Digital Gradient Sensing (DGS):
A Full-Field Optical Technique to Measure Angular Deflections of Light Rays and Its Applications to Failure Mechanics

by

Chandru Periasamy

A dissertation submitted to the Graduate Faculty of
Auburn University
in partial fulfillment of the
requirements for the Degree of
Doctor of Philosophy

Auburn, Alabama
August 4, 2012

Keywords: experimental mechanics, optical metrology, stress concentration, high strain rate characterization, failure mechanics of materials

Approved by

Hareesh V Tippur, Chair, McWane Professor of Mechanical Engineering
Jeffrey C Suhling, Quina Distinguished Professor of Mechanical Engineering
James S Davidson, Associate Professor of Civil Engineering
Barton C Prorok, Associate Professor of Materials Engineering

Abstract

Optical transparency is an essential characteristic of solids used in many engineering applications such as automotive windshields, electronic displays, aircraft windows and canopies, hurricane resistant windows, bullet resistant enclosures, personnel helmet visors, and transparent armor used by the military. In some of these applications, the ability of a structure to continue to remain transparent and bear load after impact is also critical for personnel safety.

Motivated by these, an optical, full-field measurement technique called Digital Gradient Sensing (DGS) has been introduced in this dissertation for measuring angular deflections of light rays propagating through transparent solids subjected to non-uniform quasi-static and dynamic stress fields. The technique is based on the elasto-optic effect exhibited by transparent materials due to the imposed stresses that cause light rays to deflect. The working principle of the method is explained, and the governing equations derived. DGS employs 2D Digital Image Correlation (DIC) technique to quantify the angular deflections, which can then be related to spatial gradients of stresses under plane stress conditions. The new method is first demonstrated by performing validation experiments to capture angular deflections of light rays in two orthogonal directions produced by a thin plano-convex lens.

The feasibility of this method to study material failure/damage is demonstrated on transparent planar sheets of PMMA subjected to both quasi-static and dynamic line-load acting on an edge. In the latter case, ultra high-speed digital photography is used to perform time-resolved measurements. The quasi-static measurements are successfully compared with those based on the Flamant's solution for a line-load acting on a half-space in regions where plane stress conditions prevail. The dynamic measurements, prior to material failure, are also successfully compared with finite element computations. The

measured stress gradients near the impact point after damage initiation are also presented and failure behavior is discussed.

DGS is next extended to study fracture mechanics and impact mechanics problems, where stress gradients near crack and punch tips in transparent PMMA sheets are quantified. Both quasi-static and dynamic mode-I crack problems are studied. The crack-tip stress intensity factors measured under quasi-static and dynamic loading conditions using DGS are in good agreement with the analytical and finite element results. The problem of a square-punch impacting the edge of a PMMA sheet is also studied using DGS by exploiting punch-tip – crack-tip analogy. The dynamic punch-tip stress intensity factors are extracted from the optical measurements and are again in good agreement with the ones from the finite element counterparts.

The DGS method is finally extended to study deformation of thin structures in reflection mode. After suitably modifying the governing equations, full-field surface slopes of specularly reflective thin plates (silicon wafers) subjected to out-of-plane displacements are quantified for the case of a clamped plate subjected to central deflection. The full-field plate curvatures are also evaluated from surface slope fields in view of the direct dependency of stresses on curvatures in thin structures. Both surface slope and curvature fields are successfully compared with the analytical solutions.

The dissertation also explores a few promising commercial applications of transmission mode DGS including inspection of defects and inhomogeneities in transparent media such as a glass pane. Quantification of process-induced stresses by reflection mode DGS is demonstrated by evaluating slopes and curvatures of a silicon wafer coated with a polymer film as it cures *in situ*.

Acknowledgements

I thank my advisor, Dr. Hareesh V. Tippur, for his academic guidance and financial support without which my work would not have been a success. I consider the time I spent in the "Failure characterization and optical techniques" laboratory at Auburn University, USA under Dr. Tippur's supervision to be of immense value for my personal and professional advancement. I thank my committee members Dr. Jeffrey Suhling, Dr. James Davidson and Dr. Barton Prorok for reviewing this dissertation. Partial financial support for this research through grants from ARO (W911NF-08-1-0285, W911NF-12-1-0317) and NSF (CMMI-1232821) are gratefully acknowledged.

Table of Contents

List of Tables

List of Figures

1

Introduction

1.1 Motivation

Precise measurement of physical and mechanical quantities is pivotal for performing engineering design, monitoring structural behavior or material characterization. Likewise, researchers often need to substantiate a conceived theory by measured data from real events or controlled laboratory experiments. However, accurate measurement of such data often proves to be a challenge. As a result, in several instances, experimentalists are required to rely on indirect data, because a tool capable of directly measuring the quantity of interest simply does not exist or the existing ones are inadequate. For example, in mechanics of materials and mechanical design, stress is a quantity of primary interest as it is central for implementing popular failure theories. However, there was not any method to measure stresses until the inception of photoelasticity. Even photoelasticity has restrictions such as specimen transparency and birefringence. Nevertheless, it has proved to be an extremely valuable measurement technique which has enabled engineers and researchers to approach engineering problems

with greater insight into the mechanical behavior of materials. Other methods such as Mach-Zehnder interferometry and Coherent Gradient Sensing (CGS) are also capable of measuring stresses and related quantities. Thus, every new measurement technique / tool or an improvisation of an existing tool has the potential to enhance capabilities of engineering researchers.

The existing metrology tools of engineering mechanics can be broadly classified into point-wise and full-field methods. In general, most full-field measurement techniques use light as the sensing signal and are non-contact type. They also offer the advantage of providing abundant data for analysis when compared to point-wise techniques. Full-field measurement of mechanical quantities – deformations, strains, and stresses – is necessary for understanding failure mechanisms in solids and for quantifying the associated engineering parameters. Large stress gradients in structures / components occur near stress risers such as a crack or other geometric discontinuities which are often the source of failure during service. Such situations require full-field data to compute failure parameters such as stress intensity factor to be used in the design process. The implications are even greater for characterizing materials used in transparent armor, helmet visors, aircraft canopies, etc., (Fig. 1.1) that are used to protect/shield personnel and/or critical equipment. Frequently, such transparent protective structures are expected to withstand shock and impact loads. The fact that failure of these materials could be catastrophic and involve human lives makes a strong case for having a method that is capable of directly measuring stress gradients in transparent materials.

Figure 1.1: Examples of transparent objects that are required to withstand impact loads. (Picture source: (a) www.hd-wallpapers.com, (b) www.selpro.com.hk/mainframe.htm, (c) www.conceptmobiles.com/transparent-crystal-cell-concept/ (d) www.examiner.com/article/hail-damage-and-windshields.)

This dissertation presents a new full-field optical measurement technique called Digital Gradient Sensing (DGS) capable of measuring angular deflections of light rays passing through a transparent planar object subjected to external loading. The angular deflections can be related to gradients of first invariant of stresses under plane stress conditions. The DGS technique uses the elasto-optic effect and 2D Digital Image Correlation (DIC) method in order to quantify the in-plane stress gradients. A brief

survey of the previous studies on transparent engineering materials is presented next. Following that is a review of some of the other optical full-field methods and their applications to investigate engineering mechanics problems and limitations.

1.2 Review of transparent engineering materials literature

Increased safety concerns in domestic and defense related structures have recently made failure studies on materials used in transparent armor gain importance. Patel et al. [1] presented a comprehensive discussion of transparent armor materials and thereby make a case for in-depth research on this topic. Senf et al. [2] used a Cranz-Schardin camera to record crack growth in a transparent glass-ceramic impacted by blunt steel cylinders. Strassburger [3] subjected stacked layers of transparent ceramic, soda-lime glass and polycarbonate to ballistic impact to study the projectile-target interaction. He recorded the event using flash X-ray cinematography. Wright et al. [4] performed ballistic testing of thick and thin polycarbonate plates and identified different mechanisms of dynamic failure including elastic dishing, petalling, deep penetration, cone cracking and plugging. References [5, 6] analyze the mechanisms involved in the formation of conical chips in glass produced due to spherical indenters near the specimen edge. Irrespective of the indentation distance from the edge, early material failure has been shown to be characterized by a sub-surface median crack directly under the contact point.

Over the years, there has also been a great deal of interest in developing novel transparent composites for a variety of other engineering applications which could benefit from this research. Iwamoto et al. [7] performed transparency and thermal expansion studies of an optically transparent organic nano-fiber reinforced composite that has promising characteristics such as enhanced Young's modulus and tensile strength. In 1989, Pope et al. [8] measured mechanical properties such as modulus of rupture, compression strength and Vickers hardness for a silica gel – PMMA composite for various constituent volume fractions. Ravi [9] developed a transparent photoelastic composite that could be used as a model material to study stress fields in structures made of anisotropic materials. For the first time, Yano et al. [10] developed a transparent composite reinforced with networks of bacterial nano-fibers that possess mechanical strengths five times that of engineered plastics. The increased need for transparent structural composites has prompted an increased need to develop new techniques to study stresses.

1.3 Brief review of existing full-field optical methods

Some of the widely used optical methods to study solid mechanics problems in general and stress concentration problems in particular include photoelasticity, moiré methods, laser speckle photography/interferometry, coherent gradient sensing (CGS), optical caustics and DIC. Each of these methods serves to measure different mechanical quantities such as in-plane or out-of-plane displacements and in-plane stresses or stress

gradients. This section provides a brief overview of the above methods, their capabilities, limitations, and past applications to solid mechanics problems.

1.3.1 Photoelasticity

Photoelasticity is one of the popular optical methods used to visualize and quantify mechanical stresses. It requires the specimen to be transparent (or its coating to be reflective) as well as birefringent. Birefringence involves refraction of light by an optically anisotropic material into ordinary and extraordinary rays. Certain materials such as polycarbonate, epoxy, polyurethane, etc., when subjected to mechanical load, become optically anisotropic. That is, the material displays two refractive indices at each location. When the polarized light is passed through the stressed object, it gets resolved into ordinary and extraordinary rays along the two principal stress (σ_1 and σ_2) directions. The two phase-separated rays when brought together using a plane or circular polariscope, optical fringe pattern representing contours of constant (σ_1 - σ_2) can be visualized. By analyzing the fringe pattern, the state of stress in the loaded specimen can be assessed.

Among its extensive range of applications, photoelasticity has been used to study problems involving dynamic events and stress concentrations. For example, in 1958, Wells and Post [11] used photoelasticity to obtain transient stress fields surrounding a propagating crack. de Graaf [12] used photoelasticity to witness stress waves around a dynamically growing crack in steel. Dally [13] also used photoelasticity to obtain

instantaneous stress fields around a growing crack-tip to establish a relationship between the instantaneous stress intensity factor and the crack propagation velocity. Recently, Ayatollahi and Nejati [14] used photoelasticity to study singular stress fields in V-notched Brazilian disks (see Fig. 1.2) subjected to two diametrically opposite loads. Photoelasticity also continues to be popular in the study of fast fracture/failure events [15, 16].

Figure 1.2: Isochromatic fringes in a diametrically loaded V- notched Brazilian disk (Reproduced from Ref. [14])

1.3.2 Laser speckle interferometry

When an expanded beam of coherent laser light is used to illuminate an *optically rough* surface – the mean pitch of the surface feature greater than the wave length of light – scattering occurs. The scattered wavelets from the object surface interfere among

themselves randomly produce a stochastic interference pattern called laser speckles in the space in front of the object surface. The speckle pattern that is present on a plane adjacent to the specimen surface gives it a granular appearance. The speckles adjacent to the specimen surface also follow the in-plane surface deformation. In practice, two exposures of speckles corresponding to reference and deformed states are recorded on the same film/sensor. After processing the film, the in-plane displacements can be extracted using optical spatial filtering or digital speckle correlation of reference and deformed images. This method initially found applications in areas such as vibration analysis of thin plates [17] and strain concentration measurements [18]. It continues to be popular in its modern day variation as electronic laser speckle interferometry. For example, it has recently been used for studying strain distribution in ply wood [19] and wood-fiber based composites [20].

1.3.3 Moiré methods

When a periodic geometric pattern (such as equally spaced linear gratings) is superposed on a nearly identical pattern with a small difference in its period, an optical pattern referred to as moiré fringes appear. These occur due to optical interference of the two geometric patterns. The commonly used geometric patterns are lines, cross grid, concentric circles and radial lines, and are referred to as gratings. The moiré phenomenon can be used to measure in-plane or out-of-plane displacements. The resolution of the measured quantities directly depends on the pitch of the grating. Hence, when greater

displacement resolutions are desired, high density gratings (say > 200 lines per mm) are printed on object surface using an elaborate microlithography process.

The in-plane moiré method is used to measure in-plane displacements on planar surfaces. Typically, one of the gratings is affixed to the specimen surface by either cementing or using microlithography. The reference grating is floated on the specimen surface and aligned such that a null field occurs under no-load condition. As the specimen deforms, the gratings attached to it also deforms relative to the reference grating, thereby forming moiré fringes. Alternatively, photographs of the reference grating can be superposed manually or digitally on the deformed gratings to obtain the moiré fringes. Theses fringes denote contours of constant in-plane displacements.

Another variation of the moiré method is the so-called shadow moiré technique used to measure out-of-plane displacements. In this method, the reference grating is allowed to cast its shadow on the object surface using illumination at an angle to the observation direction. The shadow grating acts as the specimen grating, as shown schematically in Fig. 1.3 (top). When the specimen deforms, the master and shadow gratings interfere, resulting in moiré fringes, representing contours of constant out-of-plane displacement, w as seen in Fig. 1.3 (bottom). These fringes can be recorded using a camera and analyzed. One significant limitation to this method is that the grating density cannot be too high (typically >200 lines per inch) as it will lead to increased diffraction effects and poor contrast between the reference and shadow grating.

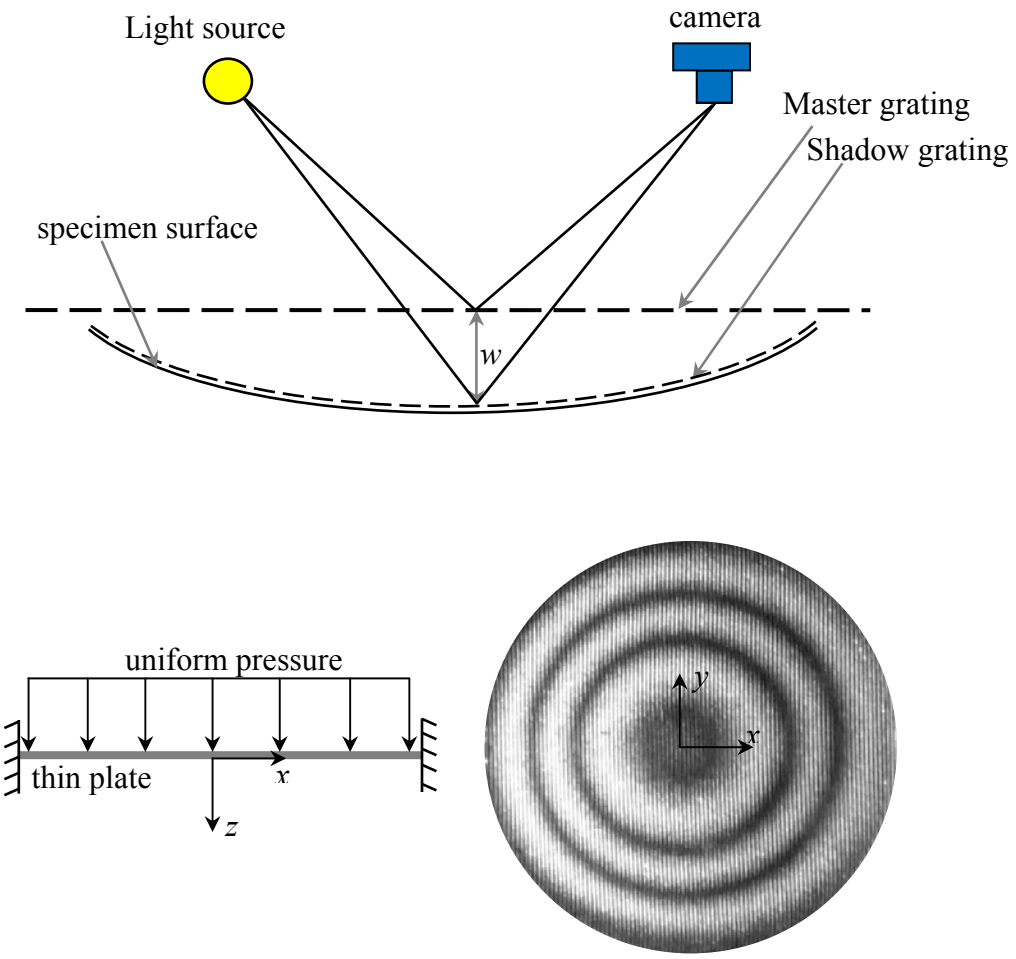

Figure 1.3: Schematic of the shadow moiré method (top) and shadow moiré fringes of out-of-plane displacements in a clamped plate subjected to uniform pressure (bottom).

When the specimen to be analyzed is large in terms of its in-plane dimensions, and a grating of the same size is not available or feasible, projection moiré method is used. It involves projecting a grating pattern onto the specimen surface at an angle while recording the specimen surface normally.

When higher resolution (sub-micron to microns) is required, moiré interferometry (or, high resolution moiré) is used. In this, the specimen is first printed with a diffraction grating that is highly reflective. Then, the specimen surface is illuminated by two coherent plane waves at two equal but opposite angles relative to observation direction such that the first order diffracted beam corresponding to the two plane waves emerge normally from the specimen surface along the observation direction. In the undeformed state, a null-field occurs in the field of view. When the specimen is deformed, the two first order diffracted rays interfere resulting in moiré fringes. These fringes represent contours of constant in-plane displacement.

Moiré methods and moiré interferometry are used to study deformation of thin films and planar structures such as electronic packages. Park et al. [21] used micro-moiré interferometry to measure thermal shear strain that causes delamination between a chip and the adhesive in anisotropic conductive film (ACF) package. Rozenburg et al. [22] used moiré method to obtain displacement fields around a bi-material interface crack and obtained mixed-mode stress intensity factors. Savalia and Tippur [23] used moiré interferometry to study the evolution of debonding of a cylindrical glass inclusion ahead of a crack-tip in an epoxy matrix.

1.3.4 Schlieren photography

August Toepler invented Schlieren photography during 1859-1864 [24] and used it to study density gradients in transparent fluids. A Schlieren system (Fig. 1.4) consists of a beam of light illuminating an object. The object waves are then collected by a lens (or, mirrors) and imaged. At the focal plane of the imaging lens (or, mirror), a knife-edge is used to block half the collected rays. When the field of observation has uniform density distribution, the image will appear as a uniform light field. In the presence of density variations, the focal plane distribution of the light field is non-uniform (will not be a well defined focal spot). Blocking off one-half of the light field will result in an image with enhanced gray scales corresponding to the density variations in that medium.

When a transparent fluid (say air) of uniform density exists in front of the object, the image recorded by the camera will be uniform. However, when the fluid density becomes non-uniform (due to temperature gradients or shock waves), light rays get refracted due to the resulting spatial variation of refractive indices. This in turn results in an enhanced contrast in the image recorded by the camera. A Schlieren image revealing the density variations surrounding an air jet (J) in a cross-flow reproduced from Ref. [25] is shown in Fig. 1.4. This method can also be used for studying structural mechanics problems that involve transparent objects. One example is the use of Schlieren optics by Forde et al. [26] to investigate shock waves near fracture fronts in impact loaded borosilicate glass.

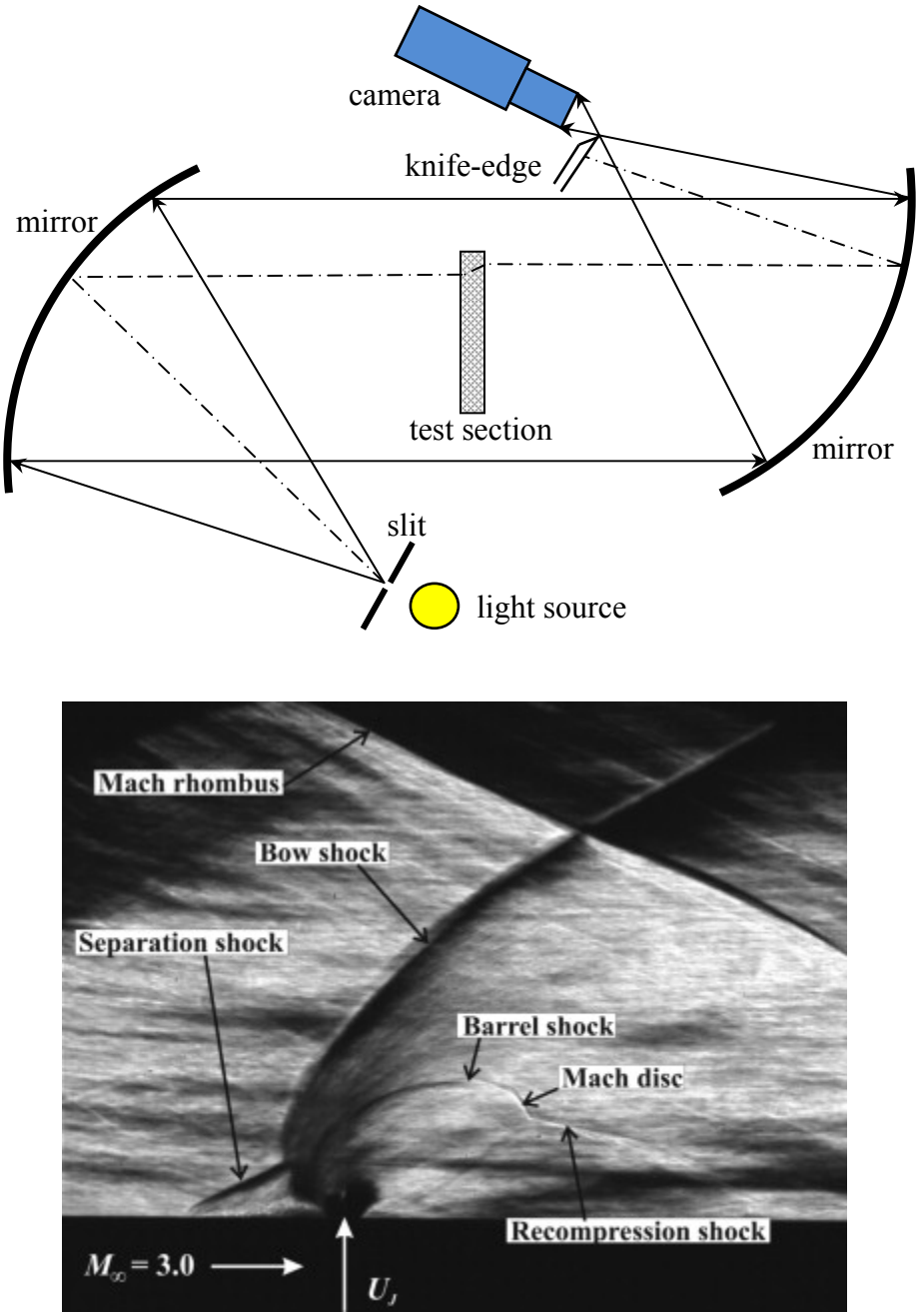

Figure 1.4: Schematic of Schlieren system (top) and Schlieren image of air jet (*J*) interacting with a supersonic cross-flow (bottom, Reproduced from Ref. [25]).

1.3.5 Coherent Gradient Sensing (CGS)

CGS is a coherent light interferometer for quantifying the refractive index and/or thickness changes in transparent planar solids to produce contours of constant angular deflections of light rays passing through the material. It can also be configured for opaque objects that are specularly reflective. Like photoelasticity and moiré methods, CGS is insensitive to rigid body motions. The experimental setup involves the specimen, two Ronchi gratings (separated by a known distance) of identical pitch with their principal directions parallel to each other, and a recording device (camera). Optical spatial filtering of the signal is also integral to the apparatus. A collimated beam of laser light is allowed to pass through the specimen (object waves) under load. The light rays emerging from the back of the specimen are diffracted into several wavelets by the first grating. All the diffracted waves undergo one more diffraction by the second grating. The interference occurring between the two adjacent parallel waves beyond the second grating is selectively acquired by filtering out all other waves using optical spatial filtering. The resulting interference fringes correspond to contours of angular deflections of light rays. The angular deflections can further be related to in-plane gradients of the first stress invariant.

The ability of CGS to measure stress gradients made it an important measurement tool particularly in the field of fracture mechanics, as stress gradients can be used to quantify stress intensity factors for a crack. Tippur and Rosakis [27] were the first to implement CGS to study crack growth problems. These authors, in subsequent years and

along with others have used CGS to study a variety of fracture problems [28-30]. Figure 1.5 shows CGS fringes of stress gradients along the crack direction in a PMMA sheet subjected to mode-I fracture experiment, as presented by Tippur et al. [28]. Very recently, Budyansky et al. [31] have employed CGS to obtain micro-scale curvatures. Dhanotia and Prakash [32] have presented an interesting work on CGS, where they have demonstrated its feasibility to test the degree of collimation of an optical beam.

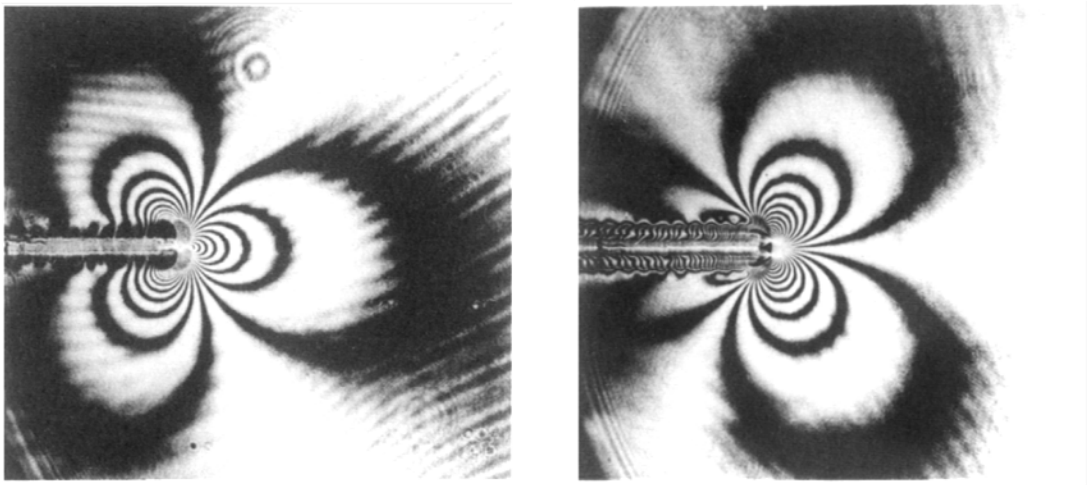

Figure 1.5: CGS fringes of stress gradients along (left) and perpendicular (right) to crack direction in a mode-I fracture specimen made of PMMA. (Reproduced from Ref. [28]).

1.3.6 Method of caustics

The method of caustics is not a full-field optical method in a conventional sense. A caustic curve is a dark/shadow region surrounded by a bright optical curve, cast behind a deformed transparent object illuminated with a collimated light beam. In Fig. 1.6, let the dashed lines represent the deformed shape of a transparent planar specimen. When a

collimated beam of light passes through this deformed region, light rays deflect away from the optical axis in this case, and intersect on a curve behind the specimen. The region inside this curve is dark as it receives no light, and is called the shadow spot. The deflection of light rays occurs due to the local refractive index change as well as the thickness change in the planar specimen. The size of this caustic curve depends on the distance between the specimen and the screen, as well as the local stress state (and hence the stress intensity factor in a fracture mechanics problem).

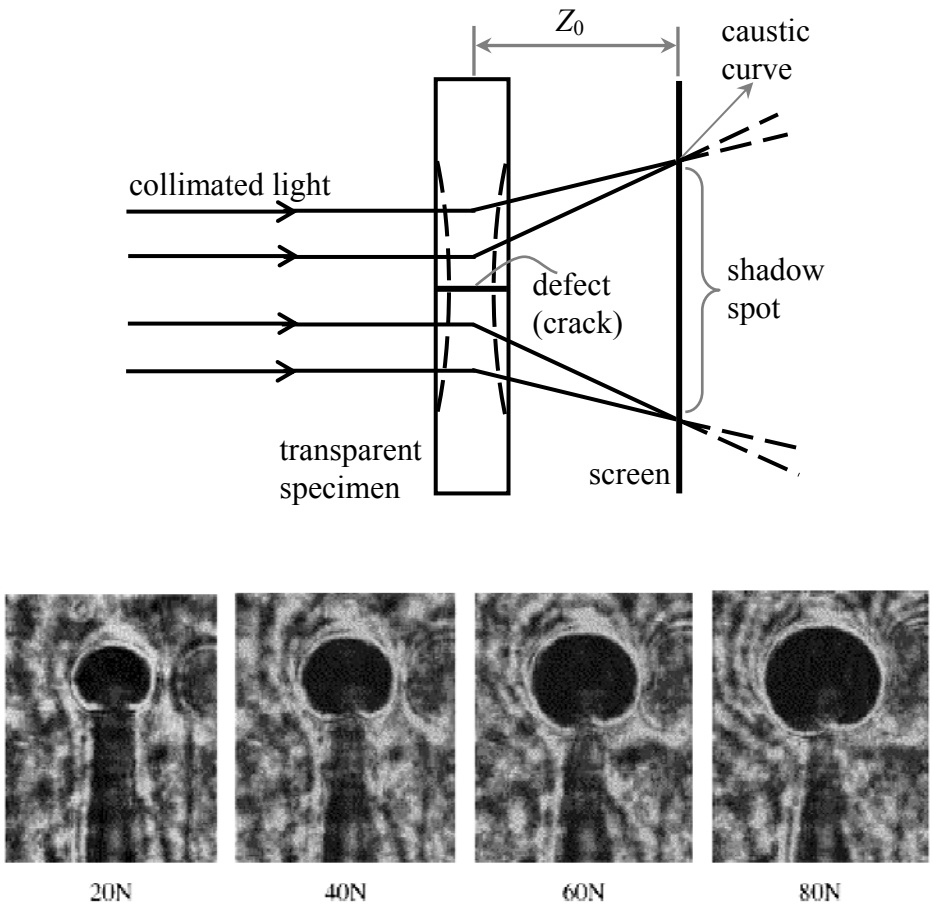

Figure 1.6: Schematic representing the phenomenon of caustics (top, dashed lines represent deformed shape of the transparent specimen) and evolution of the caustic with increased load near a crack-tip (bottom, reproduced from Ref. [33]).

A monograph edited by Sih [34] presents an elaborate description of the method and its applications to fracture mechanics problems. Zender and Rosakis [35] demonstrated the applicability of the method of caustics to obtain the *J*-integral for planar cracked bodies with elastic-plastic yielding. Yao et al. [33] used caustics measurements to obtain crack-tip stress intensity factors in functionally graded materials; representative images of caustics from their work are reproduced in Fig. 1.6. The presence of triaxial stress zone near a crack-tip and the associated difficulty to position the initial curve (that produces the optical caustic) outside the zone of triaxiality during stress-wave loading event led to a shift away from using this method [36].

1.3.7 Digital image correlation (DIC)

DIC is based on the principle of locating a point in a deformed image relative to its location in the undeformed image, and computing the relative displacement components. The method requires the object surface to be coated with a random gray-scale pattern (also called a speckle pattern) and uses ordinary white light for illumination. The speckle pattern on the specimen under no-load conditions is first photographed using a digital camera, which serves as the reference image. After the application of load, the speckle pattern distorts. This distorted pattern recorded by the camera serves as the deformed image. The two images are then segmented into an array of rectangular sub-images, each sub-image containing a rectangular array (say 20 × 20) of pixels as shown in Fig. 1.7. Each sub-image represents an intensity distribution. Now, for every sub-

image (intensity distribution) in the reference image, its location in the deformed image is searched and located. If a sub-image centered at O in the undeformed image has translated such that its new center becomes O' in the deformed image, the displacement components u and v can be obtained using affine coordinate transformations.

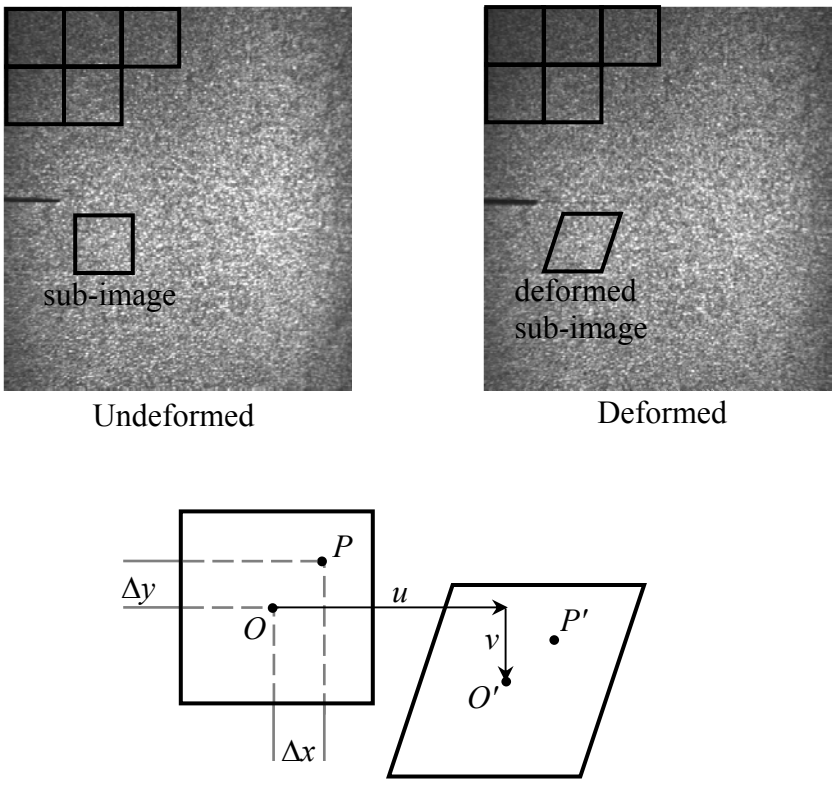

Figure 1.7: DIC principle – top: segmentation of the reference and deformed images into sub-images, bottom: displacement mapping between undeformed and deformed sub-images.

The method of DIC has gained prominence in the past decade as a metrology tool for investigating solid mechanics problems. The recent advances in digital photography, the simplicity of surface preparation and relatively low cost of implementation, combined with ubiquitous computational capabilities, are some of the major factors for its current

popularity. Further, DIC methods are capable of accurate measurement of displacements limited only by the experimental parameters such as pixel resolution of the camera, optical magnification, gray scale depth (texture, decoration) and image correlation algorithm employed. The work of Chao et al. [37] to study deformations around a dynamically propagating crack with the aid of a Cranz-Schardin film camera is an early attempt in the area of dynamic fracture mechanics. They digitized analog film recordings using a scanner to correlate successive images and estimate displacements. With the advent of modern digital high-speed cameras offering recording rates from a few thousand to a few million frames per second, there has been a significant interest in this method for studying highly transient problems [38-40].

1.4 Objectives

The primary objective of this dissertation is to establish the DGS method as a viable tool for measuring angular deflections of light rays propagating through transparent objects subjected to external loads and quantifying the local stress gradients. The following are the major items to be addressed:

- Develop the governing equations for the DGS method that relate the specimen's elasto-optic effect to the physical quantity to be measured namely, the angular deflections of light rays.

- Relate angular deflections of light rays to the mechanical fields namely, the two orthogonal in-plane stress gradients.
- Develop a viable experimental apparatus to implement DGS method on transparent polymers under static and dynamic loading conditions.
- Perform calibration experiments using well defined wave fronts to validate the working principle of DGS.
- Examine the effects of different experimental parameters such as the depth of field, sub-image size, target distance, optical uniformity of the medium, etc., on measurements.
- Conduct quasi-static experiments for the stress concentration problem of a line-load acting on the edge of a planar sheet, and measure light ray deflections near the load point. Use the angular deflection fields to determine the stress gradient fields around the stress concentration. Investigate the feasibility of estimating the stress field from the measured stress gradients.
- Develop a long-bar experimental setup capable of dynamically loading the edge of a planar object. Using the setup, conduct a dynamic line-load experiment on a transparent planar sheet, measure instantaneous angular deflection fields near the load point, and compare the results with the ones from finite element (FE) simulation of experiments.
- Demonstrate the feasibility of DGS to study deformation fields around a quasi-statically loaded crack. Using the measured fields, extract the crack-tip stress intensity factors and examine the results relative to the analytical solutions.

- Perform dynamic fracture experiments using DGS to measure deformation fields around the crack-tip, both before and after crack initiation. Use the crack-tip field equations to extract instantaneous stress intensity factors and obtain fracture parameter histories. Compare measurements with FE results until crack initiation.
- Using the long-bar setup previously developed, conduct a dynamic experiment where the edge of a planar specimen is subjected to square punch impact. Using the punch-tip – crack-tip analogy, extract instantaneous stress intensity factors at the punch corner.
- Examine the feasibility of extending DGS to reflective objects to study surface slopes and curvatures in thin structures.

1.5 Organization of the dissertation

This dissertation is organized into 10 chapters including the current one. Chapter 2 presents the experimental setup, working principle and the derivation of governing equations for the DGS method. Chapter 3 presents a calibration and benchmark experiments to validate the method. The implementation of the DGS method to a stress concentration problem, where angular deflections of light rays produced in a transparent PMMA specimen subjected to a quasi-static line-load on its edge is presented in Chapter 4. Subsequently, Chapter 5 will include the dynamic counterpart of the line-load experiment, where the development of the long-bar setup is discussed.

Chapters 6 and 7 are dedicated to quasi-static and dynamic fracture experiments, respectively, in which crack-tip stress intensity factors are obtained from the measured angular deflection fields. Chapter 8 presents the dynamic punch experiment performed using the long-bar setup. The last of the experiments correspond to the ones performed to demonstrate the feasibility of DGS to measure surface slopes of reflective surfaces, and are presented in chapter 9. Major conclusions of this work are presented in Chapter 10. A few miscellaneous topics and a few promising applications of the DGS method are presented in the Appendix.

2

The Digital Gradient Sensing (DGS) Method: Experimental Details and Working Principle

This chapter deals with the working principle and an analysis of the DGS method for experimental mechanics. First, the details of a typical experimental setup needed to implement the method are provided. A ray analysis that takes into account the elasto-optic effect exhibited by transparent objects under stress is presented. Using simplified 2D assumptions, the optical measurements are subsequently linked to the mechanical fields.

2.1 Experimental setup

The schematic of the experimental setup for DGS method is shown in Fig. 2.1. It consists of a uniformly illuminated speckle target, a planar transparent test object and a digital camera. The target is a planar surface coated with a random speckle pattern produced by spraying it with fine mists of black and white paint. The transparent specimen to be tested is placed in front of and parallel to the target plane at a known distance Δ (= distance between the mid-plane of the specimen and the target plane). A camera fitted with a relatively long focal length lens is placed behind the specimen at a

large distance L ($>>\Delta$) and focused on the target plane through the specimen in the region of interest.

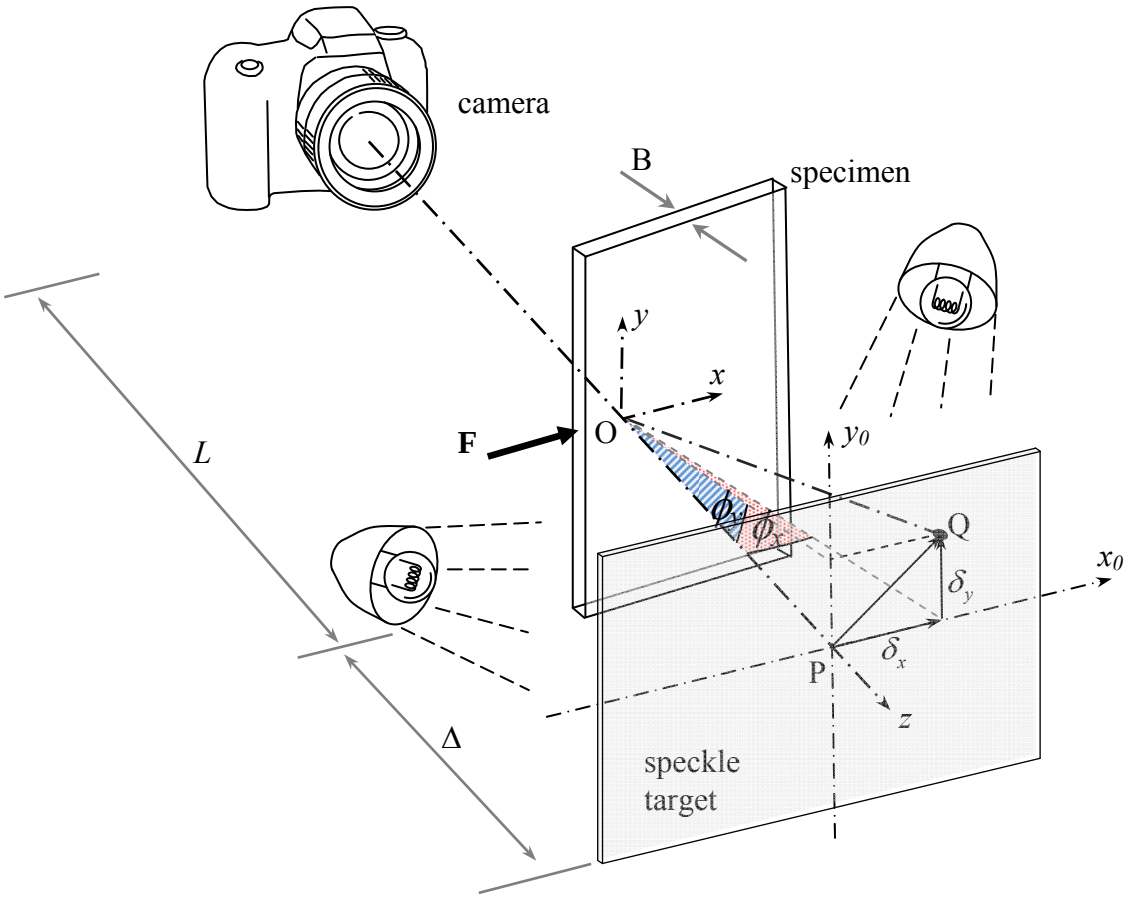

Figure 2.1: Schematic of experimental setup for Digital Gradient Sensing (DGS) method to determine planar stress gradients in phase objects.

The target is uniformly illuminated using two white light sources. The illumination sources are situated sufficiently far away from the specimen to minimize thermal currents that may distort the speckle images and/or heat the specimen during the experiment. The digital camera settings and lens parameters are selected such that the aperture is sufficiently small for achieving a good depth of field to keep speckles on the

target in focus, whilst keeping the salient features of the specimen plane (say, specimen edges, load point, etc.) discernible in the recorded image.

2.2 Working principle

In Fig. 2.1, let the in-plane coordinates of the specimen and target planes be denoted (x, y) and (x_0, y_0), respectively, and the optical axis of the setup coincide with the z-axis. Let the speckles on the target plate be photographed normally through the transparent specimen of nominal thickness B and refractive index n in its reference (or, no-load) state. That is, a generic point P on the target plane, corresponding to point O on the specimen (object) plane, is recorded by the camera in the reference state. When subjected to mechanical load (say, due to force F acting on the edge of the specimen in Fig. 2.1), both refractive index and thickness changes occur throughout the specimen depending on the local state of stress. A combination of these changes causes light rays to deflect. That is, the light ray $\overline{\mathrm{OP}}$ in the reference/undeformed state now corresponds to $\overline{\mathrm{OQ}}$ after the specimen deforms. By quantifying the spatial vector $\overline{\mathrm{PQ}}$ and knowing the separation distance Δ between the mid-plane of the specimen and the target, the angular deflection ϕ of the light ray relative to the optical axis can be determined.

Let $\hat{i}, \hat{j}$ and $\hat{k}$ denote unit vectors for the Cartesian coordinates defined with point O as the origin. When the specimen is free of any in-plane deformation, the unit vector $\hat{k}$ is collinear with $\overline{\mathrm{OP}}$ bringing point P(x_0, y_0) to focus when imaged by the camera via point O(x, y). Upon deformation, the optical path is locally perturbed, thereby

bringing a neighboring point Q($x_0+\delta_x$, $y_0+\delta_y$) to focus. Here δ_x and δ_y denote components of the vector $\overline{\mathrm{PQ}}$ in the *x*- and *y*-directions.

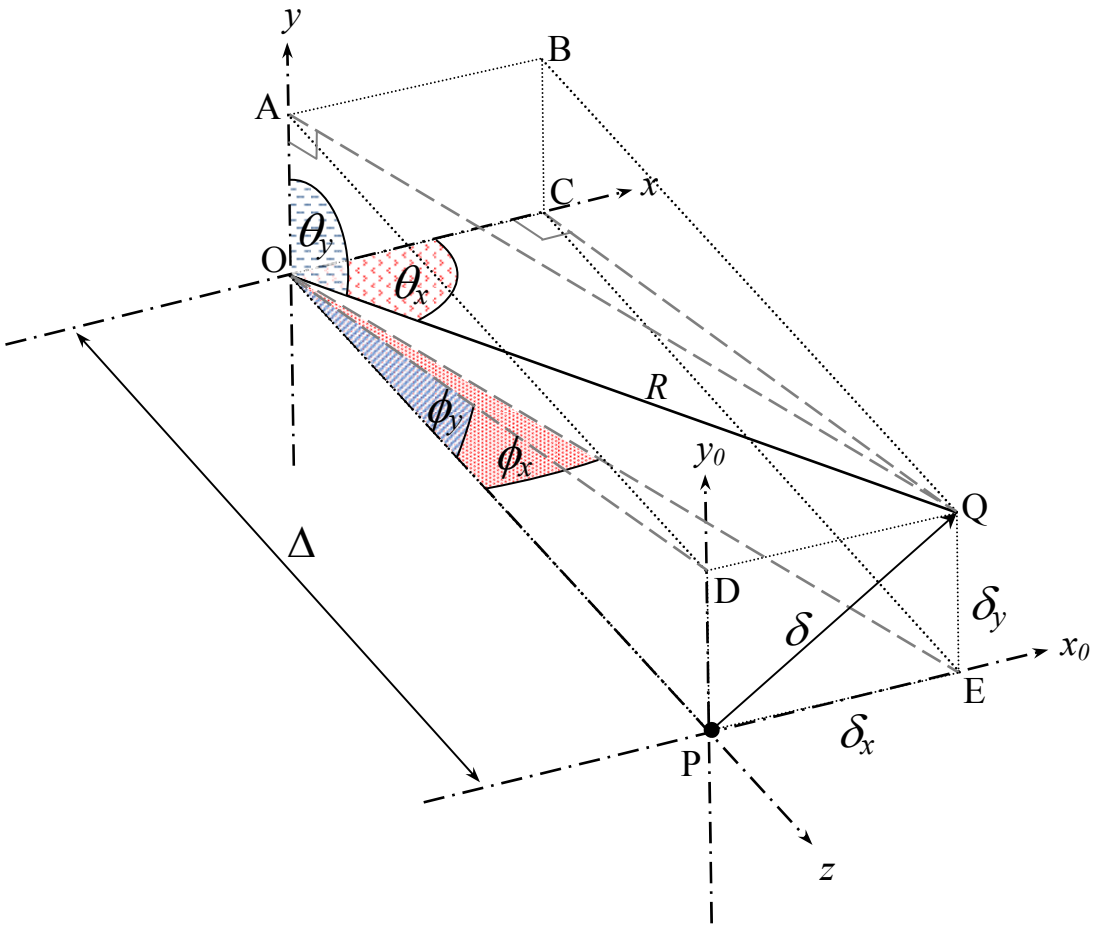

Figure 2.2: Schematic of the working principle of DGS.

Let the unit vector corresponding to the perturbed optical path $\overline{\mathrm{OQ}}$ be,

$$\hat{d} = \alpha\hat{i} + \beta\hat{j} + \gamma\hat{k}\,, \tag{2.1}$$

where α, β and γ are the direction cosines of $\hat{d}$, and, ϕ_x and ϕ_y are the components of the angular deflection ϕ in the *x*-*z* and *y*-*z* planes, respectively, as shown in Fig. 2.2.If the initial thickness and refractive index of the specimen are *B* and *n*, respectively, the optical path change, δS, for symmetric deformation of the specimen about the mid-plane in the *z*-direction, is given by the elasto-optical equation [28],

$$\delta S(x,y) = 2B(n-1)\int_0^{1/2} \varepsilon_{zz}\, d(z/B) + 2B\int_0^{1/2} \delta n\, d(z/B). \qquad (2.2)$$

The two terms in the above equation represent the contribution of normal strain in the thickness direction, ε_{zz}, and the change in the refractive index, δn, to the overall optical path change, respectively. The refractive index change caused by the local normal stress in the specimen is given by the well known Maxwell relation [41],

$$\delta n(x,y) = D_1\left(\sigma_{xx} + \sigma_{yy} + \sigma_{zz}\right), \qquad (2.3)$$

where D_1 is the stress-optic constant and σ_{xx}, σ_{yy}, and σ_{zz} are normal stresses in the *x*-, *y*- and *z*-directions, respectively Using the generalized Hooke's law for an isotropic, linear elastic solid, the normal strain component ε_{zz} can be related to normal stresses $\left(\varepsilon_{zz} = \frac{1}{E}\left[\sigma_{zz} - \upsilon(\sigma_{xx} + \sigma_{yy})\right]\right)$. That is, Eq. (2.2) can be written as,

$$\delta S = 2B\left(D_1 - \frac{\upsilon}{E}(n-1)\right)\int_0^{1/2}\left\{\left(\sigma_{xx}+\sigma_{yy}\right)\left[1 + D_2\left(\frac{\sigma_{zz}}{\upsilon\left(\sigma_{xx}+\sigma_{yy}\right)}\right)\right]\right\} d(z/B), \qquad (2.4)$$

where, $D_2 = \left[\upsilon D_1 + \upsilon(n-1)/E\right] / \left[D_1 - \upsilon(n-1)/E\right]$, E is the Young's modulus and υ is the Poisson's ratio of the transparent solid. In the above equation, the term $D_2\left(\frac{\sigma_{zz}}{\upsilon(\sigma_{xx}+\sigma_{yy})}\right)$ represents the degree of plane strain, which can be neglected for situations where plane stress assumptions (in-plane dimensions >> thickness of the specimen and $\varepsilon_{zz} \simeq 0$) are reasonable. Thus, for plane stress conditions, Eq. (2.4) reduces to,

$$\delta S(x,y) \approx C_\sigma B\left(\sigma_{xx}+\sigma_{yy}\right), \tag{2.5}$$

where, $C_\sigma = D_1 - (\upsilon/E)(n-1)$ is the elasto-optic constant of the transparent material. In Eq. (2.5), the stresses σ_{xx} and σ_{yy} denote *integrated values over the specimen thickness*. The angular deflection of a generic light ray is caused by the change in the optical path due to elasto-optic effects. Hence, the propagation vector can be related to the optical path change as [28],

$$\hat{d} \approx \frac{\partial(\delta S)}{\partial x}\hat{i} + \frac{\partial(\delta S)}{\partial y}\hat{j} + \hat{k} \tag{2.6}$$

for small spatial gradients. From Eqs. (2.1), (2.5) and (2.6), for small angular deflections, the direction cosines α and β are proportional to the in-plane stress gradients as,

$$\alpha = \frac{\partial(\delta S)}{\partial x} = C_\sigma B \frac{\partial\left(\sigma_{xx}+\sigma_{yy}\right)}{\partial x} \quad \text{and} \quad \beta = \frac{\partial(\delta S)}{\partial y} = C_\sigma B \frac{\partial\left(\sigma_{xx}+\sigma_{yy}\right)}{\partial y}. \tag{2.7}$$

A geometric analysis of the perturbed ray $\overline{\mathrm{OQ}}$ reveals the relationship between direction cosines α and β and angular deflection components ϕ_x and ϕ_y, respectively. Referring to Fig. 2.2, the perturbed ray subtends solid angles θ_x and θ_y with the *x*- and *y*-axes. The angular deflections ϕ_x and ϕ_y as defined earlier are also shown in Fig. 2.2 along with their resultant ϕ. With reference to the planes defined by OQC, OQA, OPE and OPD,

$$\cos\theta_x = \frac{\delta_x}{R}\ ,\ \cos\theta_y = \frac{\delta_y}{R}\ ,\ \tan\phi_x = \frac{\delta_x}{\Delta}\ \text{and}\ \tan\phi_y = \frac{\delta_y}{\Delta}\ , \tag{2.8}$$

where $R\ \left(=\sqrt{\Delta^2+\delta_x^2+\delta_y^2}\right)$ is the distance between O and Q. From the above, the expressions for the angular deflection components can be obtained as,

$$\begin{aligned}\tan\phi_x &= \frac{R}{\Delta}\cos\theta_x = \sqrt{1+\frac{\delta_x^2+\delta_y^2}{\Delta^2}}\cos\theta_x,\\ \tan\phi_y &= \frac{R}{\Delta}\cos\theta_y = \sqrt{1+\frac{\delta_x^2+\delta_y^2}{\Delta^2}}\cos\theta_y.\end{aligned} \tag{2.9}$$

It can be noted from Eqs. (2.9), that for small angular deflections (or, $\delta_x, \delta_y << \Delta$), the expressions reduce to $\phi_x \approx \cos\theta_x = \alpha$ and $\phi_y \approx \cos\theta_y = \beta$. Thus, for the case of small angular deflections of light rays, Eqs. (2.7) reduce to

$$\begin{aligned}\phi_x &\approx \frac{\delta_x}{\Delta} \approx \alpha = C_\sigma B \frac{\partial\left(\sigma_{xx}+\sigma_{yy}\right)}{\partial x},\\ \phi_y &\approx \frac{\delta_y}{\Delta} \approx \beta = C_\sigma B \frac{\partial\left(\sigma_{xx}+\sigma_{yy}\right)}{\partial y},\end{aligned} \tag{2.10}$$

which serve as the governing equations for the method and can be used to obtain stress gradients when specimen parameters C_σ and B are known.

The above governing equations reveal that the angular deflections ϕ_x and ϕ_y, and hence stress gradients in the x- and y-directions can be obtained by quantifying local displacements δ_x, δ_y values first and then dividing them by the separation distance Δ. The displacements δ_x, δ_y can be evaluated by carrying out a conventional 2D digital image correlation (DIC) between speckle images recorded in the reference and deformed states of the specimen. Hence the new method is aptly named Digital Gradient Sensing (DGS). A subtle but important point to note here is that displacements δ_x, δ_y are evaluated on the target plane whose coordinates are (x_0, y_0), but can be replaced with the specimen plane coordinates (x, y) for $\Delta << L$ (see, Fig. 2.1). Further justification of this assumption is provided in the next chapter.

From Eq. (2.10) it can be noted that the sensitivity of measurement of angular deflections ϕ_x and ϕ_y is dependent on two parameters δ_x (or δ_y) and Δ which provides added flexibility. The sensitivity of in-plane displacement measurement (of δ_x or δ_y) is typically dictated by a number of parameters that affect 2D digital image correlation methods including speckle characteristics/size, pixel size, sensor resolution, image processing algorithm employed, etc. The discussion of those issues is avoided here and can be found elsewhere [42]. For the speckle parameters used in this study, in plane

displacement resolution is ~3 μm as demonstrated in a few earlier works of Tippur and his co-workers [38].

It is also interesting to note that Eq. (2.10) shows that DGS method measures quantities identical to the ones measured by the Coherent Gradient Sensing (CGS) method [29, 38, and 39]. However, *unlike* CGS, DGS can be used to measure two orthogonal stress gradients in transparent solids *simultaneously* and does not use any coherent optics. This capability can be exploited for determining stresses ($\sigma_{xx} + \sigma_{yy}$) from measured stress gradients, as will be shown later in Chapter 4.

3

Calibration and Benchmark Experiments

This chapter presents a series of experiments conducted to validate the principle behind DGS, and to assess the influence of various experimental parameters on optical measurements. The DGS method is first verified by measuring a well characterized angular deflection field produced by a thin plano-convex lens. Following that is a discussion of the influence of the perspective effects. Later, the effects of depth of field, target distance and sub-image size used on measurements are presented. The chapter concludes with a discussion on the role of optical homogeneity of a planar specimen on measurement accuracy using DGS.

3.1 Angular deflection fields due to a thin plano-convex lens

To verify the DGS method, first a well-defined angular deflection field of light rays produced by a plano-convex lens was studied using the setup shown in Fig. 3.1. A target plane with the speckle pattern was placed at a relatively large distance ($L \sim 1000$ mm) from a recording camera (Nikon D100 digital camera fitted with a 28-300 mm lens

using an extension tube and aperture setting #11). A reference (undeformed) image of the speckle pattern was recorded first. Then, a *thin* plano-convex lens of a relatively long effective focal length, $f_l = 1000$ mm and clear aperture of 80 mm diameter was introduced between the camera and the speckle plane. The choice of a long focal length lens produced relatively small angular deflections of light rays similar to the ones expected in the mechanical tests to be performed on transparent polymer sheets.

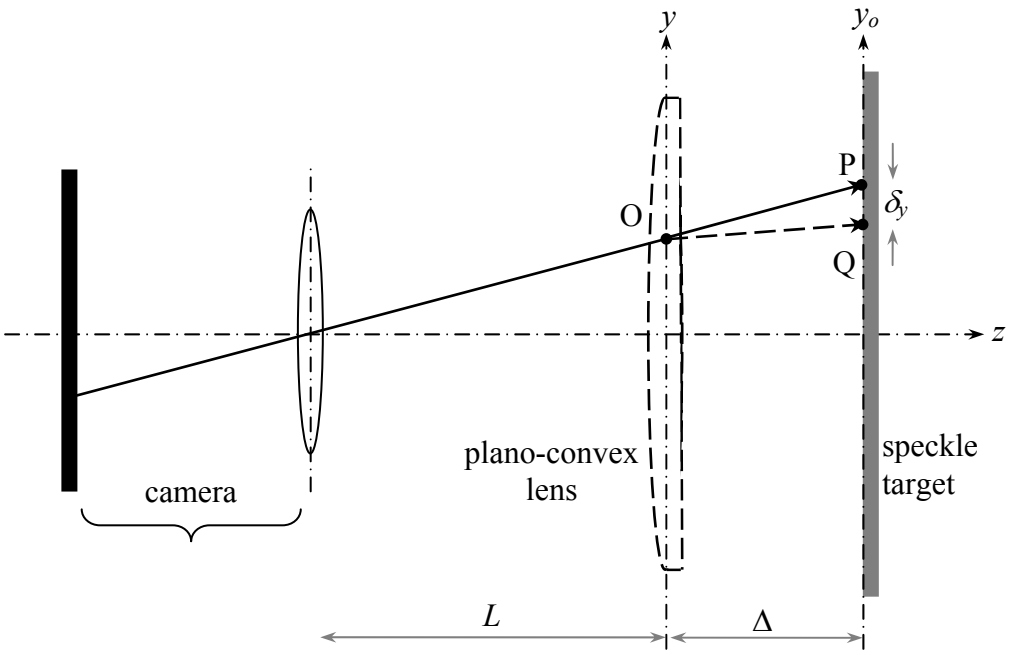

Figure 3.1: Schematic of the setup used to measure angular deflections of light rays caused by a spherical lens.

The distance from the effective center of the lens to the speckle plane was $\Delta = 19.4$ mm. Care was exercised to align the center of the plano-convex lens close to the optical axis of the camera. A second image of the speckle pattern, this time through the plano-convex lens, was recorded. The size of the image recorded by the camera was approximately $60 \times 40\,\text{mm}^2$ rectangle in the central region of the plano-convex lens. The

recording of the reference and perturbed speckle fields used a pixel resolution of 1504 x 1000 pixels (1 pixel = 39.5 μm on the target plane). The second speckle image can be considered to be the "deformed" or "perturbed" image whose angular deflection fields are given by,

$$\phi_x = \frac{\partial}{\partial x}\left(\frac{x^2+y^2}{2f_l}\right) = \frac{x}{f_l} \quad \text{and} \quad \phi_y = \frac{\partial}{\partial y}\left(\frac{x^2+y^2}{2f_l}\right) = \frac{y}{f_l}, \tag{3.1}$$

where $\left(\frac{x^2+y^2}{2f_l}\right)$ describes the spherical wave-front due to the plano-convex lens, and ϕ_x and ϕ_y are the angular deflection fields with respect to the unperturbed speckle image. As evident from Eqs. (3.1), the two orthogonal angular deflection fields are linear functions of the lens plane coordinates, *x* and *y*. Hence, the contours of constant ϕ_x and ϕ_y should be equally spaced with their principal directions in the *x*- and *y*-directions, respectively. To obtain the ϕ_x and ϕ_y fields, the in-plane displacement fields (δ_x and δ_y) were first extracted from images by performing 2D digital image correlation between the reference and perturbed speckle recordings using a commercial DIC software, ARAMIS. During the analysis, the images were segmented into 64 x 91 non-overlapping facets or sub-images resulting in an array of 64 x 91 data points. For small in-plane displacements (δ_x and $\delta_y << \Delta$) angular deflection fields were obtained as, $\phi_x \approx \frac{\delta_x}{\Delta}$ and $\phi_y \approx \frac{\delta_y}{\Delta}$. (The maximum values of δ_x and δ_y were less than 300 μm.)

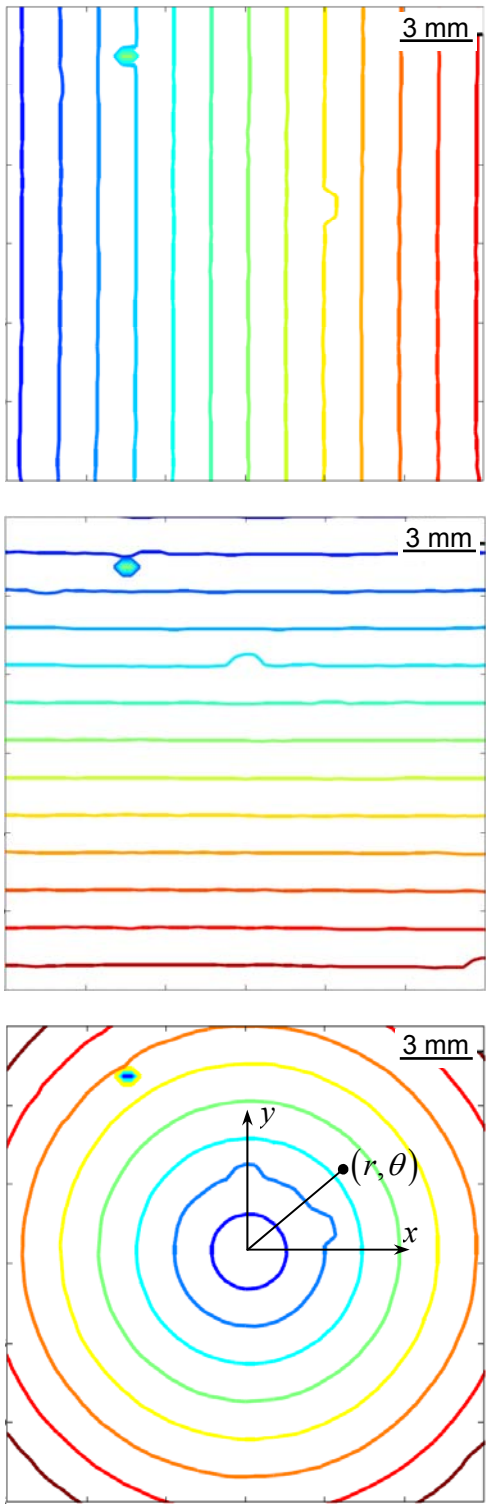

Figure 3.2: Contour plots of angular deflections (top to bottom) ϕ_x, ϕ_y and ϕ fields caused by a plano-convex spherical lens. Contour interval = 2.5 x 10^{-3} radians. (The heavy dot in the angular deflection field is due to a reference mark on the speckle plate.)

The contour plots of the experimentally obtained ϕ_x , ϕ_y and the resultant angle ϕ $\left(=\sqrt{\phi_x^2+\phi_y^2}\right)$ fields are shown in Fig. 3.2. As predicted, the contours of ϕ_x and ϕ_y are equidistant parallel lines along the *x*- and *y*-directions, respectively, and that of ϕ are equally spaced concentric circles centered on the optical axis of the lens. If the angular deflection fields are known, it is also possible to quantify the focal length of the plano-convex lens using Eq. (3.1) as, $f_l = \frac{x}{\phi_x} = \frac{y}{\phi_y}$. For this experiment, the measured focal lengths were 973 ± 32 mm from the ϕ_x field and 988 ± 42 mm from the ϕ_y field. These are within 3% of the manufacturer specified focal length of 1000 mm for the lens.

3.2 Perspective effect

As noted in the last section, the camera is focused on the target plane through the transparent object. Yet, the analysis uses the coordinates of the specimen's (phase object) mid-plane, situated at a distance Δ from the target, interchangeably. This introduces a perspective effect. That is, a point O(x, y) on the specimen corresponds to a point P(x_0, y_0) on the target plane as shown in the 2D schematic (see, Fig. 3.3). This can be taken into account by a mapping function between the specimen and the target planes. With reference to Fig. 3.3, $\tan\theta = \frac{y_s}{L} = \frac{y_t}{L+\Delta}$, where y_s and y_t are coordinates of the specimen and target planes. This can be used to account for the coordinates of the

specimen plane as $y_s = \left(\frac{L}{L+\Delta} \right) y_t$. A similar mapping function for the horizontal coordinate is obvious and implied.

Using these relations, the contours of ϕ_x and ϕ_y for the plano-convex lens were obtained and are shown (broken lines) in Fig. 3.4 along with the contours without any correction (solid lines). Evidently, for the chosen experimental parameters, the differences are rather negligible in the entire field. The errors close to the optical axis are minimum whereas they increase as one moves away from the optical axis.

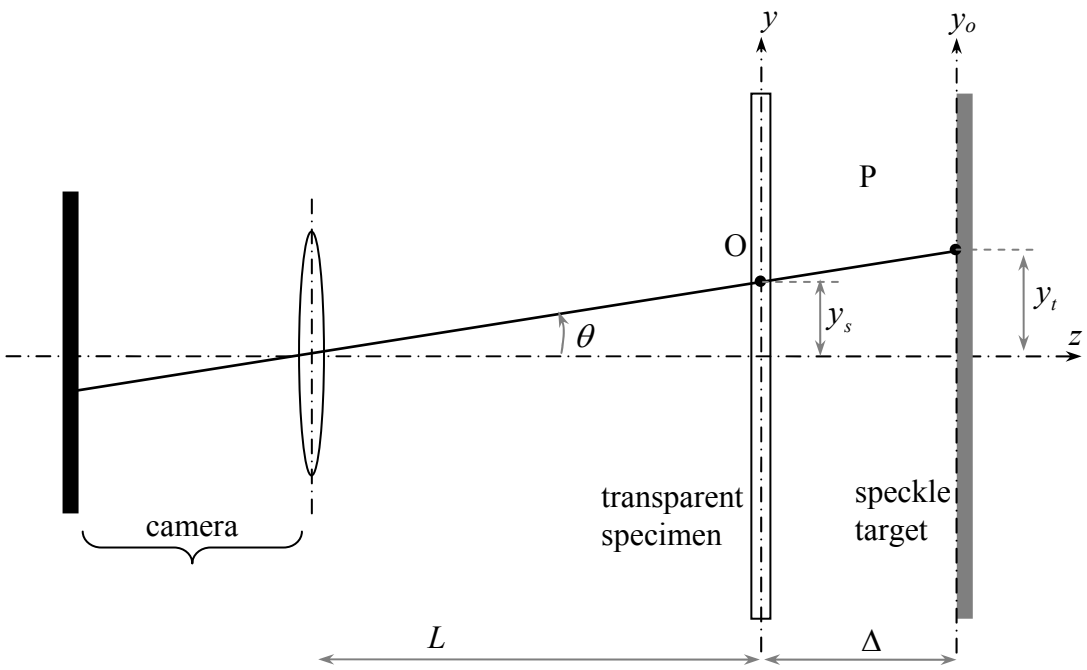

Figure 3.3: Schematic for mapping the coordinates of specimen and target planes.

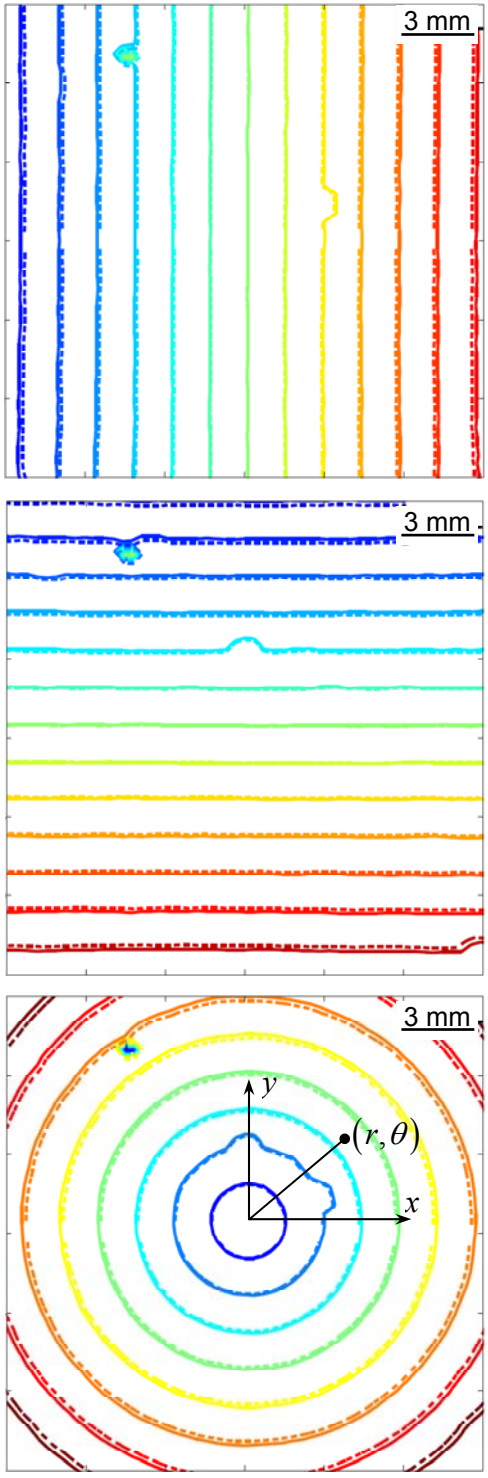

Figure 3.4: Contour plots of angular deflections of corrected (broken lines) and uncorrected (solid lines) ϕ_x (top) ϕ_y (middle) and ϕ (bottom) fields caused by a long focal length plano-convex lens. Contour interval = 2.5 x 10^{-3} radians.

3.3 Optical homogeneity and measurement accuracy

The DGS method assumes optical homogeneity of refractive index and specimen thickness in the unloaded/reference state. Mass produced materials (such as PMMA sheets used in this work) could have spatial variations of these parameters or an initial residual stress state when machined from a large sheet stock. To examine the role of such variations on measurement errors, an experiment was carried out on a PMMA specimen using a setup shown schematically in Fig. 3.5 but without applying any mechanical load.

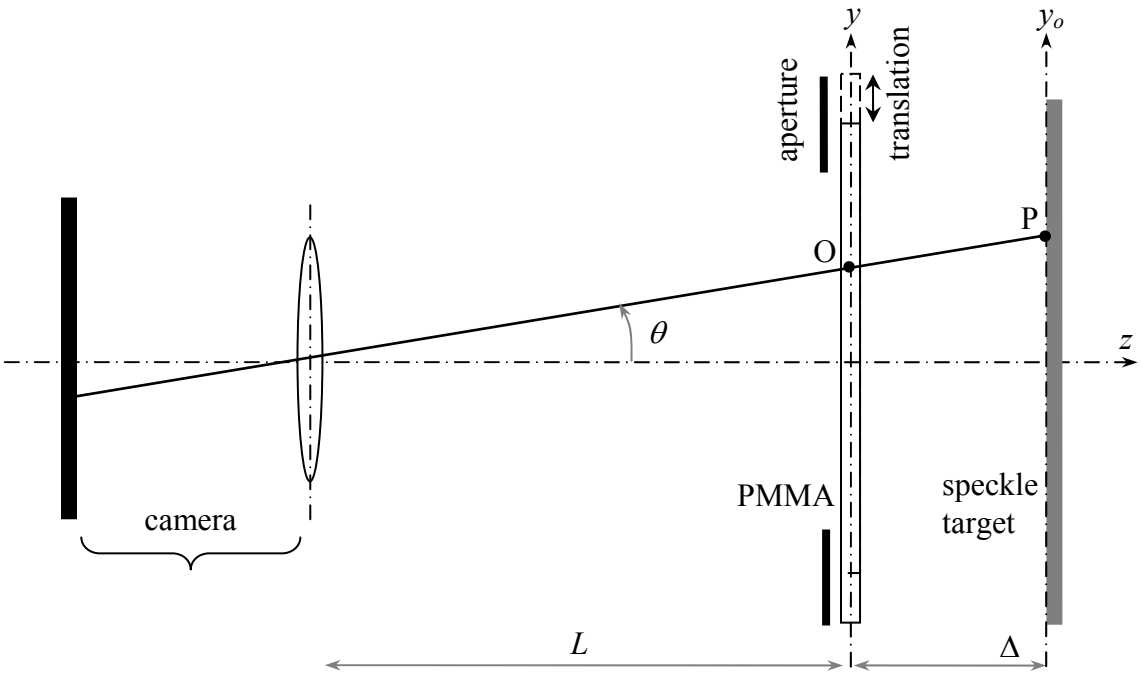

Figure 3.5: Schematic of the experimental setup used to check for residual stresses in transparent planar specimens.

A target plane decorated with a speckle pattern was placed at a relatively large distance of ~1575 mm from a recording camera (Nikon D3000 digital camera fitted with

a 70-300 mm lens (aperture setting #11) and an extension tube. Then, the specimen, a clear, 9.3 mm thick PMMA plate, was mounted on a multi-axis translation stage with micrometer adjustments and introduced between the camera and the speckle plane. A 40 mm square window/aperture, placed in front of the specimen, was used to fix the region of observation during the test.

The distance from the mid-plane of the specimen to the speckle plane, Δ, was 30 mm. The camera was focused on the speckle plane through the specimen and a reference image of the speckle pattern was recorded. Then, while the target plate held stationary, the specimen alone was translated horizontally in steps of 1 mm and speckles were recorded at each step. (The choice of these translational steps was based on the maximum anticipated displacement due to mechanically imposed loads, expected not to exceed a couple of mm.) The same was repeated in the vertical direction as well. A pixel resolution of 1936 x 1296 pixels (1 pixel = 38 μm on the target plane) was used for recording the speckles. In these translated positions, the speckles were recorded through points of the specimen different (shifted) from the corresponding points in the reference position. The presence of any non-homogeneity in the specimen between these shifted positions would cause the light rays to deflect. Hence, the images recorded at each translational step were considered ‘perturbed’ or ‘deformed’ images relative to the initial recording. By correlating the speckle images from the reference and perturbed states, the optical uniformity of the specimen was assessed.

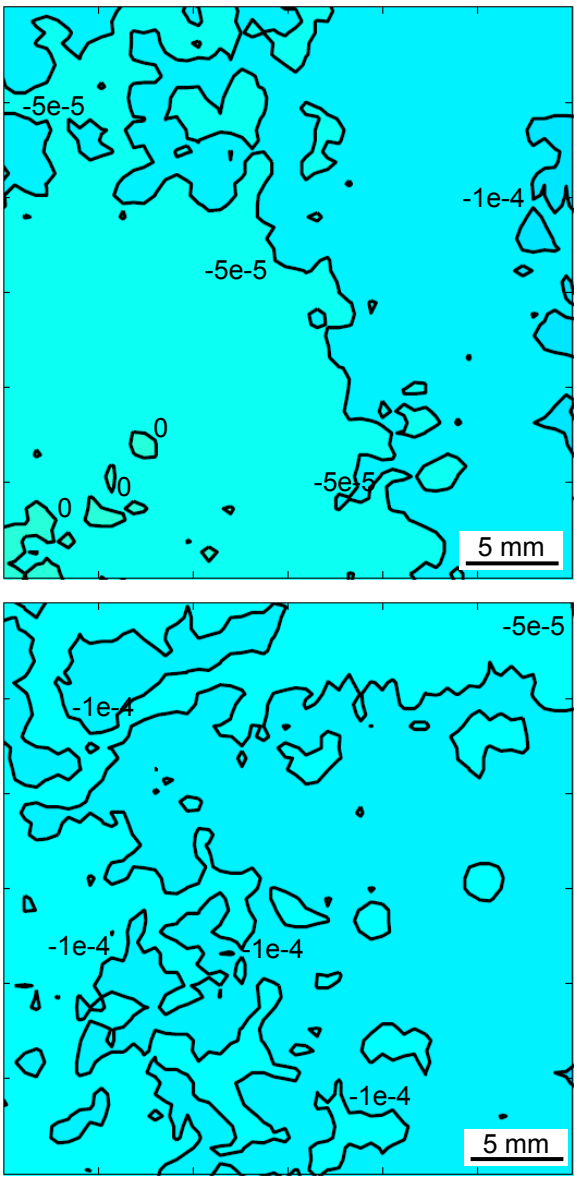

Figure 3.6: Contour plots of ϕ_x (top) and ϕ_y (bottom) fields corresponding to a horizontal specimen translation of 2 mm of the PMMA specimen. Contour labels are in radians.

The horizontal and vertical angular deflection fields (ϕ_x and ϕ_y) for one case corresponding to a horizontal translation of 2 mm is shown in Fig. 3.6. Clearly, the resulting field shows random angular deflections variation with the largest angular deflection magnitude of less than 1×10^{-4} radians. Thus, the accuracy of angular deflection measurements based on optical homogeneity is limited to values above this threshold.

Further, the displacement measurement accuracy based on the type of speckles, the recording parameters, and the correlation algorithm used in this study is 2-3 μm [38, 39]. This also translates into an angular deflection measurement accuracy of 0.5×10^{-4} - 1×10^{-4} radians when the separation distance (Δ) between the target and the specimen is in the 20-30 mm range. Thus, for the measurements to be credible, the load induced angular deflections during experiments should exceed this value.

3.4 Effect of depth of field

Being a method that uses digital image processing, the accuracy of measurements using DGS depends on the camera parameters used. One significant parameter that potentially affects the images captured is the lens aperture used during recording of the speckle field. It is common knowledge that to obtain a good depth of field a narrow aperture is required. This would diminish the light intensity recorded over the exposure time. Also, narrow apertures could limit / block light rays traveling at larger angles relative to the optical axis from reaching the image or sensor plane. This produces a shadow spot in regions of severe stress concentration. Accordingly, to study the effect of aperture size on angular deflection measurements, a stress concentration experiment on a PMMA sheet of 9.2 mm thickness was performed using different lens aperture settings. The stress concentration is produced by applying a line-load of 1000 N on an edge of the specimen resting on a rigid platform along the other edge, resulting in steep stress gradients near the loading point.

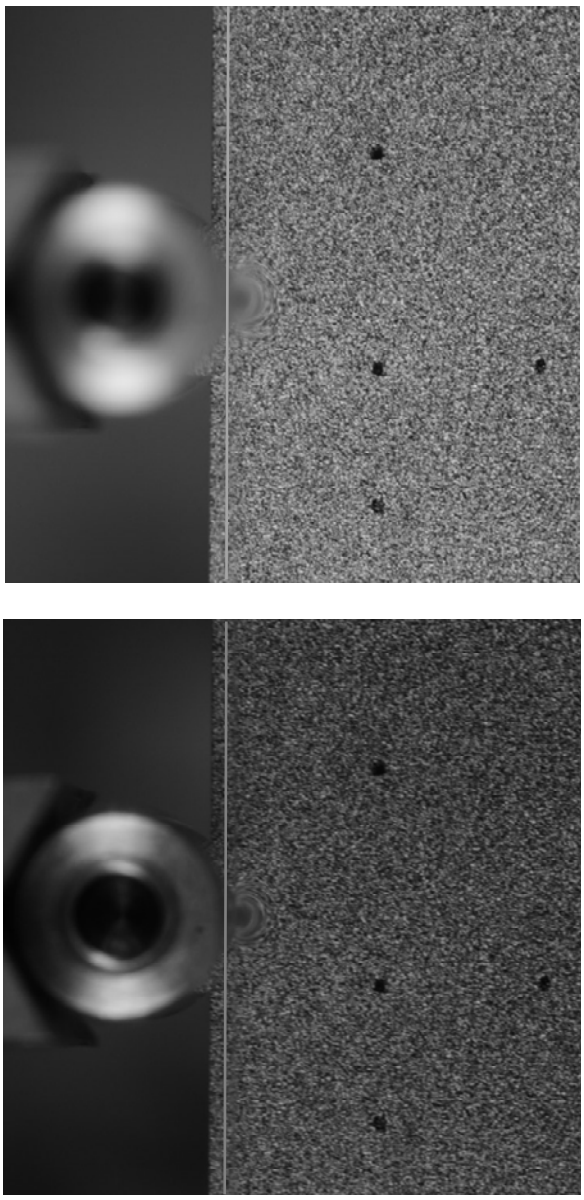

Figure 3.7: Deformed images of a PMMA sheet subjected to line-load captured using apertures 9 (top) and 16 (bottom).

The speckle patterns were recorded before and after the application of load. Two images of the speckle pattern corresponding to the deformed state are shown in Fig. 3.7. The influence of the aperture size on light intensity and depth of field are self evident (note the sharpness of the speckles as well as the focus of the loading pin between the

two images). Also evident is a small change in the size of a semi-circular region of severe angular deflections directly under the loading point / pin. The corresponding undeformed and deformed images were correlated using DIC to obtain δ_x and δ_y throughout the field. The process was repeated for three different aperture stops ($F^{\#}$ = focal length/aperture diameter) 9, 11 and 16. For each case, the angular deflection contours (ϕ_x and ϕ_y) were obtained from the measured δ_x and δ_y values. Figure 3.8 shows the contours corresponding to $F^{\#}$'s 9 and 16 overlaid on top of each other. Evidently, the contours corresponding to the different lens apertures are in good agreement with each other. The differences in the contours are attributed to the practical issue of being able to position the specimen exactly the same way for every repetition.

For a closer analysis, the radial variation of ϕ_x along 0˚ and ϕ_y along 45˚ with respect to the *x*-axis, are plotted for all three aperture cases in Fig. 3.9. Evidently, the agreement among the curves is rather good even near the load point which is closer to the optical axis of the camera, whereas, the differences among the curves are relatively more farther away from the optical axis. This may be attributed to the quality of focus achieved using different apertures. In addition, it could also be because of the lower magnitudes of angular deflections in the far field that are prone to larger errors.

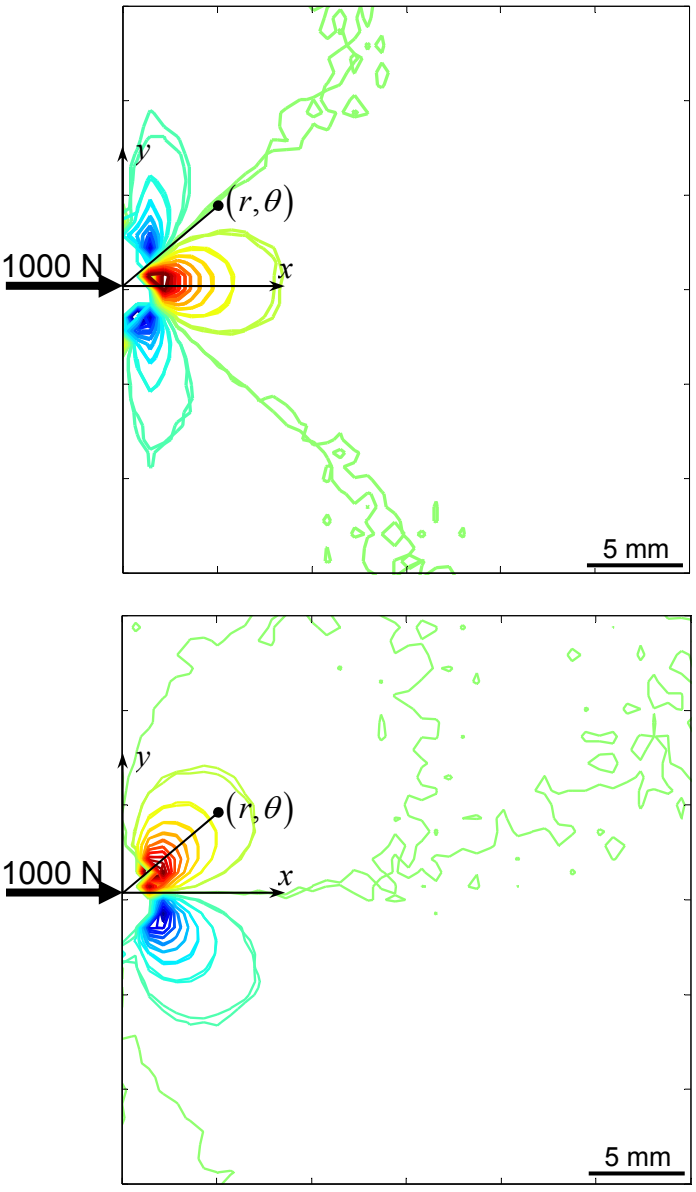

Figure 3.8: Contours of ϕ_x (top) and ϕ_y (bottom) obtained using different $F^{\#}$'s (9 and 16) corresponding to a PMMA sheet subjected to line-load on one of its edges.

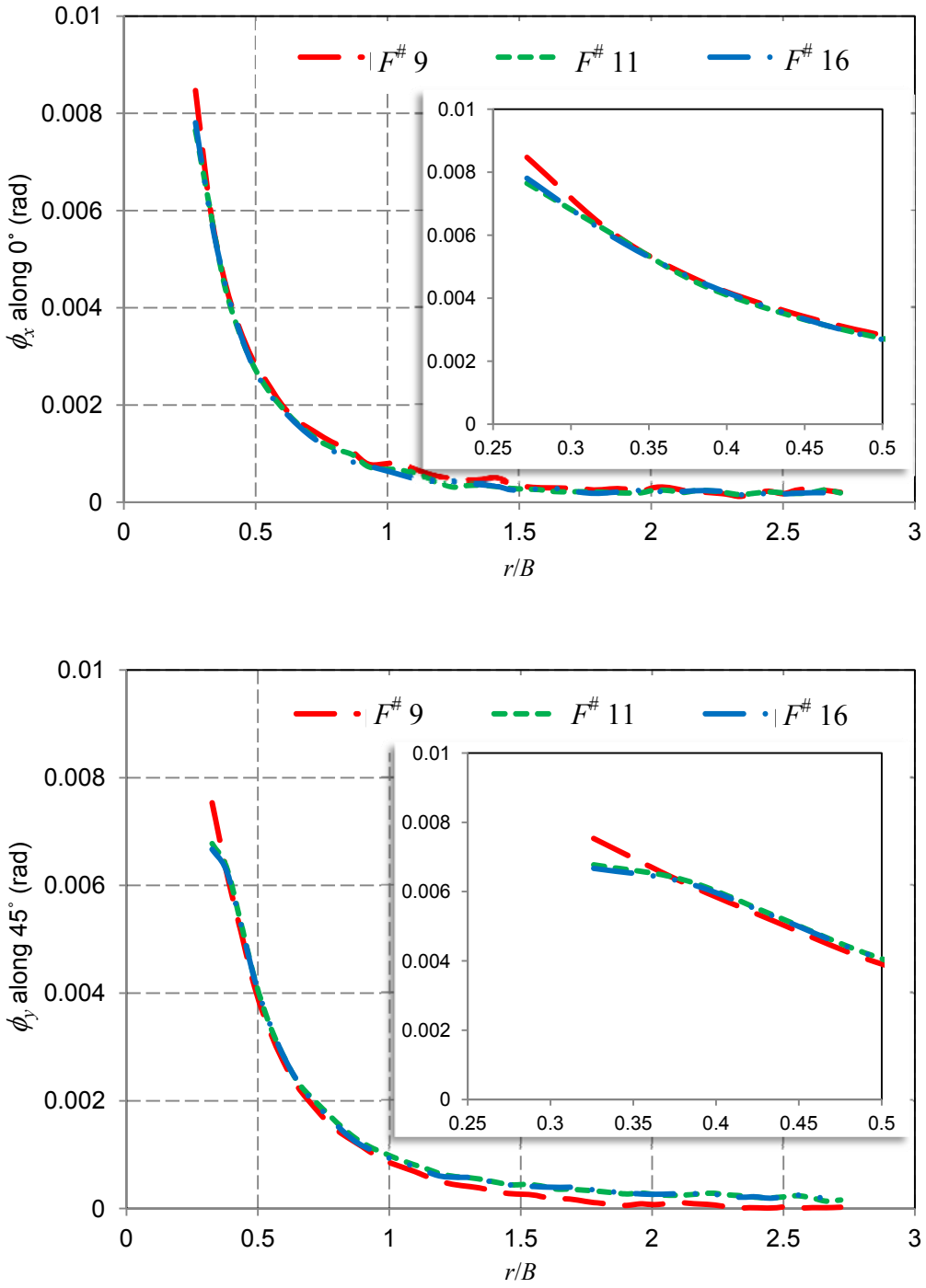

Figure 3.9: Radial variation of ϕ_x along 0° (top) and ϕ_y along 45° (bottom) obtained using different $F^{\#}$'s (9, 11 and 16) from a PMMA sheet subjected to line-load on one of its edges.

3.5 Effect of sub-image size

DGS relies on 2D DIC for evaluating displacement components δ_x and δ_y. Therefore, the accuracy of the measured angular deflections and hence stress gradients depends on the parameters used for performing image correlation. The size of the sub-image (Section 1.3.7) used during image correlation, therefore needs to be examined as well. The image processing software, ARAMIS used for all the image processing done in this work recommends a sub-image size of 15 × 15 pixels. However, in order to verify this default choice, it was necessary to correlate a single undeformed / deformed image pair using different sub-image sizes and compare the results. This was accomplished by subjecting a PMMA sheet (thickness B = 9.4 mm) to a line-load of 1077 N on one of its edges causing a severe stress gradient field, and comparing the angular deflections obtained using four different sub-image sizes. The sub-image sizes used were 10 × 10, 15 × 15, 20 × 20 and 25 × 25 pixels without any overlap. Representative ϕ_x and ϕ_y contours corresponding to the 10 × 10 and 25 × 25 sub-image sizes are shown in Fig. 3.10 overlaid on each other. Aside from the obvious difference in greater computational effort when more subsets are present for an image, the overall agreement between the two sub-image sizes is good. The smaller sub-image size results in greater noise in the measurement when compared to the larger sub-image size that produces smoother contours due to higher certainty in relative speckle location caused by deformation. The larger sub-image also produces a higher degree of averaging while generating contours due to a smaller data array as opposed to the one with smaller sub-image size.

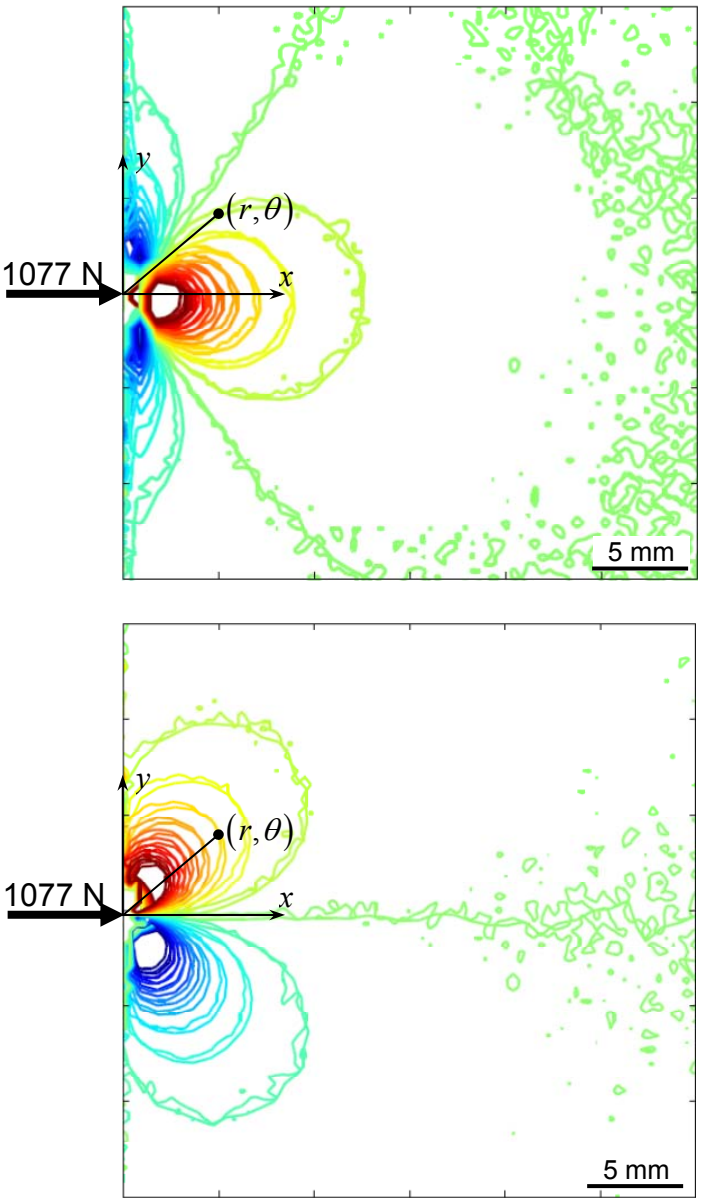

Figure 3.10: Contour plots of ϕ_x (top) and ϕ_y (bottom) obtained using different sub-image sizes (10 × 10 and 25 × 25 pixels) corresponding to a PMMA sheet subjected to line-load on one of its edges.

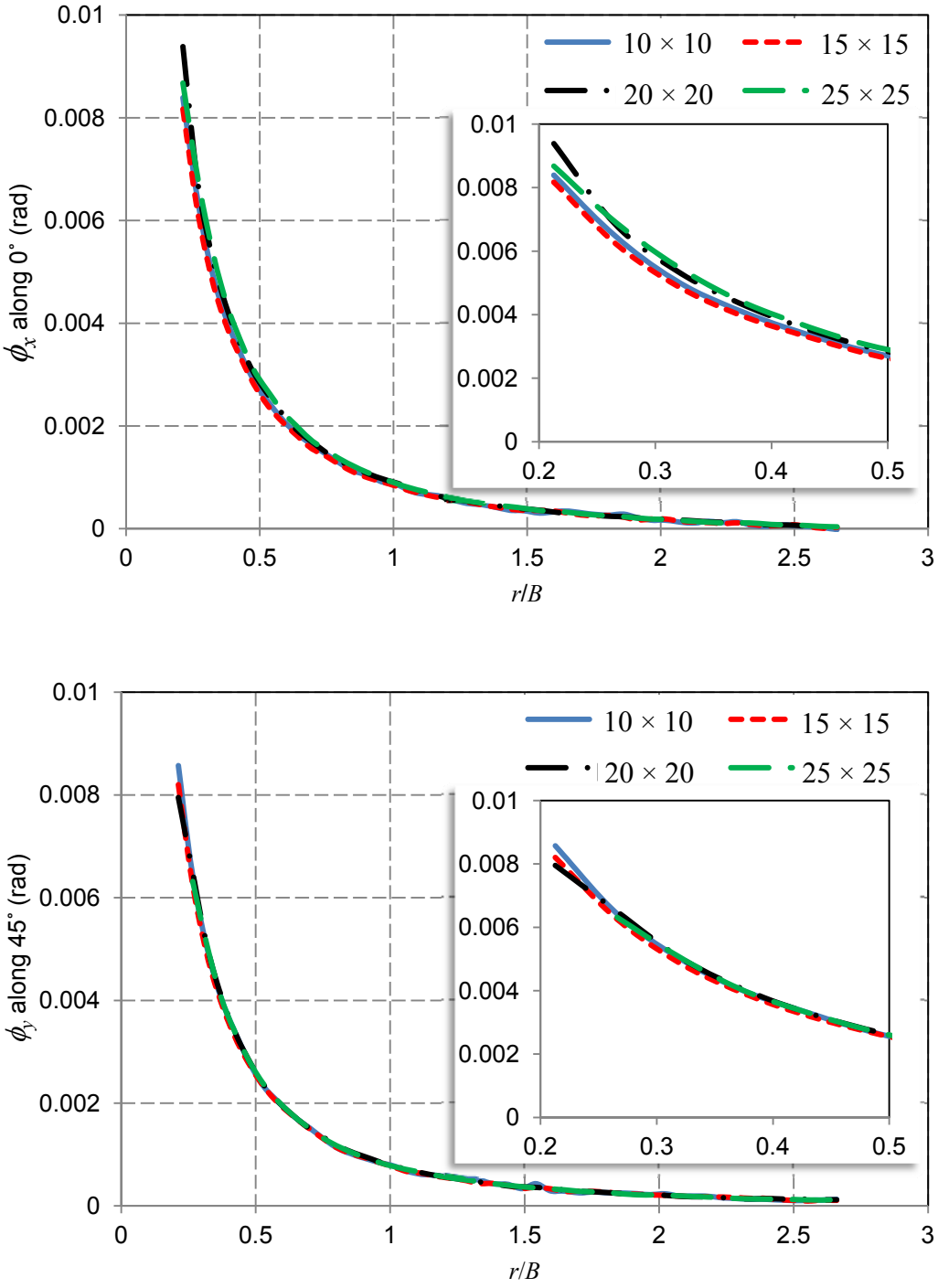

Figure 3.11: Radial variation of ϕ_x along 0˚ and ϕ_y along 45˚ obtained using different sub-image sizes (10 × 10, 15 × 15, 20 × 20 and 25 × 25 pixels) corresponding to a PMMA sheet subjected to line-load on one of its edges.

Furthermore, there is a small offset in the two sets of contours in Fig. 3.10. Prior to discussing the reason for this apparent offset, it is to be understood that a data point in the contour plot corresponds to a sub-image, and not a pixel. Therefore, the spatial resolution or the accuracy of manually selecting a point in the image is influenced by the sub-image size. In other words, smaller the sub-image size, greater is the ability to accurately represent a point in the specimen. In the current scenario of the line-load problem, the origin (loading point) needs to be selected to plot the contours in the specimen coordinates. It is this difference in the spatial accuracy of selecting the origin that caused the apparent offset. The radial variation of ϕ_x along 0˚ and ϕ_y along 45˚ with respect to the *x*-axis are plotted in Fig. 3.11. Clearly, the agreement among the curves is very good. After careful consideration, it was determined that a sub-image size of 15 × 15 pixels offered reasonable spatial accuracy without introducing noise, and became the choice for all experiments.

3.6 Effect of target distance

Another important parameter used in DGS experiments is the separation distance, Δ between the specimen's mid-plane and the speckle target. It is understood from Fig. 2.2 that smaller the Δ, smaller will be δ_x and δ_y, the basic quantities measured during the 2D DIC process. This in turn results in diminished measurement accuracy for smaller values of δ_x and δ_y, which carries over to the angular deflections.

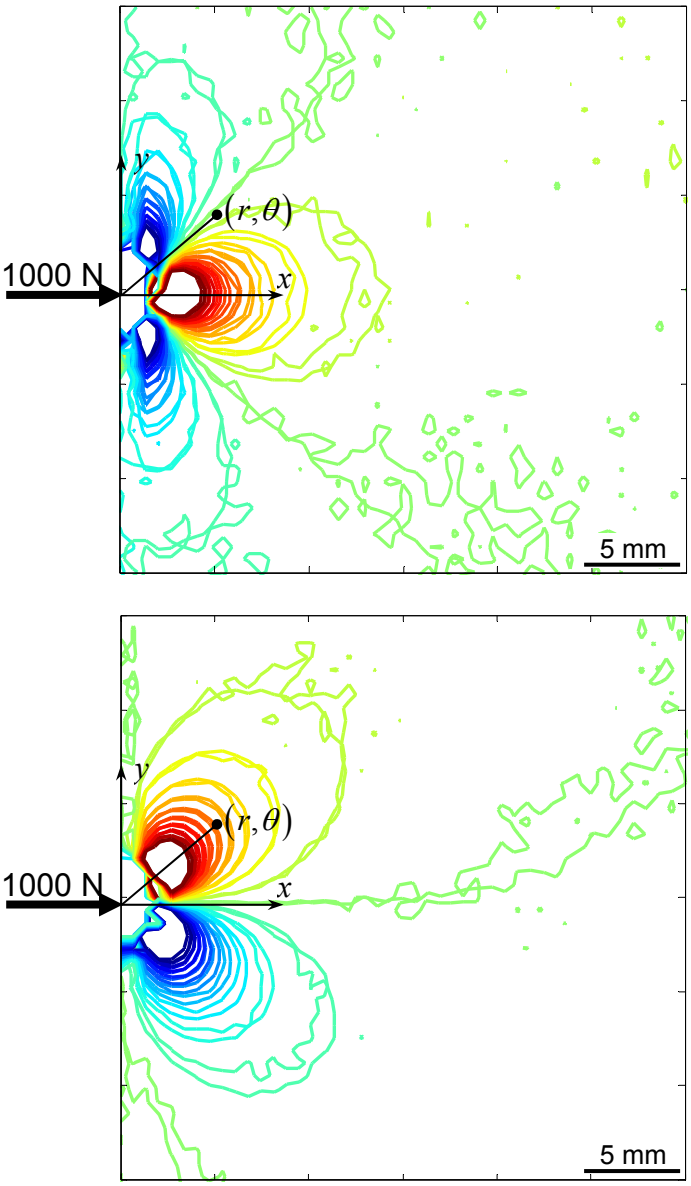

Figure 3.12: Contour plots of ϕ_x (top) and ϕ_y (bottom) obtained using different Δ (22.7 and 41.9 mm) corresponding to a PMMA sheet subjected to line-load on one of its edges.

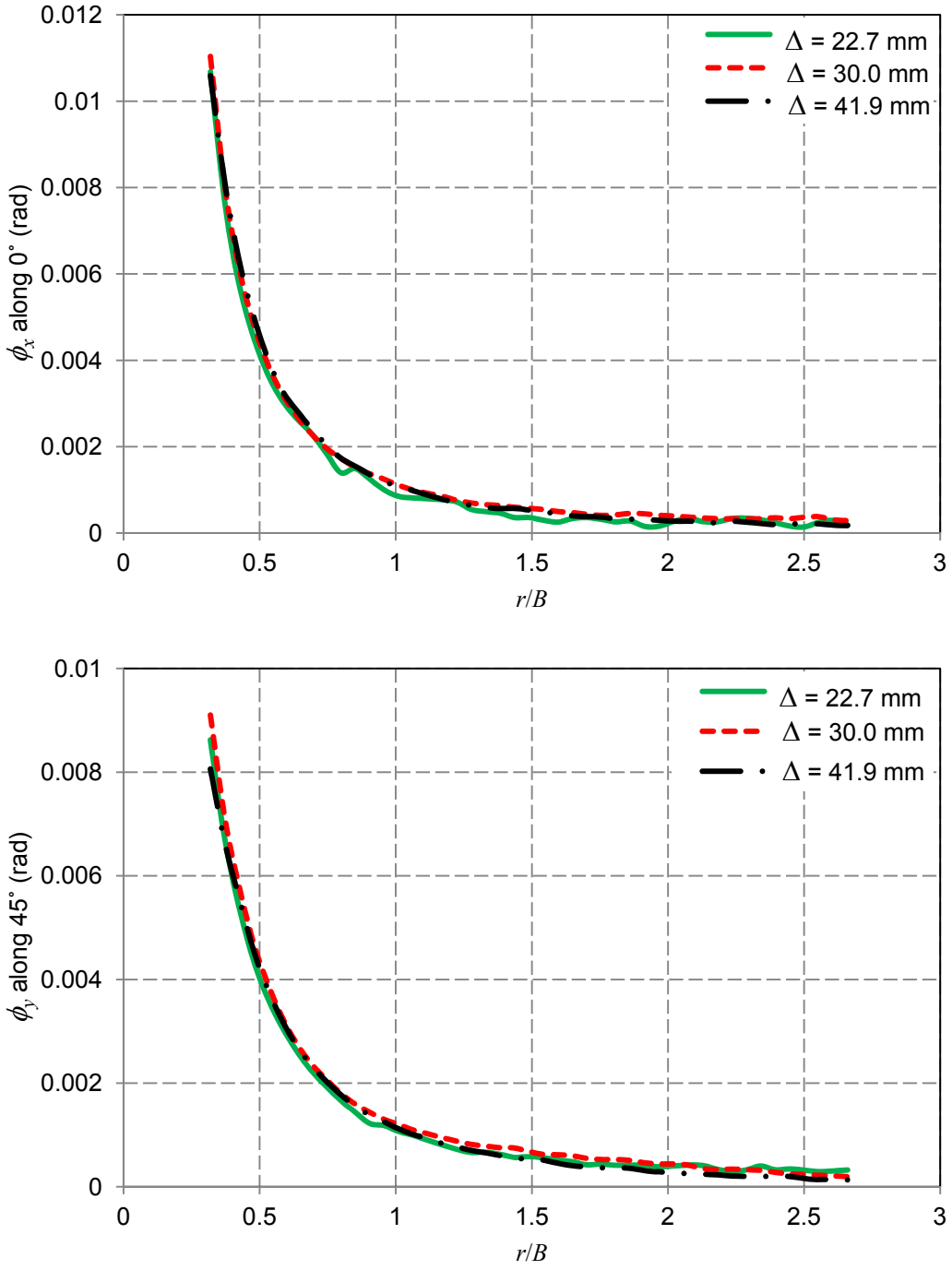

Figure 3.13: Radial variation of ϕ_x along 0˚ and ϕ_y along 45˚ obtained using Δ (22.7, 30.0 and 41.9 mm) corresponding to a PMMA sheet subjected to line-load on one of its edges.

In order to examine this effect, a PMMA sheet of thickness B = 9.4 mm was subjected to the line-load experiment similar to the one in Section 3.5 using three different Δ values, 22.7 mm, 30 mm and 41.9 mm. The load applied was 1000 N which introduced a stress gradient field near the loading point. The reference and deformed image pairs corresponding to the three Δ values were correlated using DIC. Figure 3.12 shows the contours of ϕ_x and ϕ_y corresponding to the smallest and largest Δ's superposed on one another. The noisier contour lines correspond to Δ = 22.7 mm, which is to be expected as discussed earlier in this section. Figure 3.13 shows the radial variations of ϕ_x and ϕ_y along 0˚ and 45˚, respectively. The noise corresponding to Δ = 22.7 mm observed in the contour plots is evident in Fig. 3.13 as well. Particularly, it can be seen that the noise is pronounced in regions of relatively low angular deflection values (farther from the stress riser). Therefore, during analysis, an appropriate Δ should be chosen guided by the expected angular deflection magnitudes as well as the accuracy offered by the DIC process.

4

Line-Load on the Edge of a Planar Sheet: Static Case

The study of a stress concentration problem using DGS is documented in this chapter. Details on the experimental setup, measurements and comparison between measured and analytical quantities are included. A transparent planar sheet of PMMA is subjected to a quasi-static line-load on its edge which resulted in a singular stress field near the loading point. This stress gradient field is measured using the DGS method. Subsequently, measurements are used to estimate stresses in the load point vicinity with the aid of the analytical solution for the problem. The feasibility of estimating the stress field via numerical integration of either of the two orthogonal stress gradients is also examined.

4.1 Experimental details

The specimen used for this experiment was a 180 x 69.5 mm^2 rectangular sheet of clear PMMA (Young's modulus = 3.3 GPa, Poisson's ratio = 0.35 and $C_\sigma \sim -0.90\times10^{-10}$ m^2/N) of thickness (B) 9.4 mm. A photograph of the experimental setup is shown in Fig.

4.1. The specimen was placed on a flat rigid platform and subjected to line-loading using a cylindrical steel pin (diameter 7.7 mm). An Instron 4465 universal testing machine was used for loading the specimen in displacement control mode (cross-head speed 0.005 mm/sec). A target plate painted with random black and white speckles was placed at a distance $\Delta = 30$ mm away from the specimen mid-plane (Fig. 2.1). A few heavy black dots were marked on the speckle plane to relate the image dimensions to the actual specimen/target dimensions.

A Nikon D100 digital SLR camera with a 28-300 mm focal length lens (aperture setting #11) and an extension tube were used to record speckles through the specimen in the load point vicinity. The camera was situated at a distance (L) of approximately 1040 mm from the specimen. A reference image of the target was recorded through the transparent specimen in the region of interest at a small load of a few Newtons (< 10 N). As the load was increased gradually, speckle images were recorded using time-lapse photography (12 frames per minute). One of the speckle images in the load point vicinity corresponding to a 3520 N load is shown in Fig. 4.2. It shows that due to specimen deformation, the speckles are noticeably blurry very close to the loading point whereas they appear relatively unaffected at far-away locations. The digitized speckle images (1504 x 1000 pixels) recorded at different load levels were correlated with the one corresponding to the reference condition using a 2D digital image correlation software ARAMIS®. As described previously, an array of in-plane speckle displacements on the target plane (and hence the specimen plane) was evaluated and converted into local angular deflections of light rays ϕ_x and ϕ_y. A facet/sub-image size of 15 x 15 pixels (1

pixel = 36.5 μm on the target plane) without any overlap was used in the image analysis for extracting displacement components.

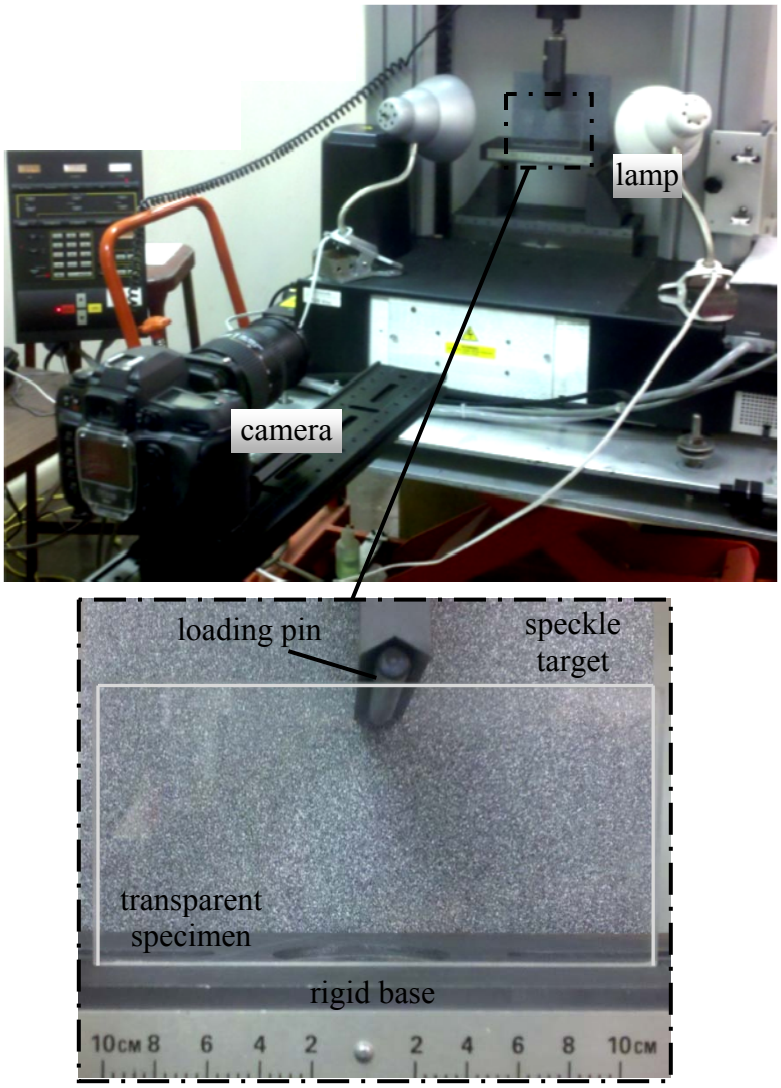

Figure 4.1: Photograph of the experimental setup used for studying stress concentration caused by a line-load acting on the edge of a large PMMA sheet (top). The close-up (below) shows loading pin resting on the top edge of the transparent specimen and speckles on the target.

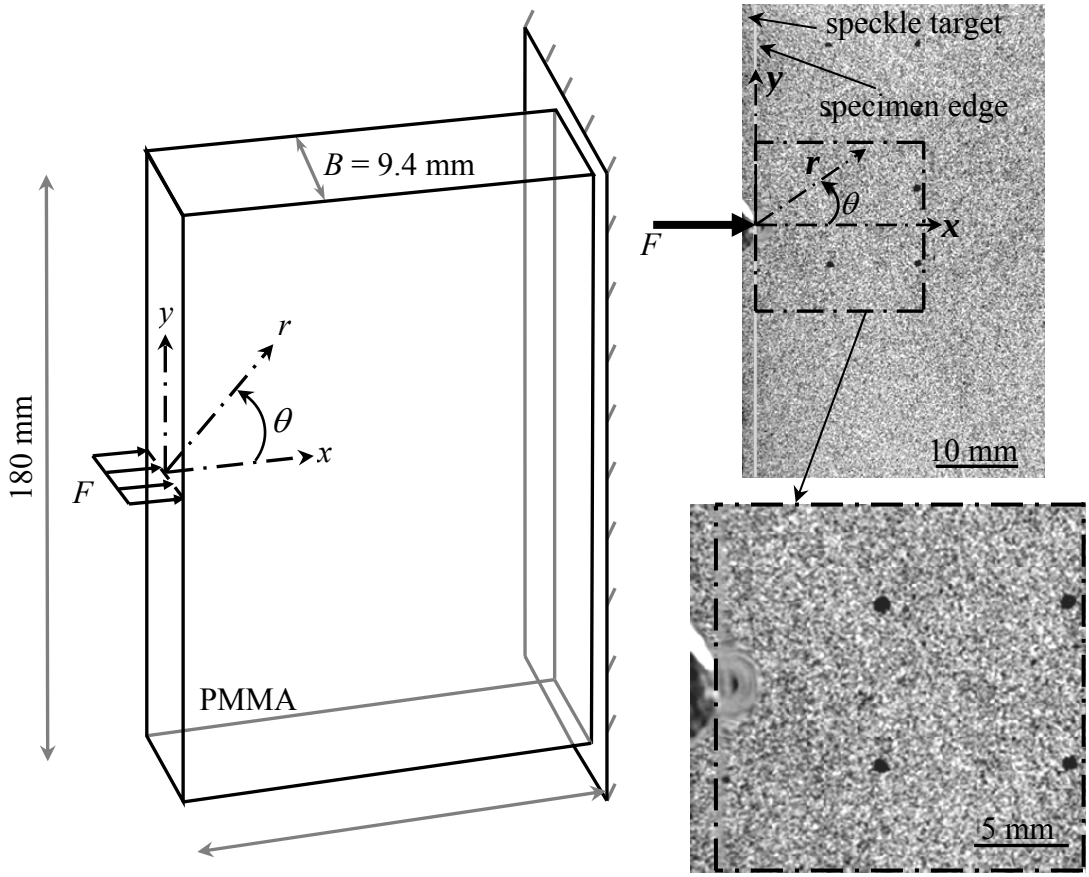

Figure 4.2: Schematic of the line-load acting on a half-space (left) and an actual speckle image recorded (right). Note the blurred/distorted region adjacent to the loading pin in the enlarged speckle image.

4.2 Comparison of measurements and analytical solution

Figure 4.3 shows the resulting contours of ϕ_x and ϕ_y for three representative load levels in a reduced square region around the loading point. It is important to note that, accounting for rigid body motions and imposing the appropriate boundary conditions of the problem to quantify the contour levels for further analysis is needed. That is, in the current problem, the boundary conditions such as equal but asymmetric stress gradient in

the *y*-direction relative to the *x*-axis, symmetric stress gradients in the *x*-direction about the *x*-axis, vanishing stress gradients far away from the loading point and stress free surfaces along the loading edge of the specimen could all be used.

Knowing that the plane stress field, near the line-load acting on an elastic half-space is described by Flamant problem [43] for which,

$$\left(\sigma_{xx}+\sigma_{yy}\right)=\sigma_{rr}=-\frac{2F}{\pi B}\frac{\cos\left(\theta\right)}{r},\ \sigma_{\theta\theta}=0,\ \sigma_{r\theta}=0, \tag{4.1}$$

where F is the applied load, B is the thickness of the half-space and $\left(r,\theta\right)$ are the polar coordinates, as shown in Fig. 4.2. Note that the hoop and shear stresses vanish in this solution. Further, $\left(\sigma_{xx}+\sigma_{yy}\right)=\left(\sigma_{rr}\right)$ for plane stress, and the radial stress σ_{rr} becomes singular/unbounded as the loading point ($r\to 0$) is approached. From Eqs. (2.10) and (4.1),

$$\phi_x=C_\sigma B\frac{\partial\left(\sigma_{rr}\right)}{\partial x}\quad\text{and}\quad\phi_y=C_\sigma B\frac{\partial\left(\sigma_{rr}\right)}{\partial y}. \tag{4.2}$$

Using Eqs. (4.1) and (4.2), the expressions for ϕ_x and ϕ_y fields become,

$$\phi_x=C_\sigma B\frac{2F}{\pi B}\frac{\cos\left(2\theta\right)}{r^2},\quad\phi_y=C_\sigma B\frac{2F}{\pi B}\frac{\sin\left(2\theta\right)}{r^2}. \tag{4.3}$$

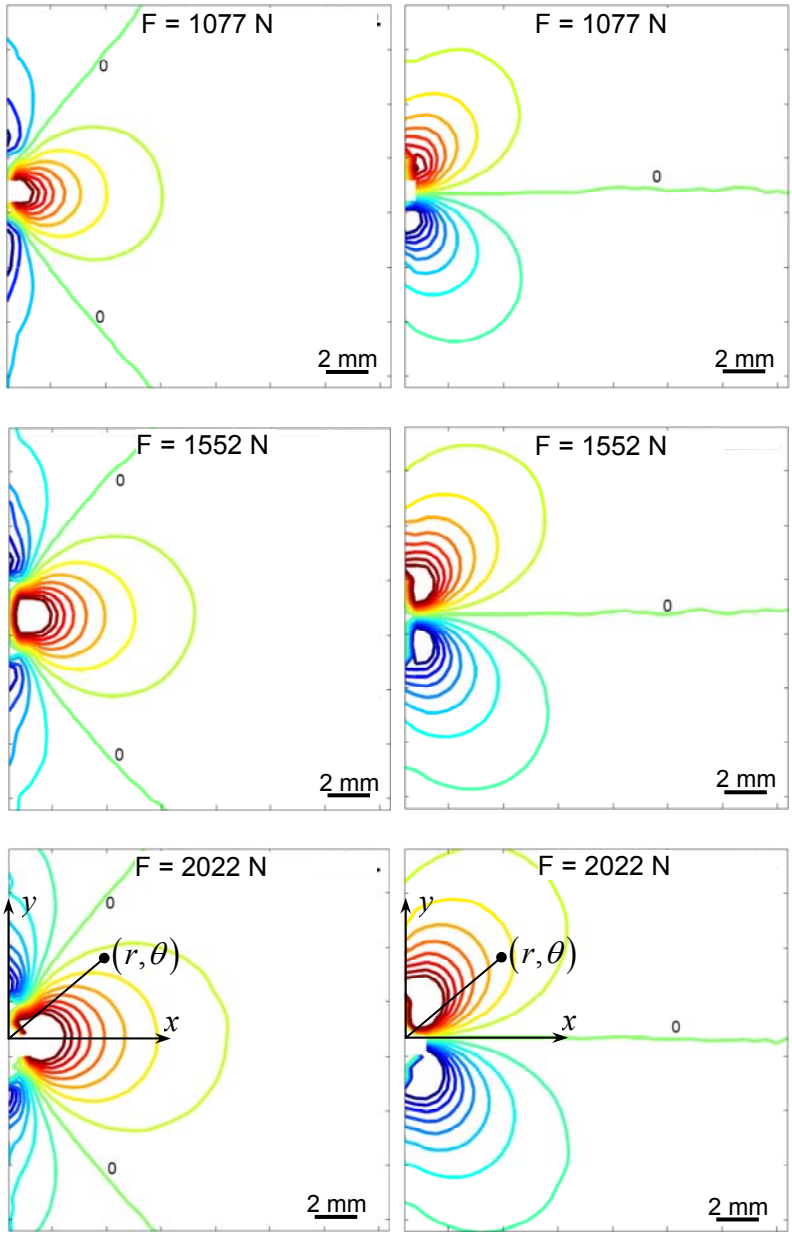

Figure 4.3: Measured ϕ_x (left) and ϕ_y (right) contours near the loading point for different load levels. Contour interval = 1 x 10^{-3} radian. (The left vertical edge of each image corresponds to the loading edge where F acts at the origin.)

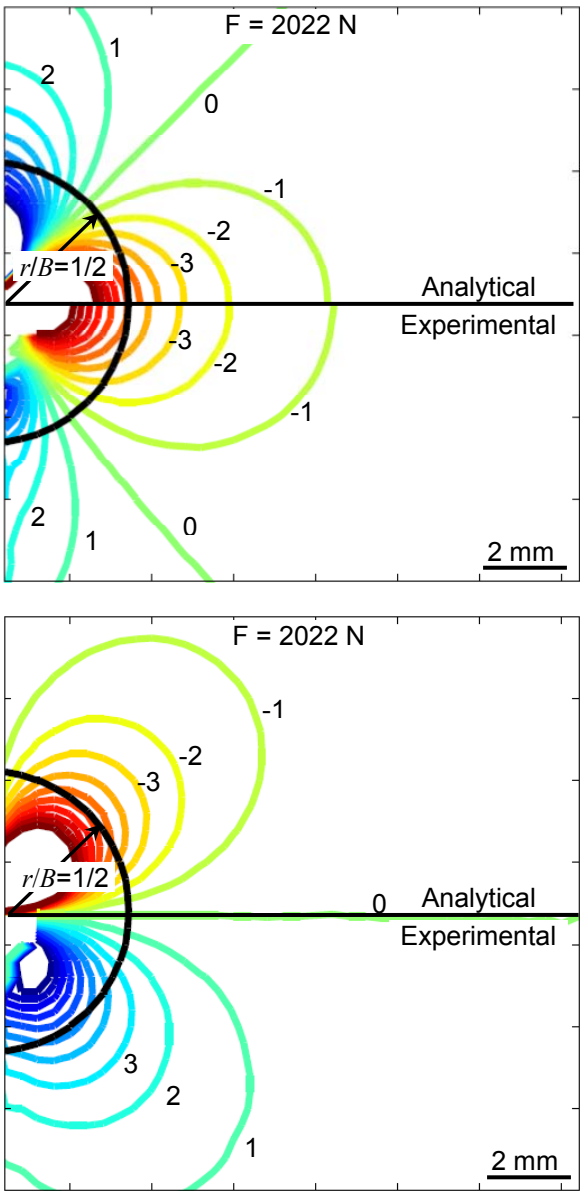

Figure 4.4: Comparison of experimental and analytical angular deflection (top: ϕ_x and bottom: ϕ_y) contours for F = 2022 N. Contour levels are in 1×10^{-3} radians.

For comparison, the experimental and analytical angular deflection contours for a representative load case of F = 2022 N are shown in Fig. 4.4. The dominant stress triaxiality where plane stress assumptions are violated is expected in regions close to the

loading point. In cracked bodies where a stress singularity of $r^{-1/2}$ occurs, a region of dominant stress triaxiality is shown to exist near the crack-tip ($0 \le r/B \le 1/2$) [28]. Based on that observation, it is reasonable to expect that stress triaxiality dominates over a region of similar size in the current case as well (verification of this assumption is provided in Appendix A1).

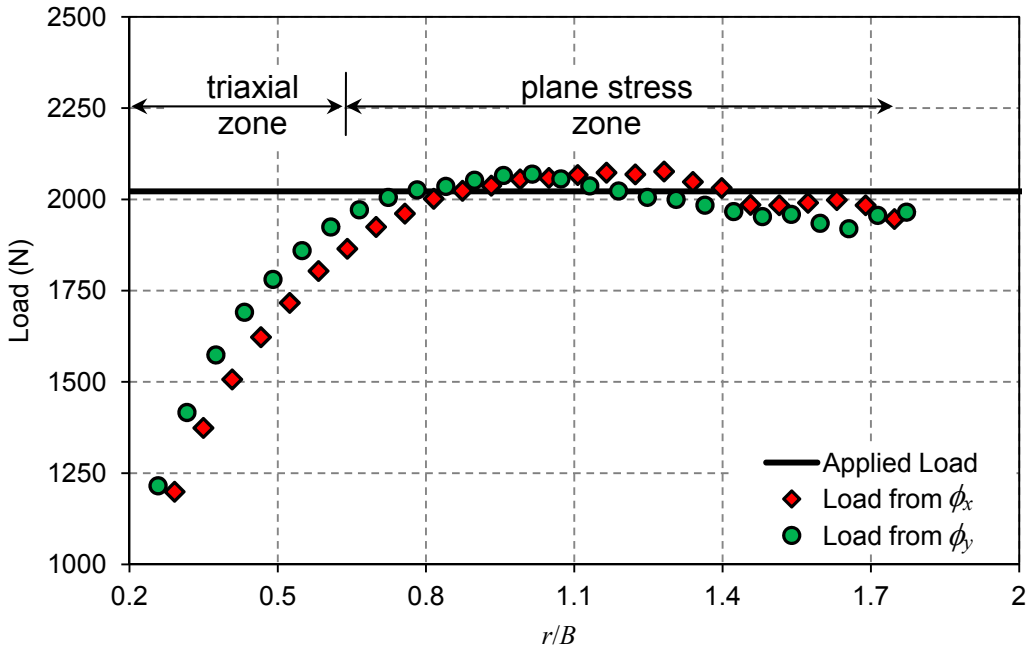

Figure 4.5: Comparison of experimentally extracted load to the known applied load; quasi-static line-load problem.

Accordingly, a good agreement between analytical solutions and experimental measurements are not expected at least up to r/B = 0.5. This region is shown in Fig. 4.4 as the one bounded by a semi-circle centered at the origin. In the regions outside the zone of dominant triaxiality, a good qualitative and quantitative agreement between experimental and analytical contours is apparent. The ϕ_x and ϕ_y data corresponding to a

particular applied load can be used to back calculate the load using Eqs. (4.3). Figure 4.5 shows the plot of calculated load at each measurement point (sub-image) as a function of r/B along $\theta = 0°$ and $\theta = 45°$ from ϕ_x and ϕ_y fields, respectively, for the case of $F = 2022$ N. From the graph, it can be seen that, after an initial non-conformity up to $r/B \sim 0.5$-0.6, the extracted load values agree with the applied load quite well.

4.3 Estimation of Stresses from Stress Gradients

Since DGS is capable of measuring stress gradients in two orthogonal directions simultaneously, one can estimate the stresses $\left(\sigma_{xx} + \sigma_{yy}\right)\left(= \sigma_{rr}\right.$ in this case) for this particular case only, in the region of interest from measured stress gradients. This can be done as follows:

Using Eqs. (4.3), the resultant of ϕ_x and ϕ_y can be obtained as,

$$\phi = \sqrt{\phi_x^{\,2} + \phi_y^{\,2}} = C_\sigma B \frac{2F}{\pi B r^2}. \tag{4.4}$$

Evidently, the expression for ϕ in Eq. (4.4) is independent of θ suggesting that contours of ϕ are circular (semicircular in this case) relative to the origin.

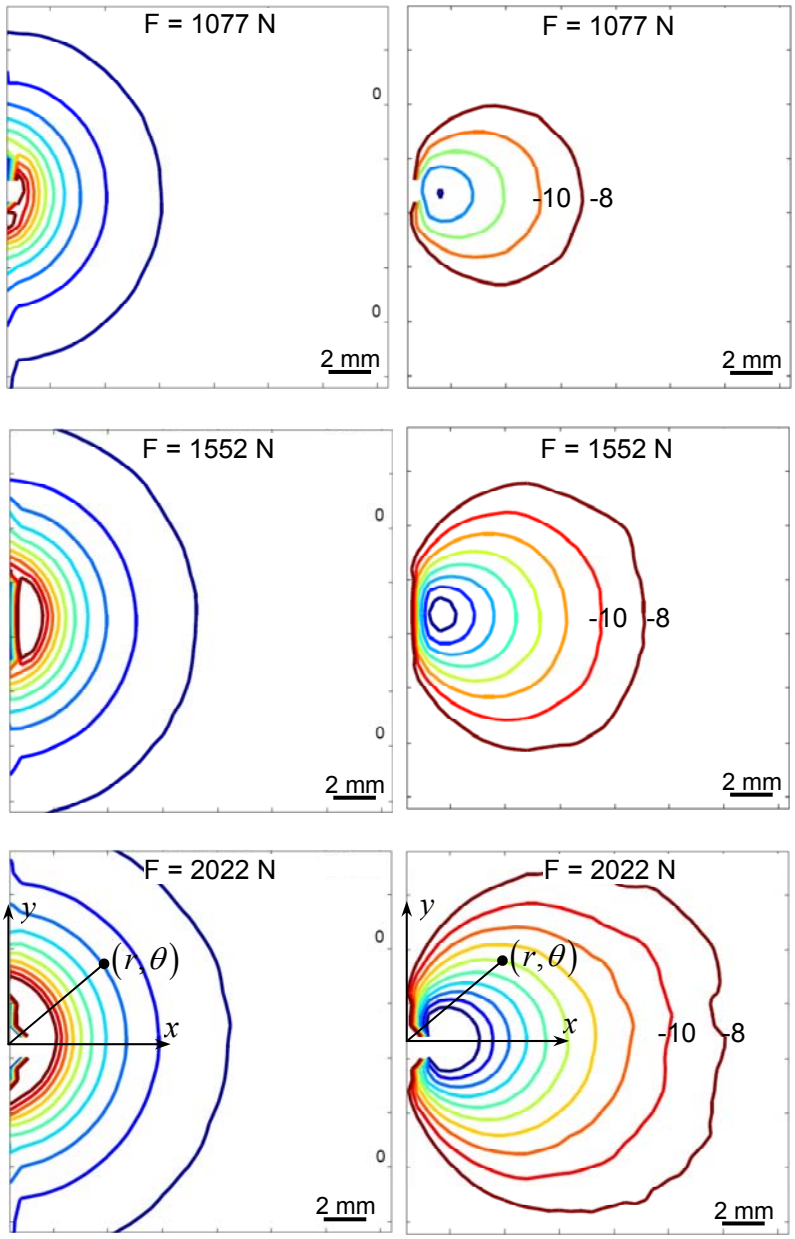

Figure 4.6: Measured resultant angular deflection of light rays ϕ (left) and estimated radial stress σ_{rr} (right) contours for various load levels. Contours are plotted every 1 x 10^{-3} radian and 2 MPa, respectively. (The left vertical edge in each image is the edge where the line-load acts horizontally at the origin.)

This can be verified by generating contours of ϕ from measured ϕ_x and ϕ_y. That is, for each facet/sub-image, ϕ was computed in the load point vicinity. The first column in Fig. 4.6 shows the measured contours of ϕ for the three load levels considered in Fig. 4.3. The resulting contours are indeed semicircular (except near the free edge of the specimen where edge effects affect ϕ_x and ϕ_y computations) centered about the loading point, confirming the prediction by the Flamant's solution. A direct comparison of measured ϕ values with the predicted ones from Flamant's solution is presented in Fig. 4.7 (top) for a representative case showing a good agreement between the two. Now, by inspecting the analytical expressions of ϕ (Eq. (4.4)) and Eq. (4.1), it becomes clear that stress σ_{rr} $(=\sigma_{xx}+\sigma_{yy})$ can be estimated under plane stress conditions by simply multiplying ϕ values with the corresponding $(r\cos\theta)$ values if ϕ data are available from experimental measurements as,

$$\left(\sigma_{xx}+\sigma_{yy}\right)=\sigma_{rr}=\frac{\phi}{C_\sigma B}\left(r\cos\theta\right). \tag{4.5}$$

The second column in Fig. 4.6 shows the stress contours thus obtained for all the three load levels considered in Fig. 4.3. The contour plots of the experimentally estimated and analytical stress fields for a representative case of F = 2022 N are shown in Fig. 4.7. Again a good agreement between the estimated and predicted contours of normal stress σ_{rr} near the loading point where plane stress conditions exist is seen demonstrating the viability of DGS method for stress estimation purposes besides stress gradient measurement in this case.

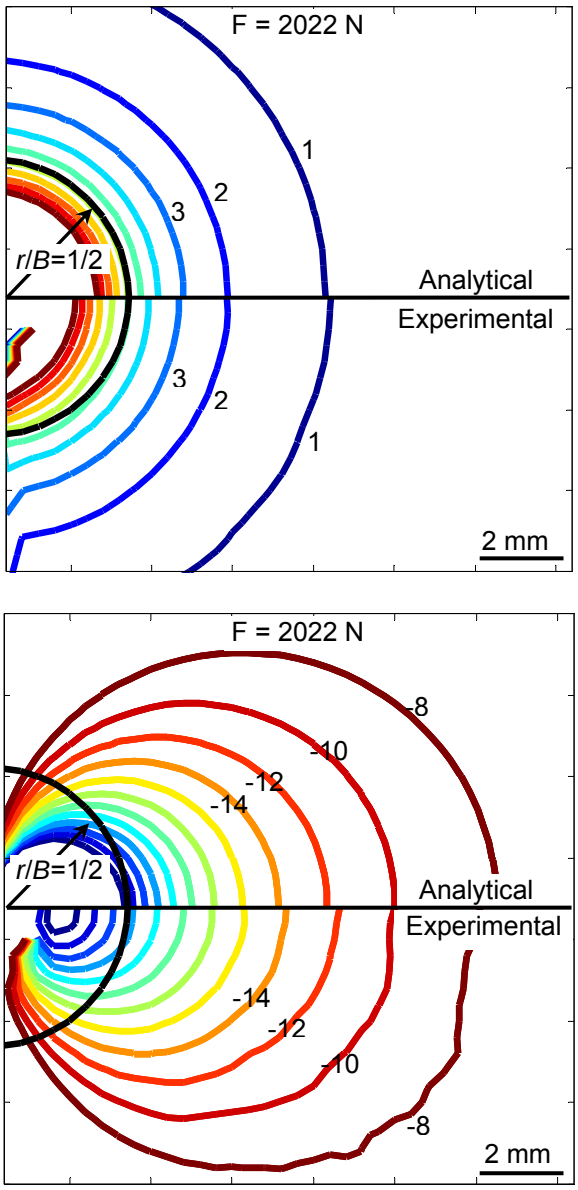

Figure 4.7: Comparison between experimental and analytical ϕ contours (top; contour interval = 1×10^{-3} radian), and radial stress (σ_{rr}) contours (bottom; contour interval = 2 MPa) for F = 2022 N.

4.4 Stress estimation by numerical integration

Previously the stress fields were estimated using ϕ_x, ϕ_y, ϕ along with the analytical field equations for $\left(\sigma_{xx}+\sigma_{yy}\right)$. In practice, however, the analytical field equations may not be known *a priori*. In such situations, stresses can be estimated by direct numerical integration of measured angular deflection fields. This, however, requires knowledge of far field stresses and stress gradients in one or both Cartesian directions depending upon the nature of the integration scheme adopted. For example, the stress field $\left(\sigma_{xx}+\sigma_{yy}\right)$ from the angular deflection fields can be obtained as,

$$\begin{aligned}\left(\sigma_{xx}+\sigma_{yy}\right) &= \frac{1}{C_\sigma B}\int_0^b \phi_x(x,y)\,dx + C_1,\\ \left(\sigma_{xx}+\sigma_{yy}\right) &= \frac{1}{C_\sigma B}\int_0^d \phi_y(x,y)\,dy + C_2,\end{aligned} \tag{4.6}$$

where C_1 and C_2 denote integration constants along constant y and x coordinates, respectively. In the present case of a line-load acting on a half-space, the stress gradients (or angular deflections of light rays) vanish at far-away locations from the loading point. That is, as $x \to \infty$, $\phi_x \to 0$ and $C_1 \to \left(\sigma_{xx}+\sigma_{yy}\right)_{x=\infty}$, the value of the stress invariant in the far-field if ϕ_x field is considered for integration. In practice, however, experimental limitations do not allow recording of speckles at sufficiently far away distances with sufficiently high resolution. In such cases, the *x*- and *y*-coordinates of the region of interest are bounded by say, ($x = b$, y) and (x, $y = d$), respectively, as implied in Eq. (4.6). The integration constants can be evaluated in these cases as $C_1 = \left(\sigma_{xx}+\sigma_{yy}\right)_{(x=b,\,y)}$ or

$C_2 = \left(\sigma_{xx} + \sigma_{yy}\right)_{(x,y=d)}$ provided stress gradients are negligibly small or known at ($x = b$, y) or (x, $y = d$).

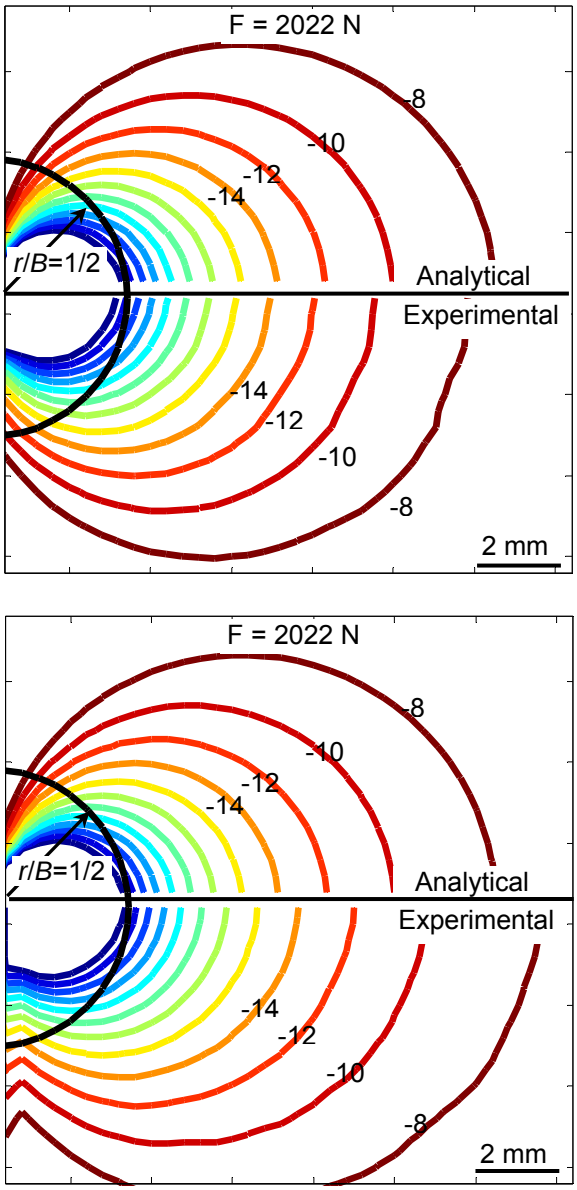

Figure 4.8: Comparison of analytical and experimental stress invariant contours obtained by cumulative numerical integration of ϕ_x (top) and ϕ_y (bottom) fields. Contour interval = 2 MPa.

To demonstrate the feasibility of extracting $\left(\sigma_{xx}+\sigma_{yy}\right)=\sigma_{rr}$ by numerical integration, the gradient field ϕ_x and ϕ_y corresponding to the load level, F = 2022 N were integrated using a simple trapezoidal rule in increments of one facet/sub-image size. The constants of integration C_1 along ($x = b$ = 35.6 mm, y) for this case were obtained using Flamant's solution (alternatively, a simple finite element computation to evaluate stresses along ($x = b$=35.6 mm, y) could be used as well). The resulting stress fields obtained from integrating the ϕ_x and ϕ_y fields are shown in Fig. 4.8. As observed, the stress contours obtained from the ϕ_y field have more pronounced experimental error relative to the analytical stress contours than the ones from the ϕ_x field. This is in part due to the practical inability to choose a larger d (in order to make the "$\phi_y = 0$ in the far field" assumption more appropriate).

5

Line-Load on the Edge of a Planar Sheet: Dynamic Case

This chapter details the feasibility study of the DGS method to study material failure/damage in transparent planar sheets subjected to a transient line-load acting on an edge. Ultra high-speed digital photography is used to record the speckles and hence the deformation in the load point vicinity. The dynamic measurements are examined relative to the finite element computations before observed material failure. The measured stress gradients near the impact point after damage initiation are also presented and failure behavior is discussed.

5.1 Experimental details

A schematic of the experimental setup developed for studying the problem of dynamic line-load acting on the edge of a planar sheet using DGS is shown in Fig. 5.1, and Fig. 5.2 shows the actual photograph of the actual setup. The loading device consisted of an Al 7075-T6 long-bar (2 m long, 25.4 mm diameter) with a cylindrical (bull-nose) head, a gas-gun and a high-speed digital image acquisition system. The long-

bar was aligned with the gas-gun barrel containing a 305 mm long, 25.4 mm diameter cylindrical striker also made of aluminum. A Cordin model-550 ultra high-speed digital camera equipped with 32 CCD sensors and a five-facet rotating mirror, and two high-energy flash lamps was used for recording speckles on the target plane. A computer connected to the camera was used to control parameters such as trigger delay, flash duration, framing rate and image storage. The specimen, a 129 × 67.5 × 9.4 mm^3 clear PMMA plate, was placed on an adjustable platform and its long edge was registered against the cylindrical head of the long-bar as shown in Fig. 5.2. The loading was initiated by suddenly releasing the compressed air in the gas-gun cylinder using a solenoid valve to propel the striker placed inside the barrel. The accelerating striker impacted the long-bar and initiated a compressive stress wave that traveled the length of the bar before imparting a transient line-load to the edge of the specimen.

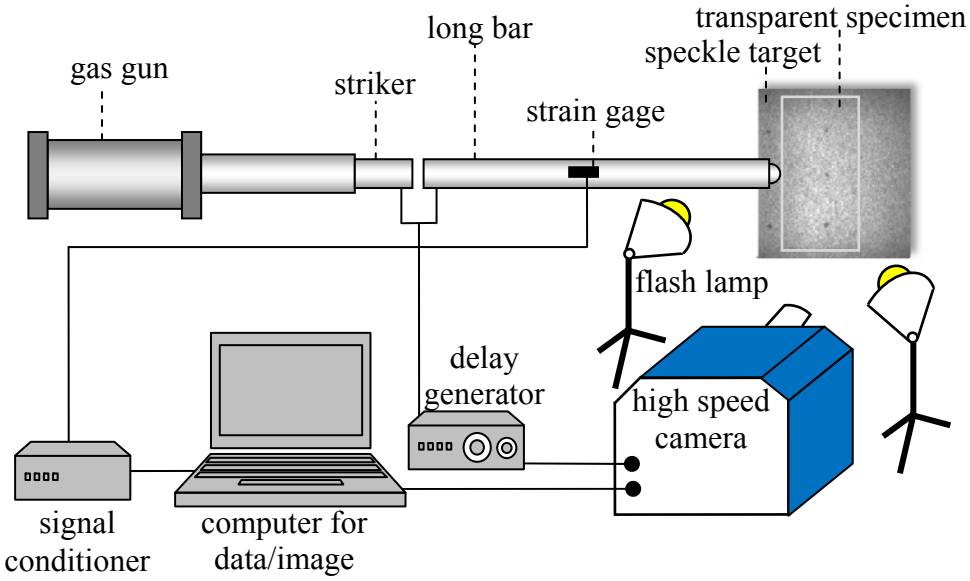

Figure 5.1: Schematic of the dynamic line-load experiment.

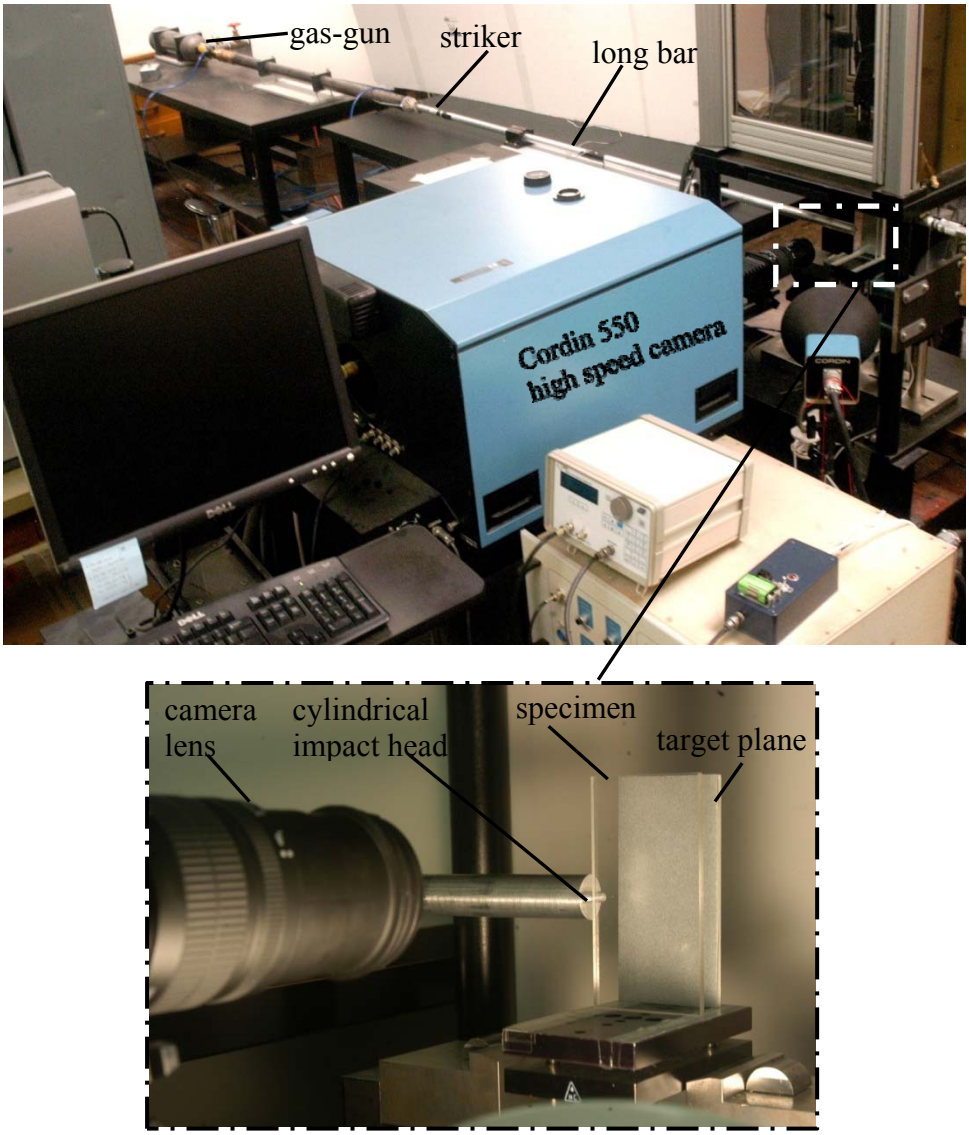

Figure 5.2: Experimental setup used to measure angular deflections of light rays caused by a deforming transparent specimen when subjected to dynamic line-load (top). Close-up of the specimen, speckle target, and the long-bar (bottom).

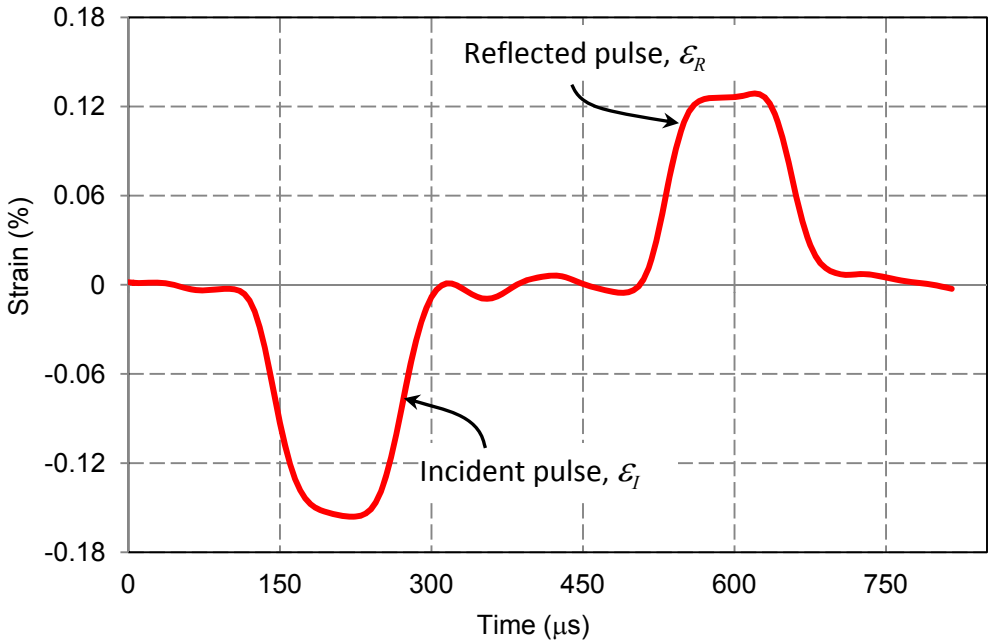

Figure 5.3: Measured strain history in the long-bar used to deliver a dynamic line-load on the edge of the transparent PMMA specimen. (time = 0 corresponds to the start of data acquisition and not impact loading)

An electrical circuit, completed when the striker contacted the long-bar, was used to trigger a delay generator which in turn activated the camera with a user-specified delay. A strain gage (CEA-13-062UW-350 from Vishay Micro-measurements) affixed to the long-bar, and connected to a LeCroy digital oscilloscope via an Ectron signal conditioner, was used to measure the strain history (Fig. 5.3) in the long-bar during loading [44]. The measured strain history was used to calculate the particle velocity history in the specimen at the specimen/bar interface. The distance between the specimen and the camera lens plane (L) was ~1000 mm and the one between the specimen mid-plane and the target plane (Δ) was 30 mm.

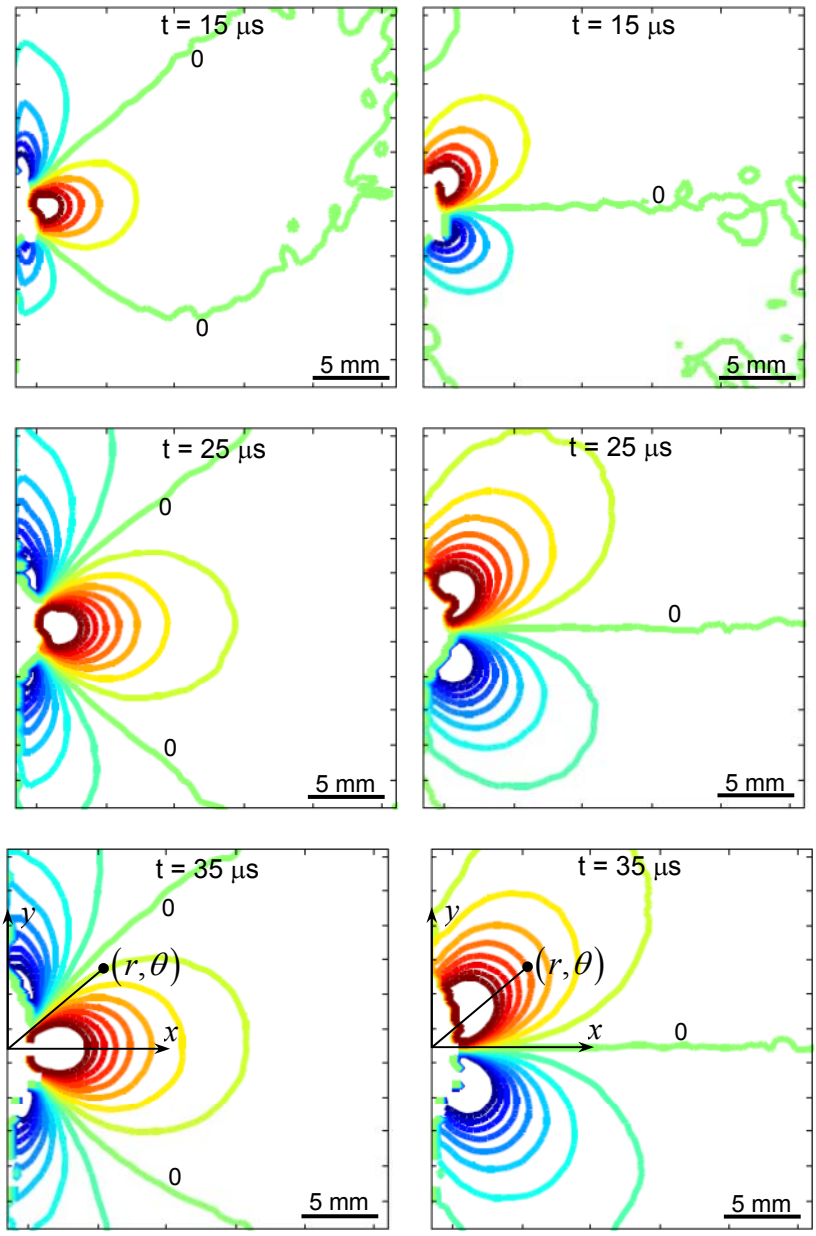

Figure 5.4: Measured ϕ_x (left) and ϕ_y (right) contours near the loading point for different time instants. Contour interval = 1 x 10^{-3} radian. (The left vertical edge corresponds to the loading edge with impact load *F(t)* acting at the origin along the *x*-axis.)

A set of 32 reference (undeformed) images, one for each sensor, were first captured under no-load condition at 200,000 frames per second. Next, the specimen was subjected to a dynamic line-load using the long-bar setup. During loading, a set of 32

consecutive images of the specimen undergoing deformation were captured at the same framing rate. The deformed-undeformed image pairs for each of the 32 CCD sensors were then correlated to obtain the in-plane displacement fields, δ_x and δ_y. A facet/sub-image size of 15 x 15 pixels (1 pixel = 29.2 μm on the target plane) without any overlap was used in the image analysis for extracting displacement components. The displacement fields were then used to compute the angular deflection fields (ϕ_x and ϕ_y), and are shown in Fig. 5.4. Appropriate boundary conditions were imposed as discussed in Chapter 4 for quantifying the contour levels.

5.2 Comparison of measurements and numerical solution

The dynamic angular deflection fields were also numerically obtained by performing an elasto-dynamic finite element (FE) analysis to compare with the measured fields. The elastic modulus and Poisson's ratio of PMMA used in the simulation were from ultrasonic pulse-echo measurement of longitudinal and shear wave speeds [45] and mass density. Using the measured incident strain history, $\varepsilon_I(t)$, in the bar during loading, and the measured parameters listed in Table 5.1, the transmitted particle velocity, V_T, was calculated using [46],

$$V_T = V_I \frac{2\rho_I C_I A_I}{\rho_I C_I A_I + \rho_T C_T A_T}, \tag{5.1}$$

where $V_I = C_I \varepsilon_I$ is the particle velocity in the incident bar, and ρ, C, and A denote the mass density, bar wave speed and area, respectively, and subscripts I and T denote the

incident and transmitted values. The area values used in this work were assumed to be proportional to length over which stress wave transmission occurred.

Parameter	Value
Density of bar material (Al 7075-T6)	2730 kg/m^3
Longitudinal wave speed in bar	5700 m/s
Width of cylindrical head	25.4 mm
Density of specimen material (PMMA)	1010 kg/m^3
Longitudinal wave speed in PMMA	2657 m/s

Table 5.1: Material properties of long-bar and PMMA specimen used in the dynamic line-load experiment.

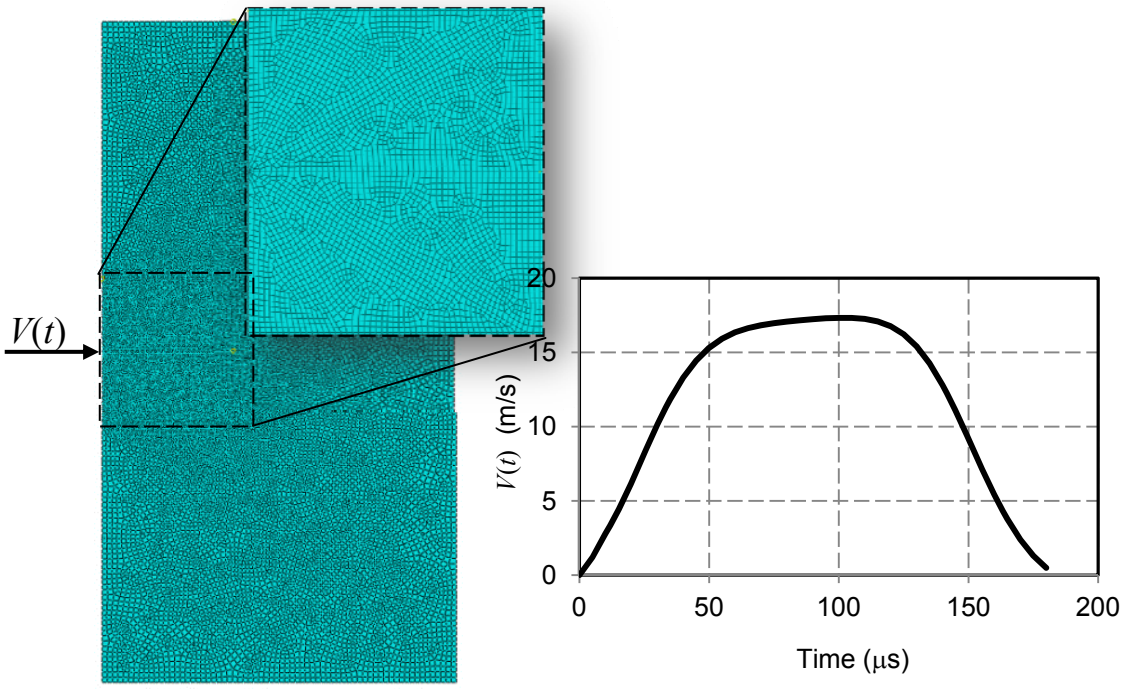

Figure 5.5: Discretized finite element model used to simulate a PMMA sheet experiencing a dynamic line-load (left) and particle velocity history (right) used as an input.

The transmitted particle velocity history shown in Fig. 5.5 was used as the input for FE computations using structural analysis software package ABAQUS. The FE model consisted of 17,004 four-node quadrilateral elements (total DOF = 33964) with the smallest element of size ~ 0.5 mm. The numerical model was solved using explicit time integration scheme and the instantaneous in-plane stress invariant $(\sigma_{xx} + \sigma_{yy})$ field near the loading point was obtained.

5.3 Extraction of dynamic force history from optical measurements

The representative $(\sigma_{xx} + \sigma_{yy})$ contours corresponding to the time instants in Fig. 5.4 are as shown in Fig. 5.6. From this field, the $(x, y, (\sigma_{xx} + \sigma_{yy}))$ data along $\theta = 0^o$, 30^o and 60^o were extracted and the in-built differentiation scheme in ABAQUS was used to compute spatial derivatives of $(\sigma_{xx} + \sigma_{yy})$ in the *x*- and *y*-directions. For comparison with measurements, these numerically obtained stress gradient data along with the experimental ones corresponding to a time instant 30 μs after the arrival of the stress waves at the specimen/bar interface are shown in Fig. 5.7. From the graphs, a rather good agreement between the computational and experimental results is evident beyond the triaxial zone ($r/B \sim 0.5$). The $(\sigma_{xx} + \sigma_{yy})$ contours in Fig. 5.6 are generally circular (except very close to the loading point) and are similar to the ones expected from the Flamant solution (Eq. (4.1)). This suggests that the functional form of the instantaneous deformation fields near the transient line-load can be approximated reasonably well by

the Flamant's equations. Accordingly, an attempt was made to use Eqs. (4.3) in the dynamic line-load problem to extract the load history.

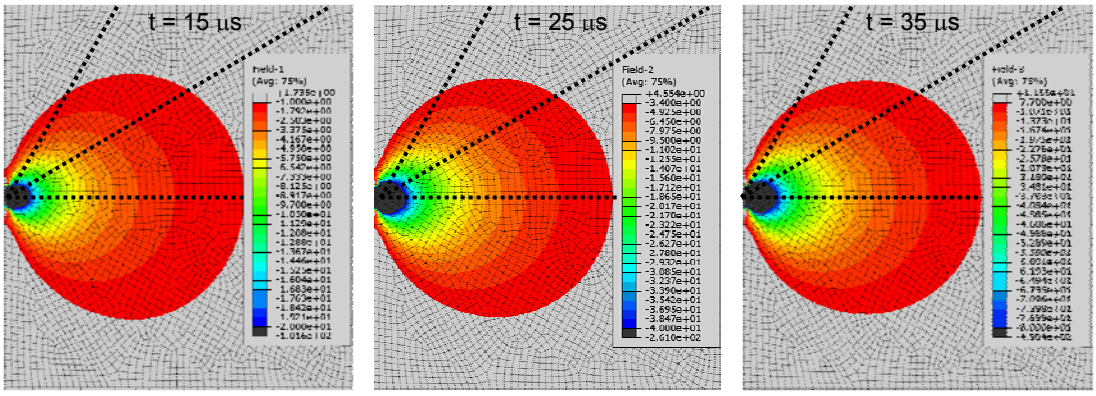

Figure 5.6: Contour plots of in-plane stress invariant at various time instants during the dynamic loading of PMMA from finite element analysis. Dotted lines correspond to paths along 0^o, 30^o and 60^o relative to the loading direction used for computing stress gradients.

Three sets of discrete values of angular deflection fields at various (r, θ) locations, excluding the immediate vicinity of the loading point (within r/B = 0.4, 0.5 and 0.6) where triaxial deformations dominate, were collected for each time instant. These values were then used along with Eqs. (4.3) to extract three values of the instantaneous load ($F(t)$) using an overdeterministic least-squares analysis [41] for every time instant. For each time instant, the intermediate value is plotted in Fig. 5.8 and the error bars show the upper and lower bounds of $F(t)$ resulting from three different data sets. The load history was also assessed from the strain gage measurements on the long-bar as, $F_b(t) = E_b A_b (\varepsilon_I + \varepsilon_R)_b$ where E_b (= 72 GPa) and A_b are the elastic modulus and cross-section area of the bar, respectively, and ε_I and ε_R denote incident and reflected strain signals.

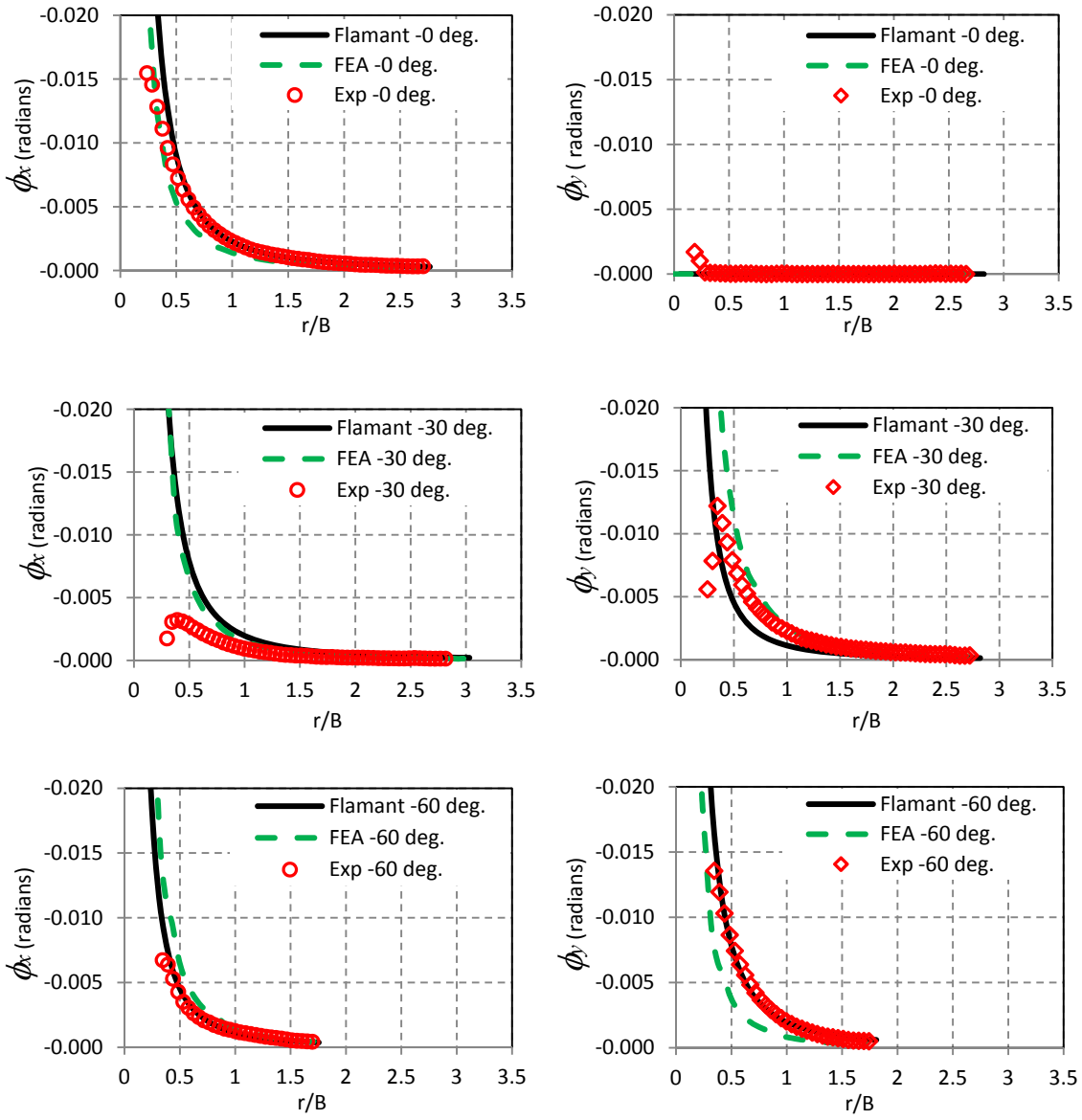

Figure 5.7: Comparison of analytical, finite element and experimental angular deflections (column 1: ϕ_x and column 2: ϕ_y) in PMMA plate subjected to a dynamic line-load at t = 30 μs.

Figure 5.8 shows a plot of measured load histories from the strain gage along with the ones from optical data analysis. The load history extracted using ϕ_x and ϕ_y fields and Eqs. (4.3) is in good agreement with the strain gage measurements until damage/failure initiation (at ~40 μs after impact) occurs at the loading point. Beyond that, the two results

noticeably deviate from each other. It is evident from the graph that just after the start of local crushing/pulverization of PMMA at ~40 μs, the measured load history starts to decrease for about 20 μs before rising again. These differences are to be expected as the closed form solutions used for optical data extractions do not hold in the post-failure regime.

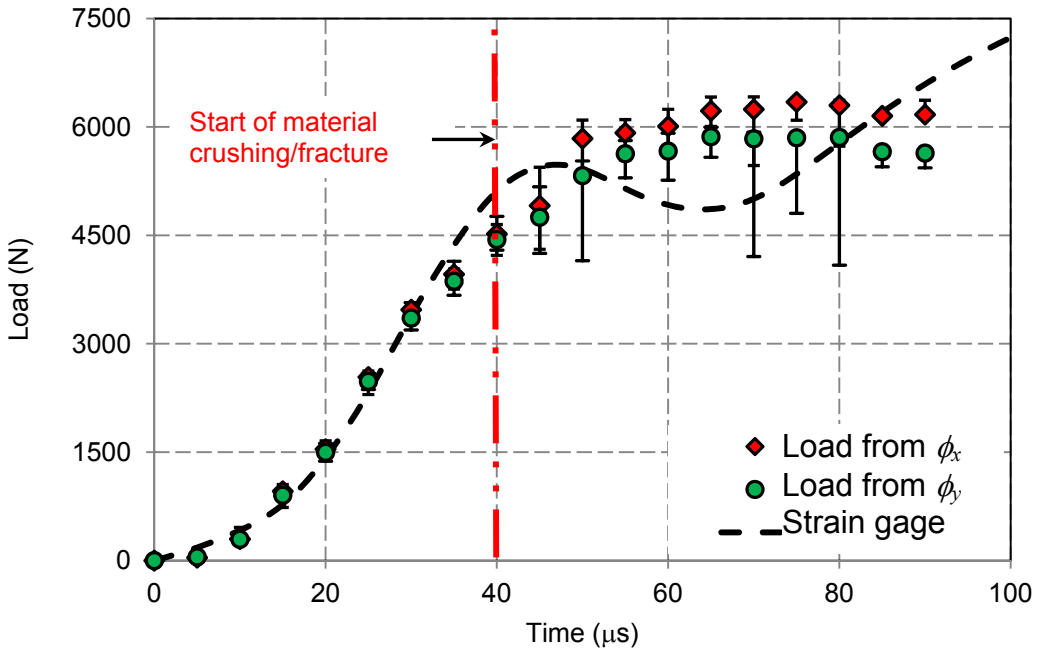

Figure 5.8: Load histories measured using DGS (symbols) and strain gage (broken line). The agreement between the two is good up to the start of the material crushing/cracking at the impact point.

Further, the local crushing and micro-cracking events of PMMA are sensed by the strain gage data as a drop in the signal whereas the load extracted by analyzing the optical data from undamaged regions away from the load point/s lag in revealing this least-

squares information. Furthermore, the optically extracted loads based on over-deterministic analysis provide an averaged response over the region.

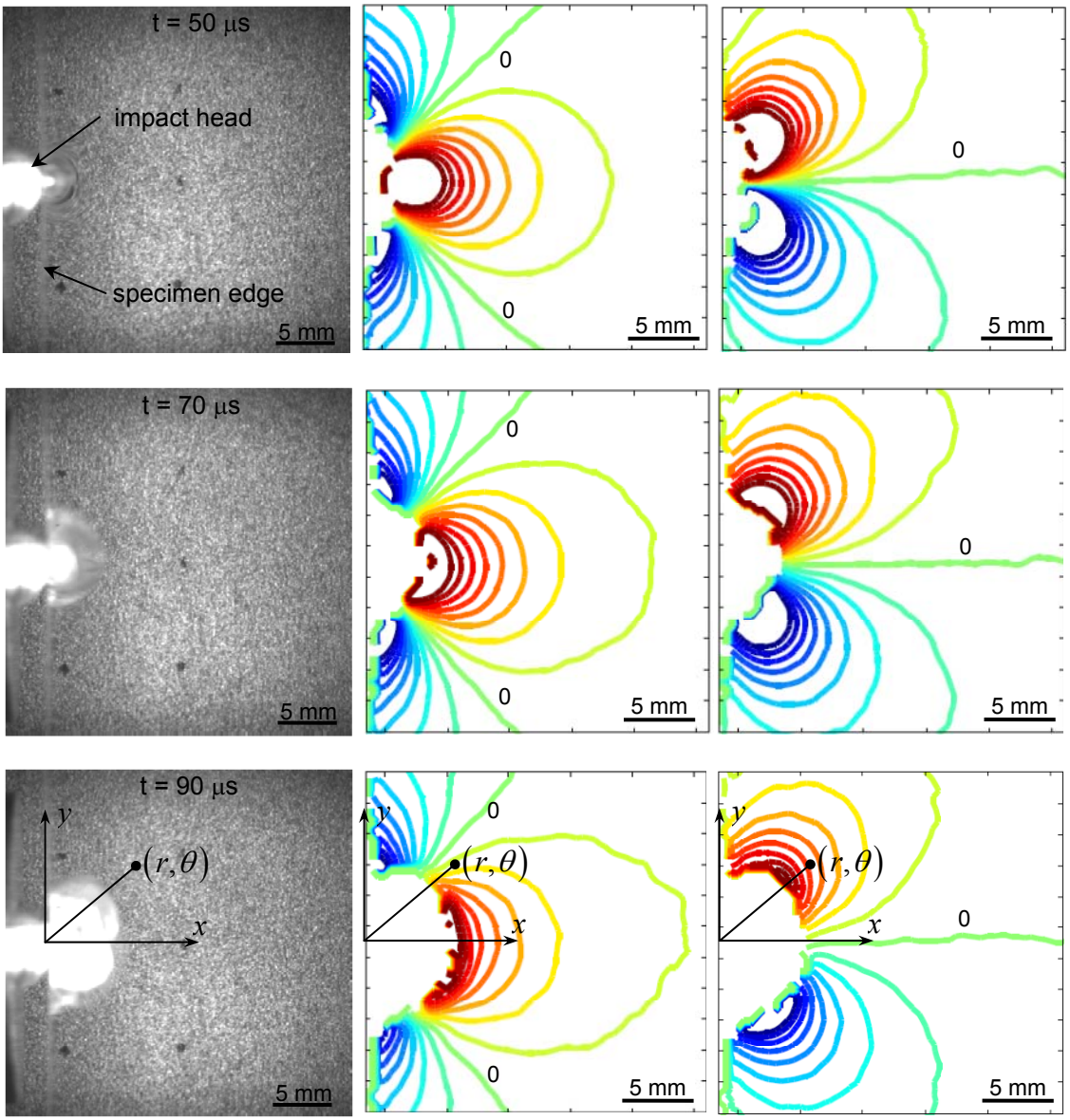

Figure 5.9: Failure progression (column 1) and corresponding angular deflection contours, ϕ_x (column 2) and ϕ_y (column 3) contours in PMMA plate subjected to a dynamic line-load. Contour interval = 1×10^{-3} radian.

The large error bars in the post-failure regime are due to the expanding zone of triaxiality as the failure front progresses (Fig. 5.9) during the dynamic event. Therefore,

the optical data used for least-squares analysis had to be collected well beyond $r/B = 0.5$, based on the position of the instantaneous damage front. These load *estimates* thus correspond to optical data analyzed using measurements from $1.0 < r/B < 1.8$. The corresponding errors in the post-failure regime were based on data analysis for different inner radii used during the analysis.

5.4 Stress gradients in the post-failure regime

The analytical and/or numerical solutions are generally valid only until the onset of failure - crushing and/or cracking. In addition, they are dependent on assumptions associated with failure modes and post-failure material behavior. In such scenarios, only direct experimental measurements offer reliable data for structural analyses/design. In view of this, stress gradients even after the material has undergone cracking and crushing near the loading point is also presented. The first column in Fig. 5.9 shows failure progression in the specimen after the initiation of failure at the loading point. This causes the image correlation to fail in the region of intense damage. The highly saturated (or, decorrelated) gray scale around the loading point represents the damaged zone. The second and third columns in Fig. 5.9 show contours of ϕ_x and ϕ_y. The observed changes in contour density and their shapes relative to the ones prior to damage initiation qualitatively indicate contributions of a smeared loading front as well as the arrival of the reflected stress waves from the far edges of the specimen to the load point vicinity. Figure 5.10 shows photographs of the failed specimen as well as a close-up of the load

point vicinity. Due to the dynamic load, PMMA is symmetrically chipped off from the plate relative to the mid-plane. However, there is a slight non-symmetry observed in the chip cavities about the loading axis. This can be attributed to the magnitude difference between the reflected stress waves from the top (free) and bottom (supported) edges of the plate. All of the compressive stress wave that reach the top free edge reflect as a tensile wave, whereas, part of the stress waves that reach the bottom (supported by denser than PMMA steel platform) edge get transmitted into the support and the rest reflect as a tensile wave, thereby causing a stress magnitude difference about the loading axis.

A close-up of the failure surface reveals the typical mirror and hackle regions. References [5, 6] describe the mechanisms involved in the formation of conical chips in glass produced due to spherical indenters near the specimen edge. Irrespective of the indentation distance from the edge, early material failure has been shown to be characterized by a sub-surface median crack directly under the contact point. However, higher material compliance in the near-edge region and the bending moment experienced by a growing crack have been suggested as sources of chip formation when the indentation distance from the specimen edge is small (less than 0.05 mm) [5]. In the current case, the entire specimen thickness makes a line contact with the cylindrical impactor head. Given the symmetric nature of the contact, it is reasonable to expect symmetric chipping about the specimen's mid-plane as in Fig. 5.10. Chai et al. [6] add to the above inferences by attributing chip initiation and the radial striations in the hackle region to stress enhancement in the specimen edge and multiple stress-wave reflections at the edge respectively.

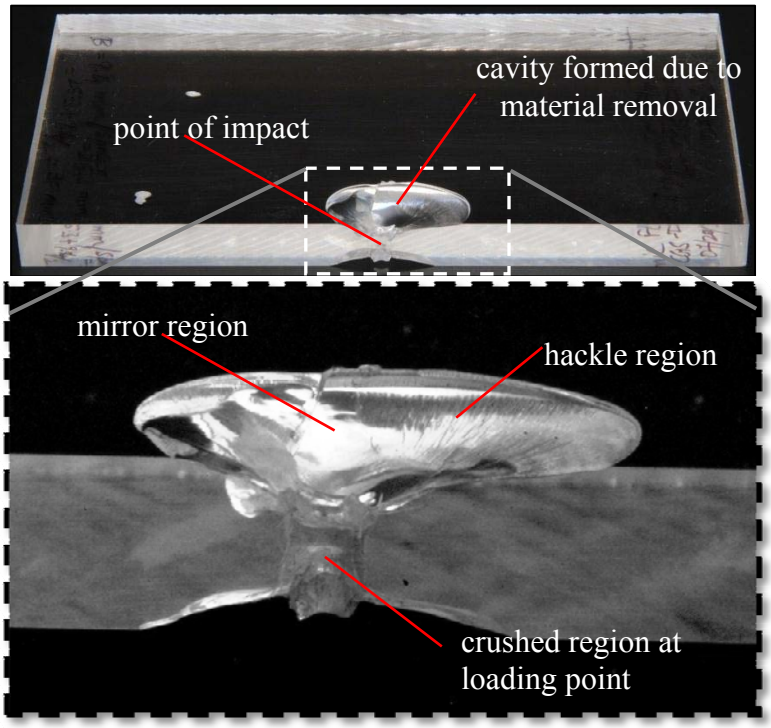

Figure 5.10: Failed PMMA specimen after experiencing a dynamic line-load on the edge (top). Close-up of the damaged/cracked region (bottom).

6

Crack-tip Deformation Measurement: Static Case

Failure characterization in structural components plays a vital role in material selection and engineering design. In particular, measurement of fracture parameters such as stress intensity factors is of importance due to the instantaneous nature of failure caused by sharp discontinuities / cracks. Accordingly, this chapter presents the feasibility of DGS for measuring crack-tip stress gradient fields under quasi-static loading. In this chapter, the experimental procedure, optical measurements and extraction of crack-tip stress intensity factors are described. The experimental results are compared with the ones from an analytical solution.

6.1 Experimental details

Using the DGS method, a quasi-static symmetric 3-point bend experiment on an edge cracked specimen (mode-I) was performed. A photograph of the experimental setup is shown in Fig. 6.1. A transparent PMMA specimen of dimensions 220 x 62.5 x 9.2 mm^3, with an initial crack of length 12 mm was used as the test specimen. An Instron 4465 universal testing machine was used to load the sample resting on two anvils (span 210 mm) in a displacement controlled mode (cross-head speed = 0.005 mm/sec). A target

plate painted with black and white speckle pattern was placed at a distance of $(\Delta =)29.9$ mm behind the mid-plane of the specimen. Multiple reference points were marked on the target to help relate the image dimensions to the actual specimen dimensions. A Nikon D100 digital SLR camera with a 28-300 mm focal length macro lens was placed in front of the specimen at approximately one meter distance. The camera also used an adjustable extension tube to achieve good focus of speckles on the target plane. Further, a relatively small aperture ($F^{\#} = 11$) was selected to achieve a good depth of field to resolve specimen features while maintaining the target plane focus. Before loading, a reference image was recorded using a camera resolution of 1504 × 1000 pixels (one pixel covered 43.6 μm on the target). Subsequently, speckle images were captured in the deformed state once every 5 seconds during loading using time-lapse photography. As the crack-tip vicinity suffered deformation, light rays passing through the specimen were deflected by the local non-uniform state of stress distorting the speckle images relative to the reference state. The images corresponding to the deformed state along with the one from the reference state were then used to extract the angular deflection fields (ϕ_x and ϕ_y) using 2D digital image correlation as described earlier. The images were segmented into 15×15 pixel non-overlapping sub-images during image correlation. This yielded an array of 99 x 65 data points to analyze.

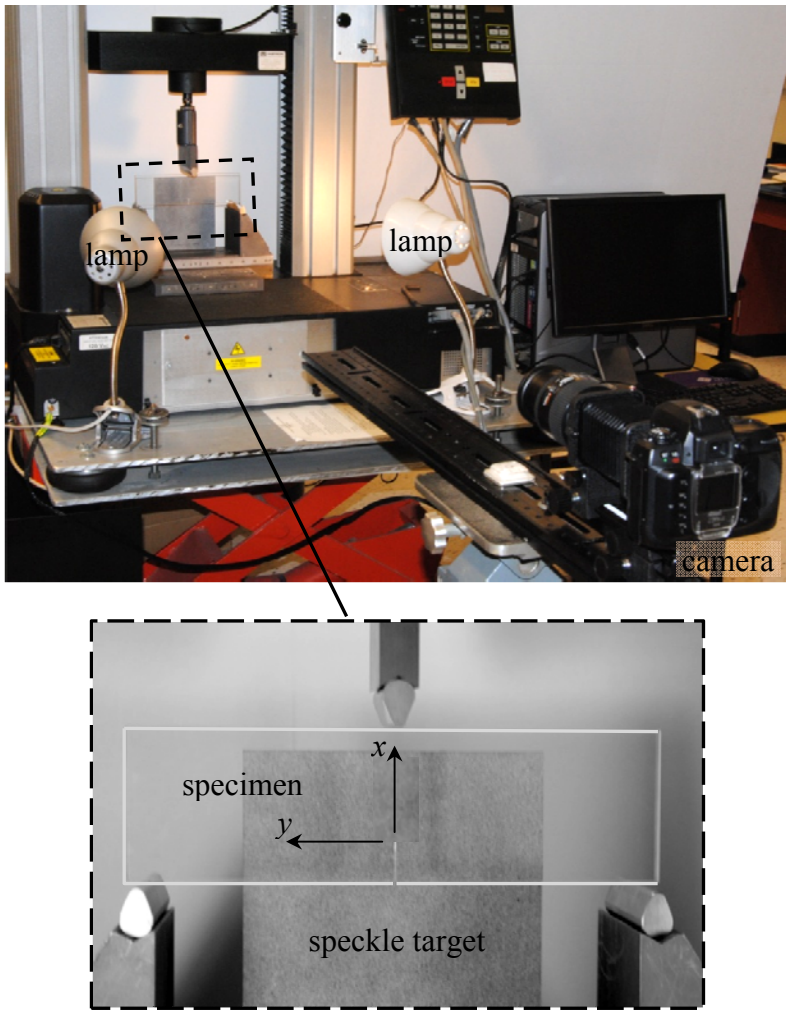

Figure 6.1: Experimental setup used to measure angular deflections of light rays caused by a mode-I crack in a planar transparent 3-point bend specimen subjected to quasi-static loading.

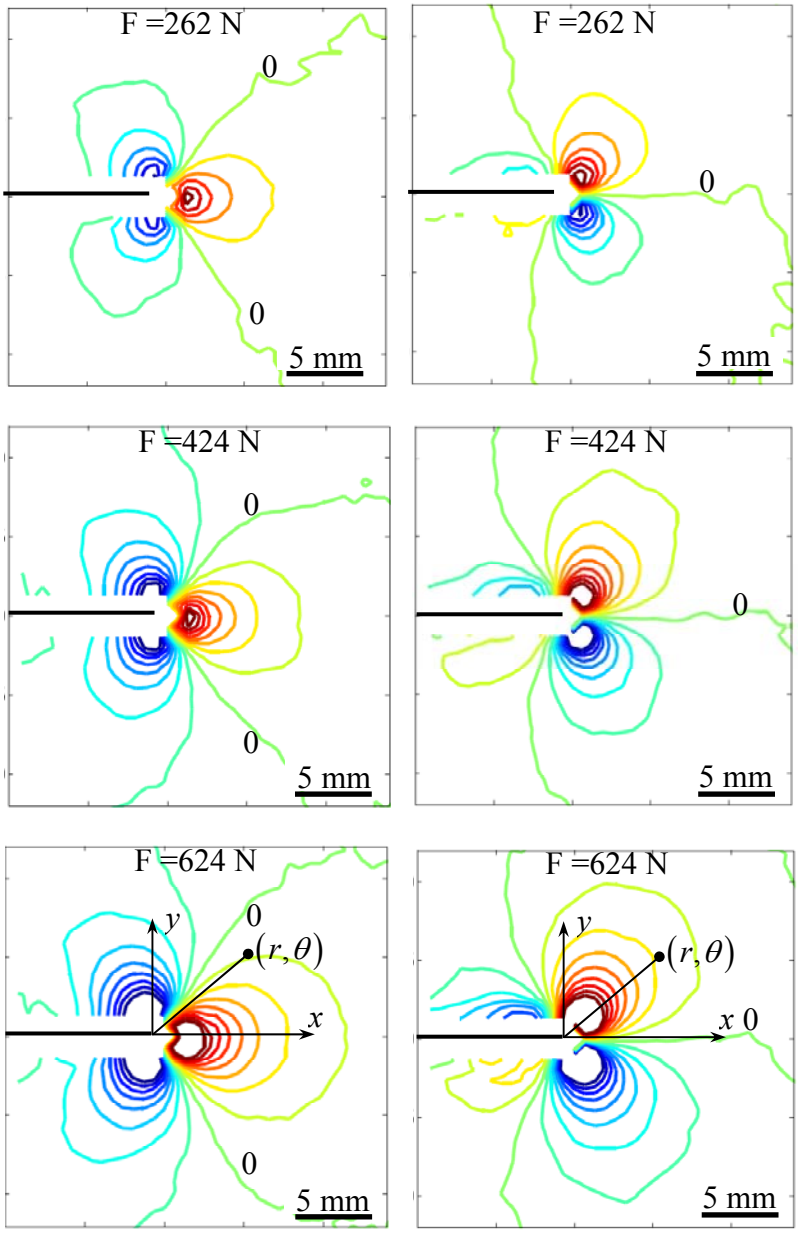

Figure 6.2: Experimental ϕ_x (column 1) and ϕ_y (column 2) contours near the crack-tip for different load levels. Contours are plotted every 25 x 10^{-5} radian.

Figure 6.2 shows the resulting contours of ϕ_x and ϕ_y for three representative load levels in a square region around the crack-tip. The assignment of contour levels requires

consideration of boundary conditions [47] of the problem on hand. For example, in the mode-I crack problem, boundary conditions such as symmetric ϕ_x and asymmetric ϕ_y about the *x*-axis, vanishing stress gradients far away from the crack-tip and stress free surfaces along the edges behind the crack are all considered while assigning the contour levels. It should be noted that the contour lines adjacent to the crack faces in Fig. 6.2 appear smeared due to unavoidable edge effects. Additionally, diffraction effects and residual stresses incurred during machining of the crack itself also contribute to the loss of information along a narrow band adjacent to the two crack faces.

6.2 Extraction of stress intensity factor (K_I)

From Williams' asymptotic stress field expansion for mode-I cracks, the expressions for angular deflections (or in-plane gradients of stresses) can be expressed as [28],

$$\begin{aligned}\phi_x &= C_\sigma B\frac{\partial\left(\sigma_{xx}+\sigma_{yy}\right)}{\partial(x)} = C_\sigma B\sum_{N=1}^{\infty}A_N\left(\frac{N}{2}-1\right)r^{\left(\frac{N}{2}-2\right)}\cos\left(\frac{N}{2}-2\right)\theta,\\ \phi_y &= C_\sigma B\frac{\partial\left(\sigma_{xx}+\sigma_{yy}\right)}{\partial(y)} = C_\sigma B\sum_{N=1}^{\infty}A_N\left(\frac{N}{2}-1\right)r^{\left(\frac{N}{2}-2\right)}\sin\left(\frac{N}{2}-2\right)\theta,\end{aligned} \tag{6.1}$$

where $C_\sigma \approx -0.9\times10^{-10}\ \mathrm{m^2/N}$ is the elasto-optic constant of PMMA [48], B = 9.2 mm is the thickness of the specimen, (r,θ) are the crack-tip polar coordinates and $A_1 = K_I\sqrt{\frac{2}{\pi}}$ with K_I being the mode-I stress intensity factor. In the above equations, if *K*–dominance is assumed (or, terms with $N \geq 3$ in Eq. 6.1 are neglected), we get

$$\phi_x = C_\sigma B\left[\left(-\frac{A_1}{2}\right)r^{\left(-\frac{3}{2}\right)}\cos\left(-\frac{3\theta}{2}\right)\right],$$
$$\phi_y = C_\sigma B\left[\left(-\frac{A_1}{2}\right)r^{\left(-\frac{3}{2}\right)}\sin\left(-\frac{3\theta}{2}\right)\right]. \quad (6.2)$$

The above angular deflection field equations were used to obtain the mode-I stress intensity factor (K_I) using overdeterministic regression analysis of measured data. Discrete angular deflection values around the crack-tip in the region $\left(0.3 \le r/B \le 1.6\right)$ and an angular extent (-150˚ $\le \theta \le$ +150˚) were used in the regression analysis. This ensured that data close to the crack-tip where triaxial effects are dominant are excluded from the regression analysis. The upper bound ($r/B \sim 1.6$) of the radial extent makes sure that only those data points rich in the K-dominant mode-I crack-tip field are included in the analysis. Further, these help deal with any uncertainty with the crack-tip location due to edge effects introduced by the image correlation operation. The results thus obtained are plotted in Fig. 6.3 for different load levels. The error bars shown in the graph correspond to stress intensity factors obtained by using different subsets of $\left(0.3 \le r/B \le 1.6\right)$ range.

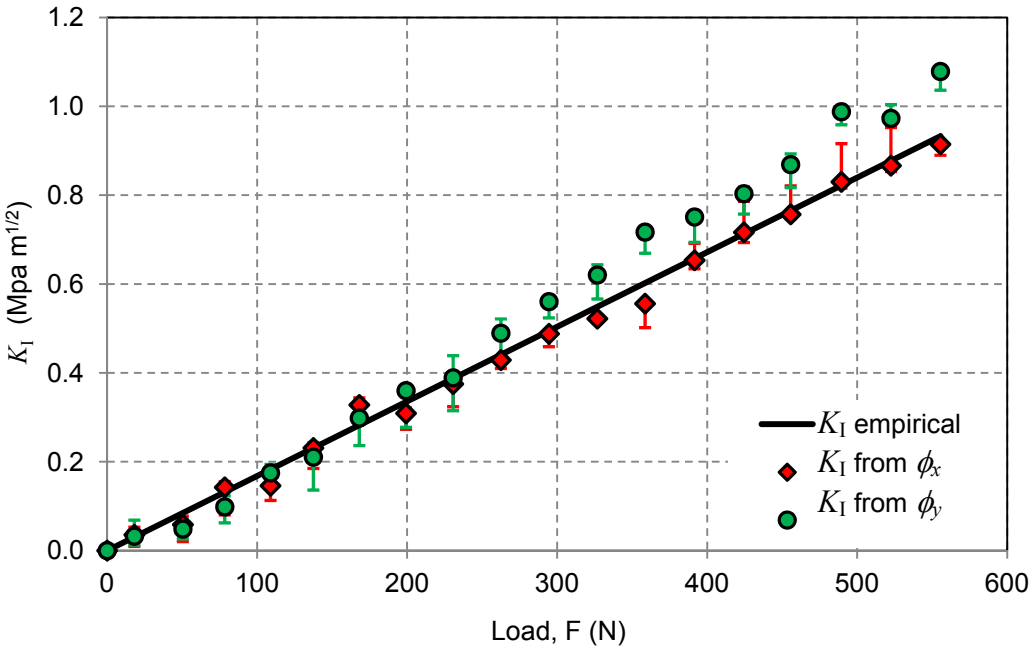

Figure 6.3: Experimental vs. empirical stress intensity factors for a static 3-point-bend crack problem for various load levels.

6.3 Comparison of measurements and closed-form solutions

As a means for comparison, the crack-tip stress intensity factors for different load levels calculated using a result based on boundary collocation method [49],

$$K_I = \frac{F \cdot S}{B \cdot W^{\frac{3}{2}}} \cdot \frac{3\left(\frac{a}{W}\right)^{\frac{1}{2}}\left[1.99 - \frac{a}{W}\left(1-\frac{a}{W}\right)\left\{2.15 - 3.93\left(\frac{a}{W}\right) + 2.7\left(\frac{a}{W}\right)^2\right\}\right]}{2\left(1+2\frac{a}{W}\right)\left(1-\frac{a}{W}\right)^{\frac{3}{2}}}, \qquad (6.3)$$

are also presented in Fig. 6.3. In the above equation, F is the applied load, S is the distance between the supports, a is the initial crack length, and W is the specimen width. The stress intensity factors thus obtained were in turn used in Eqs. (6.2) to obtain the analytical ϕ_x and ϕ_y contours. Figure 6.4 shows a comparison of the experimental and

analytical angular deflection contours for a representative load level of F = 624 N. Evidently the agreement between the analytical and experimental contour lines is rather good, further validating the feasibility of the method.

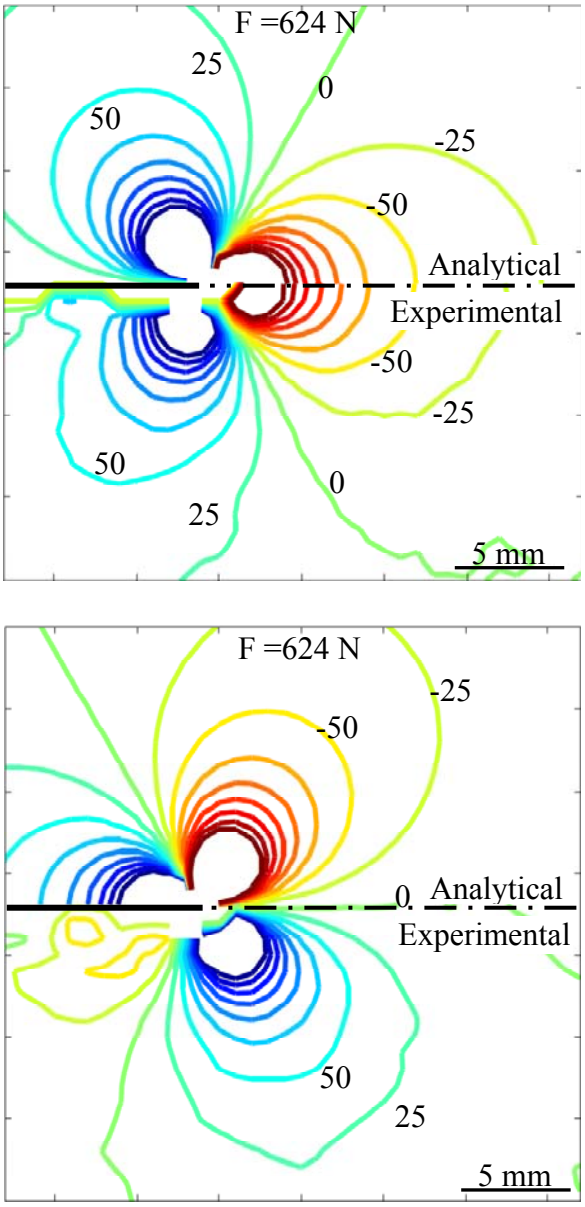

Figure 6.4: Comparison of experimental and analytical ϕ_x (top) and ϕ_y (bottom) contours near the mode-I crack-tip corresponding to a load of 624 N.
Contours are plotted every 25 x 10^{-5} radian.

7

Crack-tip Deformation Measurement: Dynamic Case

This chapter describes a dynamic mode-I fracture experiment using the DGS method. An ultra high-speed digital camera is used to record time resolved deformations in the specimen. Similar to the quasi-static crack counterparts, stress intensity factor history measurements are compared with an independent calculation by performing an elasto-dynamic finite element computation up to crack initiation.

7.1 Experimental details

The dynamic fracture experiments were performed on edge cracked PMMA samples using a drop-tower facility and ultra high-speed photography. A schematic of the experimental setup used is shown in Fig. 7.1. The specimen was a $130\times51\times8.9$ mm^3 transparent PMMA sheet with an initial crack of length 12 mm. The specimen was placed on two instrumented anvils of the drop-tower, symmetrically about the crack line and the plunger (hemispherical impact head), as shown in Fig. 7.2. The speckle target was placed at a distance of $\Delta = 29.8$ mm from the mid-plane of the specimen. A Cordin model 550

ultra high-speed digital camera equipped with 32 CCD sensors and a five-facet rotating mirror, two high-energy flash lamps and a delay generator was used to record the real time speckle images during stress wave loading. A computer connected to the camera was used to control the experimental parameters such as trigger delay, flash duration, framing rate and image storage.

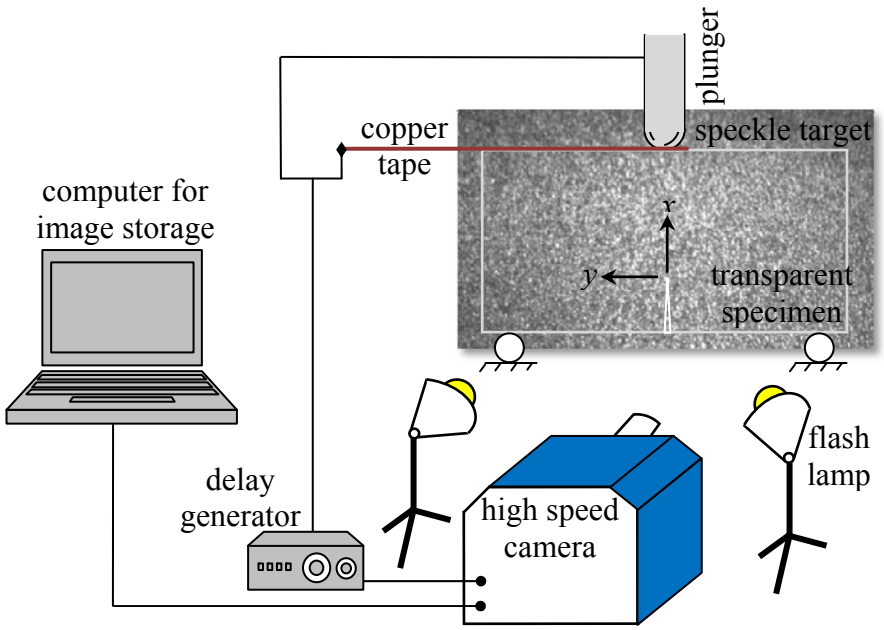

Figure 7.1: Schematic of the experimental setup used in the dynamic mode-I fracture study.

Prior to impact loading, a set of 32 images, one for each of the 32 CCD sensors of the high-speed camera, was captured at 200,000 frames per second. Then, the plunger, initially held at a predetermined height was launched to impact the mid-plane of the specimen at ~4.5 m/s. The propagating stress waves upon reflection from the free edges behind the crack load and initiate the crack-tip. When the plunger came in contact with a copper tape adhered to the top edge of the specimen, an external circuit was closed

triggering the flash lamps and the high-speed camera previously brought to speed to record at 200,000 frames per second. A second set of 32 images were recorded during the impact/fracture event. The latter set of images correspond to distorted speckle patterns as the deformation in the specimen cause the light rays passing through it to deflect according to the instantaneous local stress field.

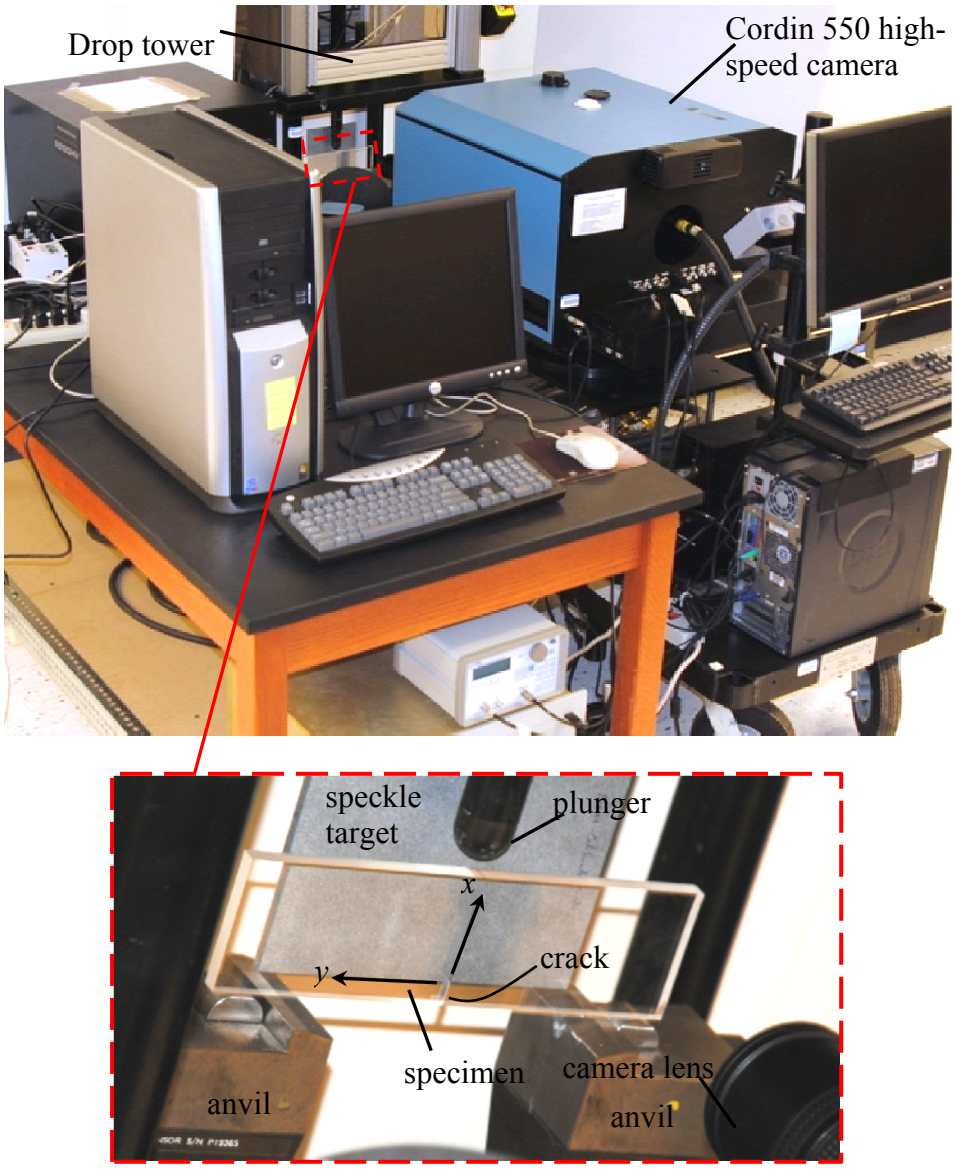

Figure 7.2: Experimental setup used in the dynamic mode-I fracture study.

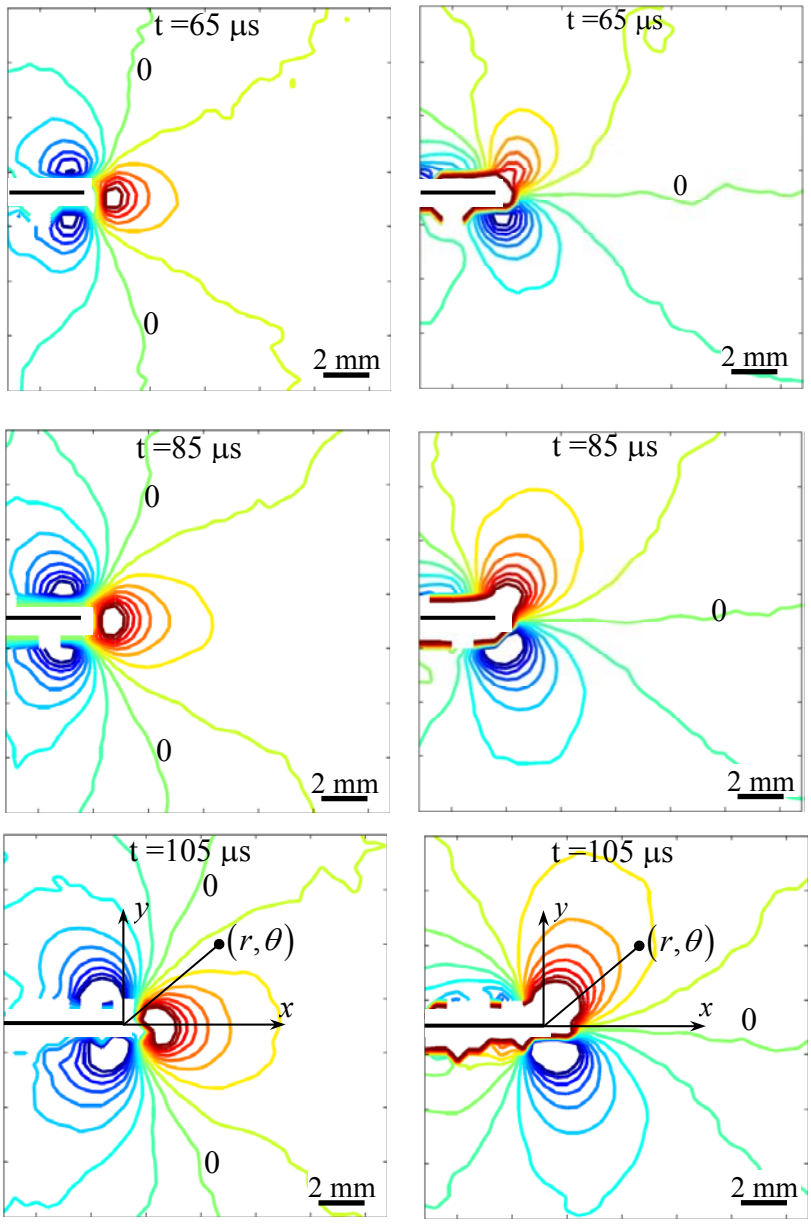

Figure 7.3: Experimental ϕ_x (column 1) and ϕ_y (column 2) contours near the crack-tip for different load levels. Contours are plotted every 50 x 10^{-5} radian.

The 32 deformed-undeformed image pairs corresponding to the 32 CCD sensors were then correlated using 2D DIC method to obtain the in-plane displacement fields, δ_x and δ_y, in the region of interest near the crack-tip. A facet/sub-image size of 15 x 15

pixels (1 pixel = 32 μm on the target plane) without any overlap was used in the image analysis for extracting displacement components along and normal to the crack direction. The displacement fields were then used to compute the angular deflections fields (ϕ_x and ϕ_y) as described earlier. A few representative results are shown in Fig. 7.3. In these figures, the first two rows correspond to pre crack initiation regime, and the third to that of post crack initiation. It is obvious from the contour plots that the crack has propagated along its initial orientation of the crack, without any kink. The contour interval in Fig. 7.3 was chosen to be 50×10^{-5} radians which is an order of magnitude higher than the angular deflections that can be measured for commercial PMMA sheet of similar thickness [47, 50]. As in case of the static fracture problem (Chapter 6), boundary conditions such as symmetric stress gradients about the *x*-axis and asymmetric stress gradients in the *y*-direction relative to the *x*-axis, vanishing stress gradients away from the crack-tip and stress free edges behind the crack were all utilized to quantify the contour levels. Again, as noted earlier, image correlation operations introduce edge effects. This coupled with residual stresses (along the initial notch) and diffraction effects make contours not discernible in a narrow band along the two crack faces.

7.2 Extraction of stress intensity factor (K_I)

The expressions for angular deflection fields corresponding to a steadily growing crack are given by [51],

$$\phi_x(t) = f(v;C_L,C_s)C_\sigma B\left[\left(-\frac{A_1(t)}{2}\right)r^{\left(-\frac{3}{2}\right)}\cos\left(-\frac{3\theta}{2}\right)\right] + HoT,$$
$$\phi_y(t) = g(v;C_L,C_s)C_\sigma B\left[\left(-\frac{A_1(t)}{2}\right)r^{\left(-\frac{3}{2}\right)}\sin\left(-\frac{3\theta}{2}\right)\right] + HoT, \quad (7.1)$$

where, f and g are functions of crack velocity, v, dilatational and shear wave speeds, C_L and C_S, respectively and $A_1(t) = K_I(t)\sqrt{\frac{2}{\pi}}$ with K_I being the mode-I stress intensity factor. In the above, *HoT* represents higher order terms of the asymptotic expansion for the angular deflection fields. Further, for plane stress conditions,

$$f(v;C_L,C_S) = \frac{\left(1+\alpha_S^2\right)\left(\alpha_L^2-\alpha_S^2\right)}{4\alpha_S\alpha_L - \left(1+\alpha_S^2\right)^2} \quad (7.2)$$

where, $\alpha_{L:S} = \sqrt{1-\frac{v^2}{C_{L:S}^2}}$. The instantaneous crack velocity corresponding to each deformed image was calculated by measuring the change in the crack length between successive images and dividing by the temporal separation between them (Fig. 7.4). The post initiation crack velocities were in the 190 – 300 m/s range. The dilatational and shear wave speeds were measured using ultrasonic pulse-echo measurements [45]. The angular deflection fields were then used with Eqs. (7.1) to extract the dynamic mode-I stress intensity factor (K_I) history by performing an overdeterministic least-squares analysis of the measured data. As in the quasi-static case, data in the $\left(0.3 \le r/B \le 1.6\right)$ range were used in the regression analysis. For the dynamic analysis, $C_\sigma \approx -1.08\times10^{-10}$ m^2/N was used in Eqs. (7.1) based on the dynamic elasto-optic constant of PMMA reported in Ref. [52].

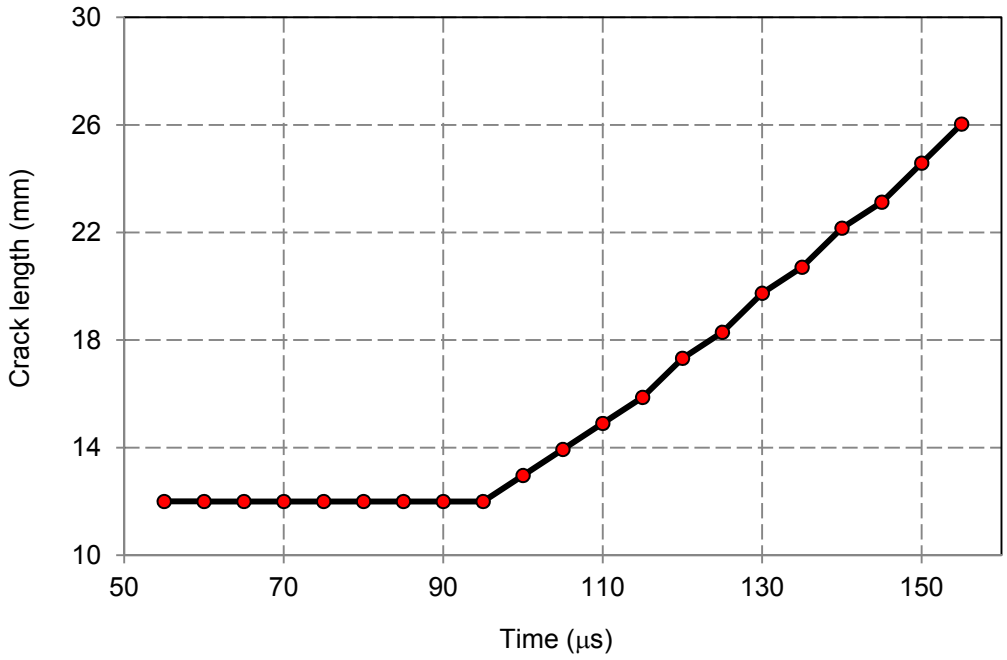

Figure 7.4: Crack growth history in PMMA

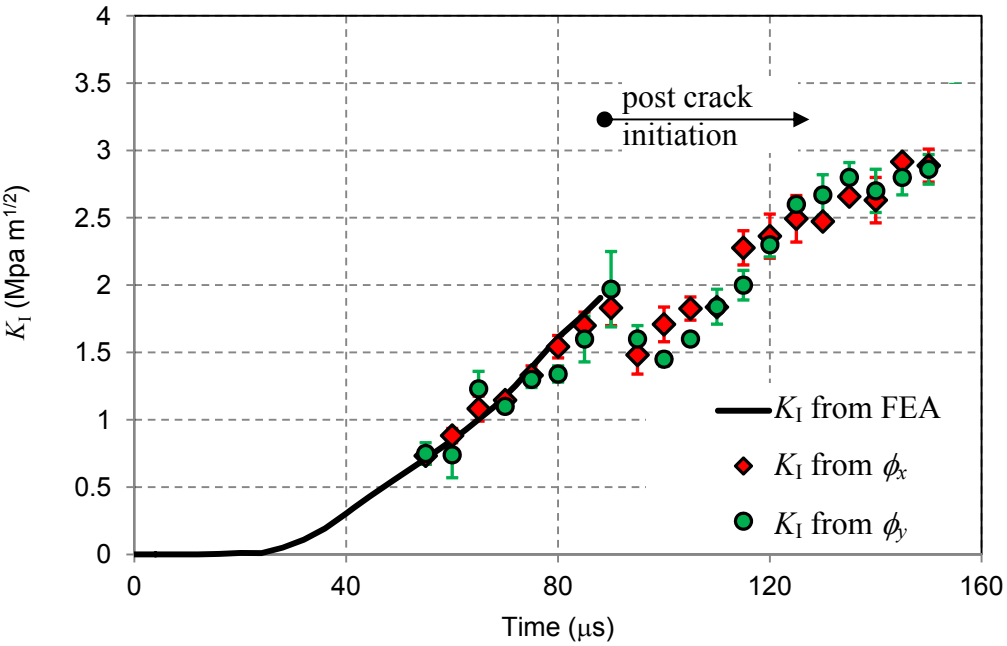

Figure 7.5: Dynamic mode-I stress intensity factor histories from overdeterministic least-squares analysis of angular deflection data. Solid line is obtained from finite element analysis.

Figure 7.5 shows the crack-tip K_I histories computed using the measured ϕ_x and ϕ_y fields. The error bars in Fig. 7.5 correspond to stress intensity factors obtained by using different subsets of the radial extent $\left(0.3 \le r/B \le 1.6\right)$ of optical data used in the analysis. The plot shows a monotonic increase in K_I prior to crack initiation. The crack initiation (~1.8 MPa√m) is signified by a noticeable dip in the history at approximately 90 μs after impact. Following crack initiation, again a monotonic increase in K_I seems to ensue over the next 50 μs time window. Also included in Fig. 7.5 is the numerically determined K_I history up to crack initiation, represented as a solid line, from a complementary finite element analysis.

The finite element simulation was performed using ABAQUS^{TM}/Explicit software package, and used a half symmetric model of the experiment. The model was discretized with 29979, four node bi-linear plane stress quadrilateral elements with reduced integration and hourglass control. The time steps during the analysis were allowed to be automatically controlled by the explicit integration scheme. The dynamic elastic modulus and Poisson's ratio of PMMA used in the simulation were obtained from ultrasonic pulse-echo measurement of longitudinal and shear wave speeds [45] and mass density of PMMA. The measured plunger velocity of 4.5 m/s was used as an input in the simulation. The boundary conditions shown in Fig. 7.6 correspond to a half symmetric model of the dynamic crack experiment.

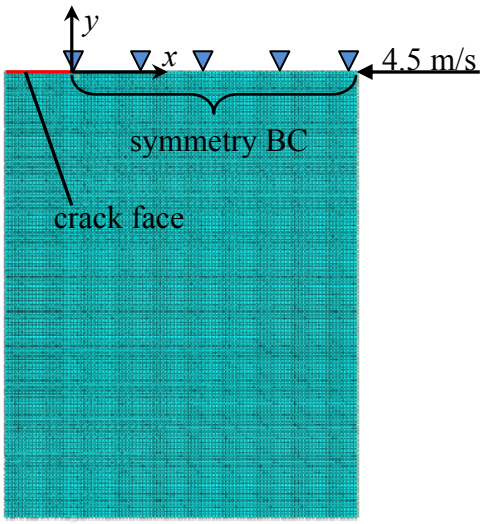

Figure 7.6: One-half finite element model used for performing elasto-dynamic fracture analysis.

The crack opening displacements (COD) along the upper crack face were extracted every 5 μs after imposing the constant velocity input and the mode-I stress intensity factor (K_I) computed using [52]

$$K_I(t) = \frac{E\sqrt{2\pi}}{4\sqrt{r}} u_2(t); \quad (r, \theta = \pi) \tag{7.3}$$

where E = 5.8 GPa is the dynamic elastic modulus [47] of PMMA and u_2 is half COD of the crack flanks. These simulations were limited to the case of a dynamically loaded stationary crack and hence the comparison of K_I histories from measurements and simulations are valid up to crack initiation. Accordingly, the numerical data from simulations are superposed on the experimentally extracted K_I values up to the observed crack initiation time. A good agreement between the two is evident, supporting the feasibility of DGS method for studying dynamic fracture problems.

8

Dynamic Punch Experiment

In this chapter, the results from a DGS experiment in which a plate subjected to dynamic load by a square punch are presented. A long-bar setup similar to the one used in the dynamic line-load experiment (Chapter 5) has been used. The elasto-optic changes in the transiently deforming PMMA sheets are captured using high-speed photography as in the cases of dynamic line-load (Chapter 5) and dynamic fracture (Chapter 7) experiments. The angular deflection fields in the specimen, near the punch-tip are measured for different time instants. Further, by using the punch-crack analogy, the crack-tip angular deflection field equations are used to obtain the stress intensity factor (K_P) histories at the punch corner.

8.1 Punch-tip – crack-tip analogy

Material failure due to high strain-rate loading is often initiated by shear localization [53]. Such a scenario can be realized experimentally when a plate specimen is impacted on its side by a square punch. This results in shear bands originating at the punch-tip. One way of characterizing dynamic failure in such a scenario is by evaluating dynamic stress intensity factor history at the punch-tips [54]. This is done by using the analogy between the problem of a square punch loading a semi-infinite plate and the problem of two semi-infinite edge cracks being loaded in compression [53, 54], as shown in Fig. 8.1.

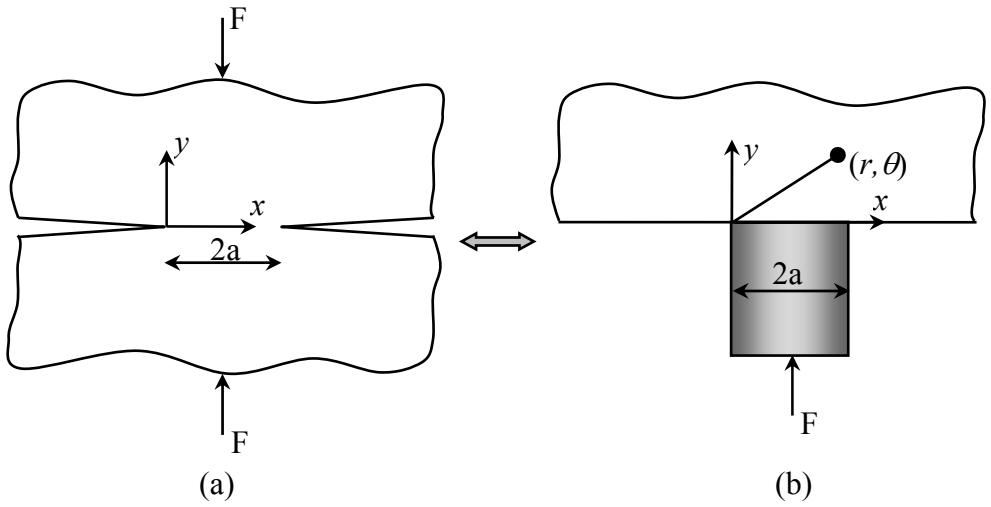

Figure 8.1: Analogy between (a) compressively loaded semi-infinite double crack and (b) punch loaded semi-infinite plate.

8.2 Experimental details

The schematic of the experimental setup used for studying the dynamically loaded planar sheet by a square punch using DGS is shown in Fig. 8.2. The loading device consisted of an Al 7075-T6 long-bar (2 m long, 25.4 mm diameter), a gas-gun and the high-speed digital image acquisition system used in the dynamic crack experiment. The long-bar was aligned with the gas-gun barrel containing a 305 mm long, 25.4 mm diameter cylindrical striker also made of Al 7075-T6. Its leading head was machined flat as shown in the inset of Fig. 8.3 so that it makes a square contact with the specimen's side. The height of the punch was 23.1 mm. The specimen, a 160 × 90 × 5.7 mm^3 clear PMMA plate, was placed on an adjustable platform and its long side was registered against the head of the long-bar as shown in Fig. 8.3.

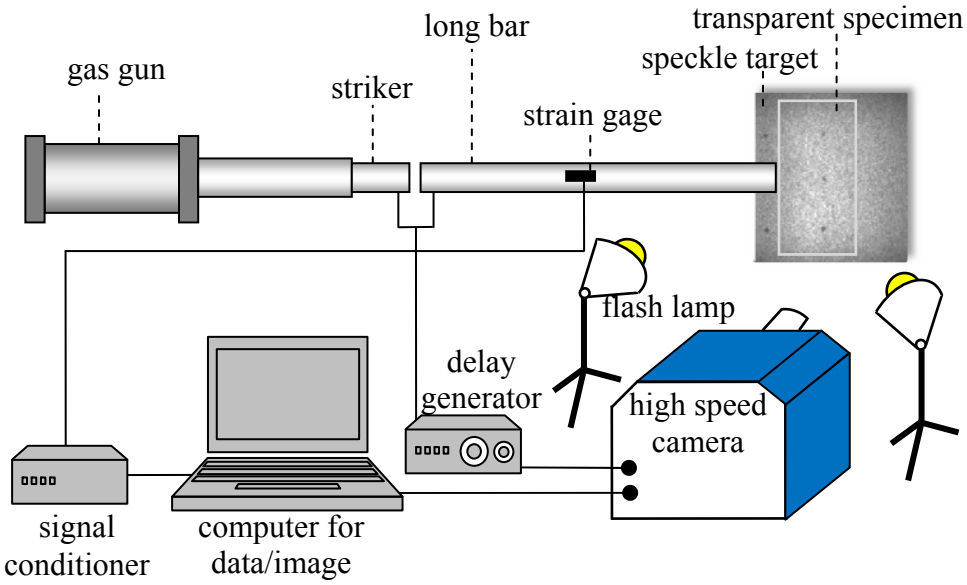

Figure 8.2: Schematic of the dynamic punch experimental setup.

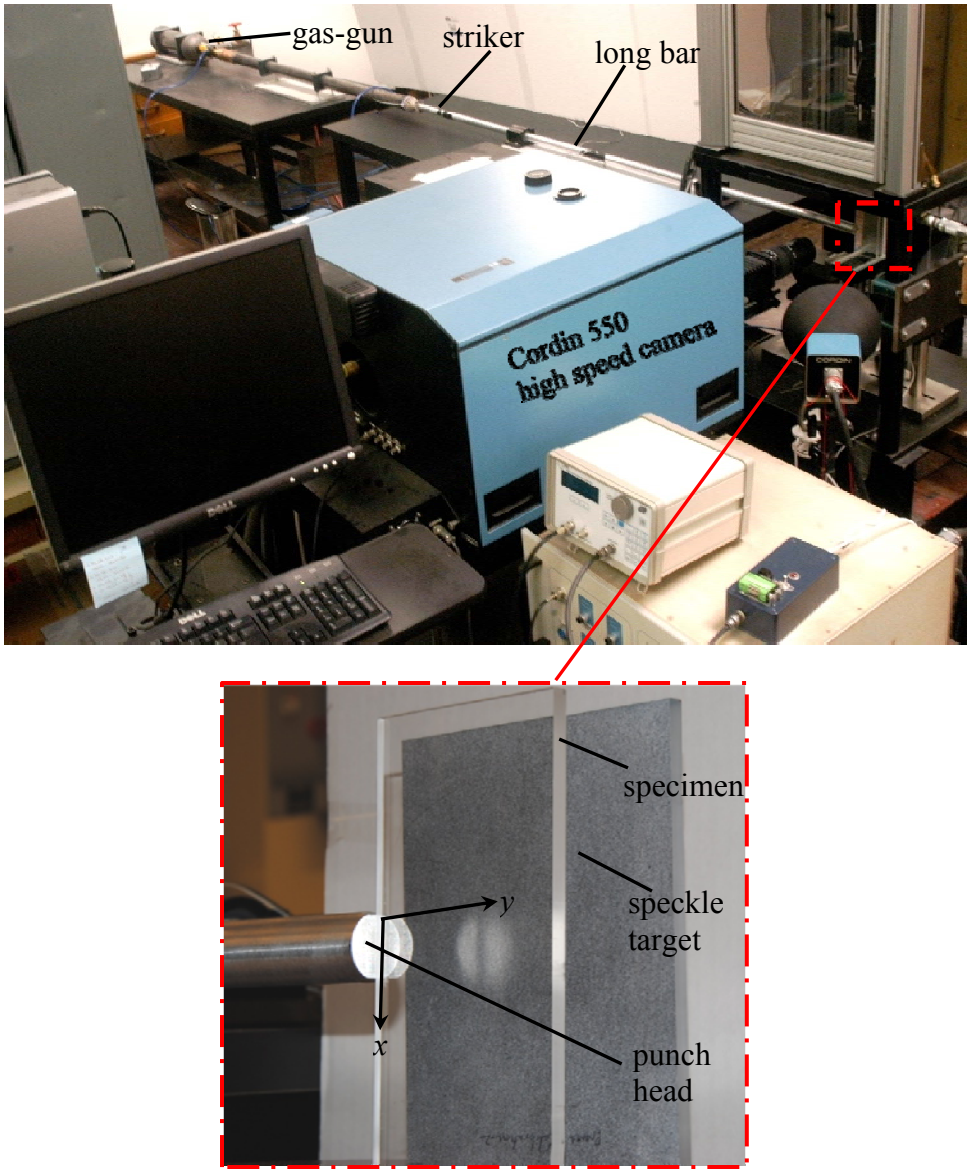

Figure 8.3: Dynamic punch experimental setup (top), and close up of the punch-specimen edge (bottom).

The loading was initiated by suddenly releasing compressed air stored in the gas-gun cylinder using a solenoid valve to propel the striker placed inside the barrel. The accelerating striker impacted the long-bar and initiated a compressive stress wave that traveled the length of the bar before imparting a transient punch-load to the side (edge) of the specimen. An electrical circuit, closed when the striker contacted the long-bar, was used to trigger a delay generator which in turn activated the camera with a user-specified delay. A strain gage (CEA-13-062UW-350 from Vishay Micro-measurements) affixed to the long-bar, and connected to a LeCroy digital oscilloscope via an Ectron signal conditioner was used to measure the strain history $\varepsilon_I(t)$ in the long-bar during loading [44]. The distance between the specimen and the camera lens was L ~1000 mm and between the specimen mid-plane and the target plane was Δ = 28.2 mm. Using the high-speed camera, a set of 32 reference (undeformed) images, one for each sensor, were first captured under no-load condition at 200,000 frames per second. Next, the specimen was subjected to a dynamic line-load using the long-bar setup. During loading, a set of 32 consecutive images of the deforming specimen were captured at the same framing rate. The deformed-undeformed image pairs for each of the 32 CCD sensors were then correlated to obtain the in-plane displacement fields, δ_x and δ_y. A facet/sub-image size of 15 x 15 pixels (1 pixel = 37 μm on the target plane) without any overlap was used in the image analysis for extracting displacement components. The displacement fields were then used to compute the angular deflection fields (ϕ_x and ϕ_y), and are shown in Fig. 8.4.

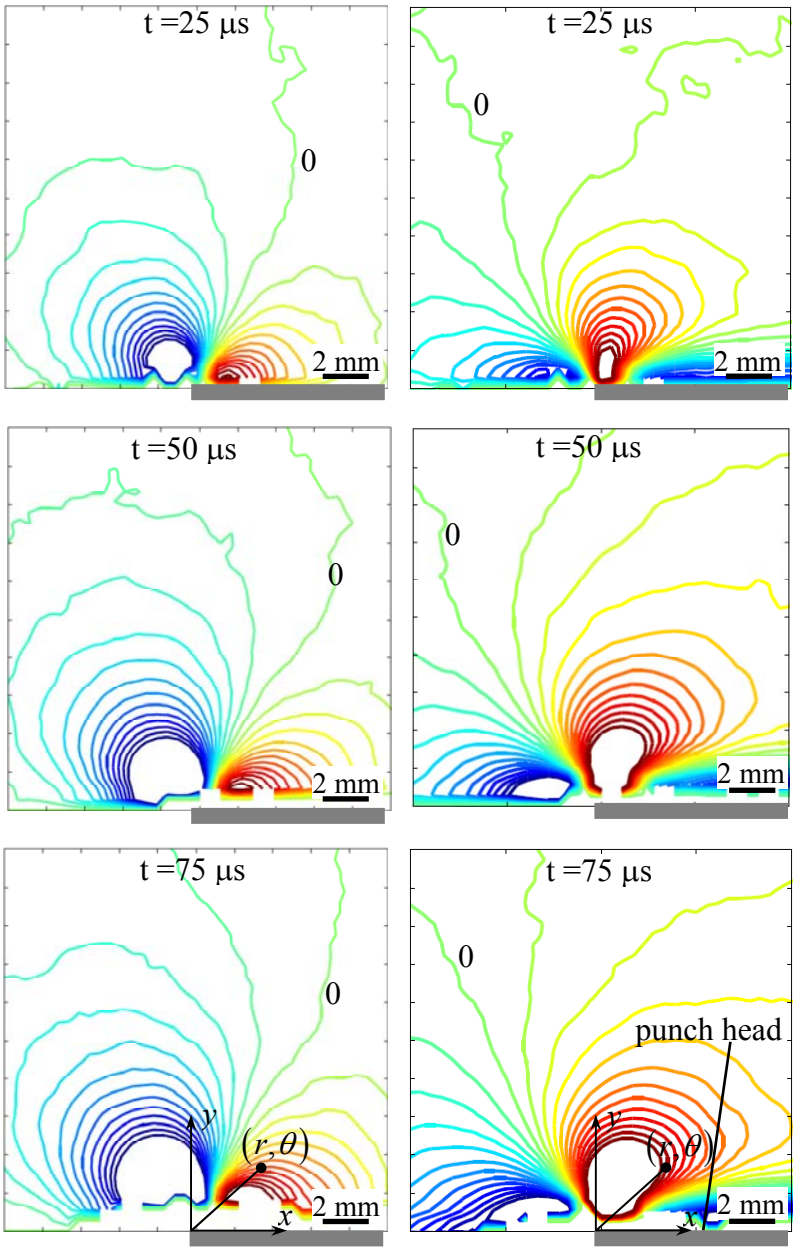

Figure 8.4: Experimental ϕ_x (column 1) and ϕ_y (column 2) contours near the punch-tip for different time instants. Contours are plotted every 50 x 10^{-5} radian.

8.3 Extraction of punch-tip stress intensity factor

From the ϕ_x contours in Fig. 8.4, it can be seen that the contours above the x-axis resemble the ϕ_x contours in Fig. 7.3 corresponding to a crack-tip ϕ_x field. However, the ϕ_y counterparts from the punch experiments differ from that of the crack experiments near the x-axis. This difference is due to the compressive stress waves caused by the punch load at and near the contact area. Nevertheless, the ϕ_x and ϕ_y contours obtained from the punch and the crack experiments are qualitatively similar in the $70^\circ \leq \theta \leq 180^\circ$ range, which serves to further support the punch-tip – crack-tip analogy as discussed earlier. Therefore, it is reasonable to use Eqs (7.1) to extract the punch-tip dynamic stress intensity factor, K_P after replacing K_I with K_P as,

$$\begin{aligned} \phi_x &= C_\sigma B\left[K_P(t)\sqrt{\frac{2}{\pi}}\left(-\frac{1}{2}\right)r^{\left(-\frac{3}{2}\right)}\cos\left(-\frac{3\theta}{2}\right)\right], \\ \phi_y &= C_\sigma B\left[K_P(t)\sqrt{\frac{2}{\pi}}\left(-\frac{1}{2}\right)r^{\left(-\frac{3}{2}\right)}\sin\left(-\frac{3\theta}{2}\right)\right], \end{aligned} \tag{8.1}$$

in the mode-I crack-tip equations. In the above equation, B = 5.7 mm is the thickness of the sample. Using the above equations and the measured angular deflection field data in the ($0.3 \leq r/B \leq 1.6$, $70^\circ \leq \theta \leq 160^\circ$) range, the dynamic stress intensity factor (K_P) history at the punch corner was computed by performing an overdeterministic least-squares analysis of measured data.

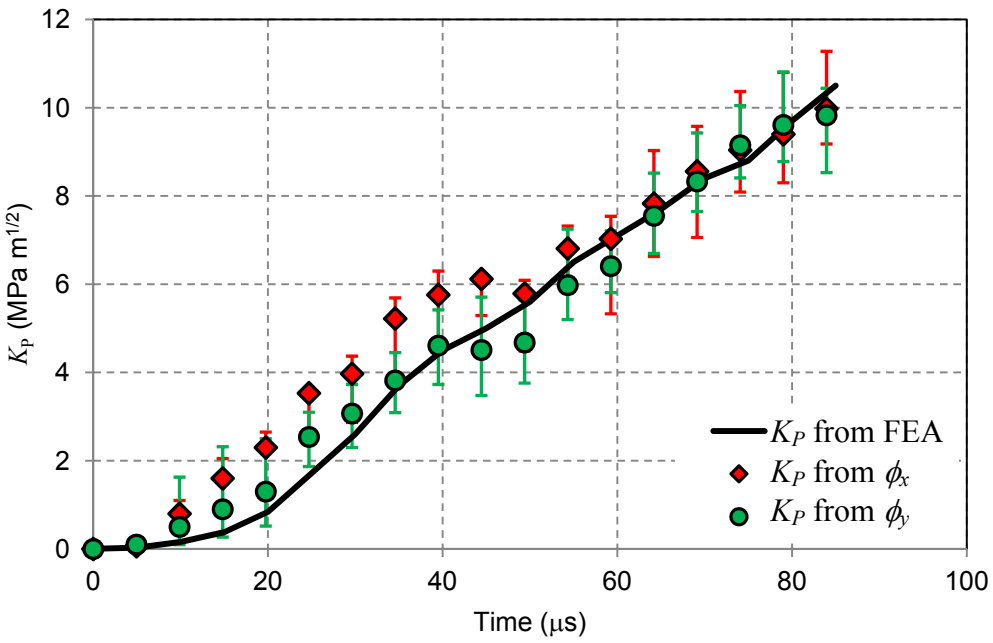

Figure 8.5: Experimental vs. numerically obtained stress intensity factors for a dynamic punch problem.

The results are shown in Fig. 8.5. The error bars for symbols in the graph correspond to K_P values obtained using different subsets of the ($0.3 \leq r/B \leq 1.6$, $70^\circ \leq \theta \leq 160^\circ$) range. The rate of increase in K_P is initially shallow, in agreement with the slope of the loading curve (see graph in Fig. 8.6), after which it monotonically increases. The K_P histories from both the angular deflection fields follow a similar trend. When compared to the dynamic crack-tip stress intensity factors (Fig. 7.5), the dynamic punch-tip stress intensity factors are substantially higher. For example, at 65 μs after the first non-zero stress intensity factor, the punch-tip counterpart registers a value nearly four times the magnitude of the crack-tip K_I. This is expected as the plate experiences compressive stress waves, unlike the dominant tensile stresses at the crack-tip.

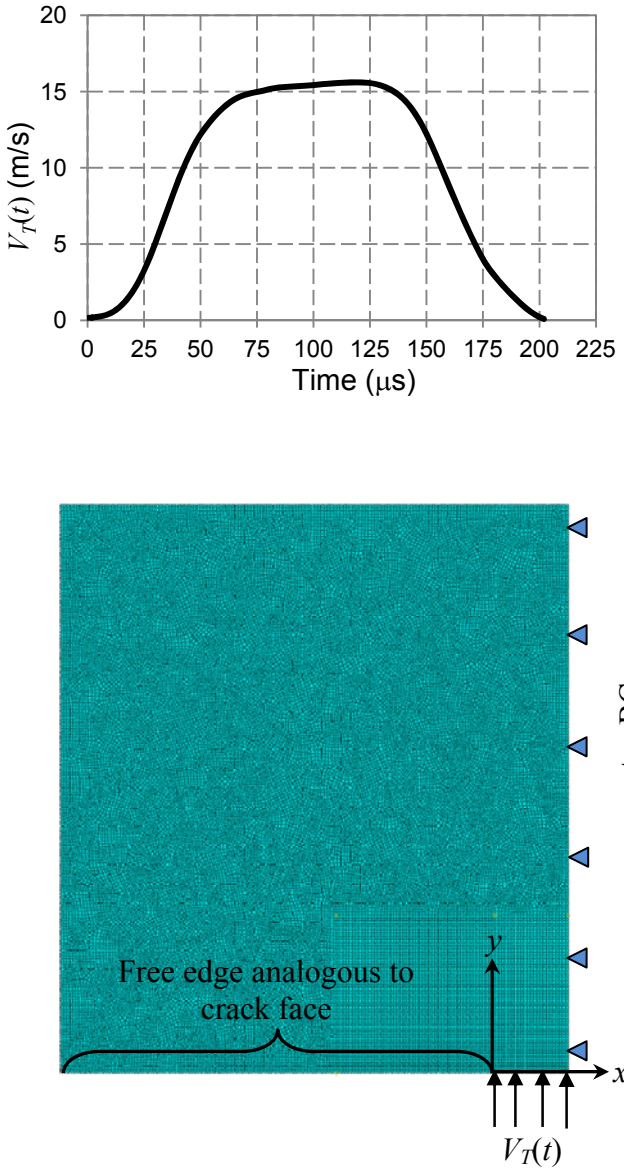

Figure 8.6: Transmitted particle velocity input obtained from strain gage measurements in the long bar (top). Finite element model showing load and boundary conditions used to simulate the crack-analogous punch problem (bottom).

The experiments were again numerically simulated using transient elasto-dynamic finite element analysis of the problem to provide a complementary set of results to the experimental measurements. Figure 8.5 also shows the numerically obtained K_P history. The numerical simulation was performed using ABAQUS/Explicit. The discretized

model along with the loading and boundary conditions used are shown in Fig. 8.6. It consisted of 33,574 four-node quadrilateral elements with the smallest element size ~ 0.5 mm. The time steps were allowed to be automatically chosen by the explicit integration scheme.

The particle velocity ($V_T(t)$) transmitted from the long-bar into the PMMA specimen was used as the input. The V_T history is shown in Fig. 8.6 was calculated using Eq. (5.1). The measured material properties of the long-bar and PMMA are shown in Table 5.1. Analogous to the crack problem, displacements (u_2) in the loading direction along the free edge of the impacted side of the PMMA sheet were extracted at 5 μs intervals. These displacements were then used to extract the punch-corner stress intensity factor (K_P) using [52]

$$K_P(t) = \frac{E\sqrt{2\pi}}{4\sqrt{r}} u_2(t); \quad (r, \theta = \pi). \tag{8.2}$$

The numerically obtained K_P history is plotted as a solid line in Fig. 8.5, which reveals a good agreement with the experimentally obtained values. This further substantiates the use of the punch-tip – crack-tip analogy.

9

Measurement of Surface Slopes: Feasibility of Reflection Mode DGS

Measurement of surface characteristics such as deflection, slope and curvature of thin plates are of importance in many engineering fields including aerospace and electronic industries. This is partly because bending stresses in plates can be quantified from curvatures which in turn are the first and second derivatives of slopes and deflections, respectively. However, since numerically or graphically differentiated quantities are prone to errors, the use of deflections to obtain stresses by performing two successive differentiations is not desirable if stresses are the primary quantities of interest. In such cases, direct measurements of surface slopes are preferred. Kao and Chiang's [55] work provides a comprehensive description of various moiré methods that can be used for contouring surface slopes and curvatures. The application of reflection moiré to dynamic vibration of plates has been investigated by Ritter [56]. These conventional techniques require grid patterns, and in some cases have restrictions such as monochromatic light [55]. These aspects motivate to reconfigure the DGS method to measure slopes of reflective surfaces. If successful, it could be a preferred method over the current techniques for surface slope measurements, as DGS has advantages such as,

relatively simple experimental setup, inexpensive optical components and digital measurements. The prevalence of DIC as a popular optical metrology tool, its ability to measure orthogonal displacement components simultaneously, and the availability of several commercial image analysis software tools to measure displacements as well as their derivatives all make reflection mode DGS for slope and curvature measurement attractive.

In the previous chapters, it was shown that DGS can measure angular deflections of light rays passing through a deformed planar transparent object. There, the deflection of light rays is caused by a combination of thickness as well as refractive index changes in the specimen. In the reflection mode, the light ray deflection upon reflection from a non-planar reflective surface due to non-uniform deformations is due to out-of-plane displacements only. A light ray that is normally incident on a specularly reflective surface will result in a reflected ray that is collinear with the incident ray. However, when the reflective specimen is subjected to out-of-plane displacements, the reflected ray corresponding to the initially normal incident ray will make an angle θ_r with the local normal to the deformed specimen surface. This angular deflection can be quantified using DGS, and thus surface slopes measured. Furthermore, it is also possible to obtain curvatures by differentiating the surface slopes once. The current chapter details the principle of measuring surface slopes of reflective objects, and also presents an experiment where surface slopes of a thin silicon wafer are measured and verified using closed form solutions.

9.1 Experimental details

The schematic of the setup to measure surface slopes of reflective planar specimens using the DGS method is shown in Fig. 9.1(a). It consists of an imaging device (Nikon D3100 digital SLR camera), a beam splitter and a planar speckle target. The camera was fitted with an extension tube and a 70-300 mm lens. The beam splitter is placed in between the specimen and the target, and is oriented at 45 degrees to the optical axis of the camera. The camera is now focused on the target plane via the reflective surface of the specimen and through the beam splitter.

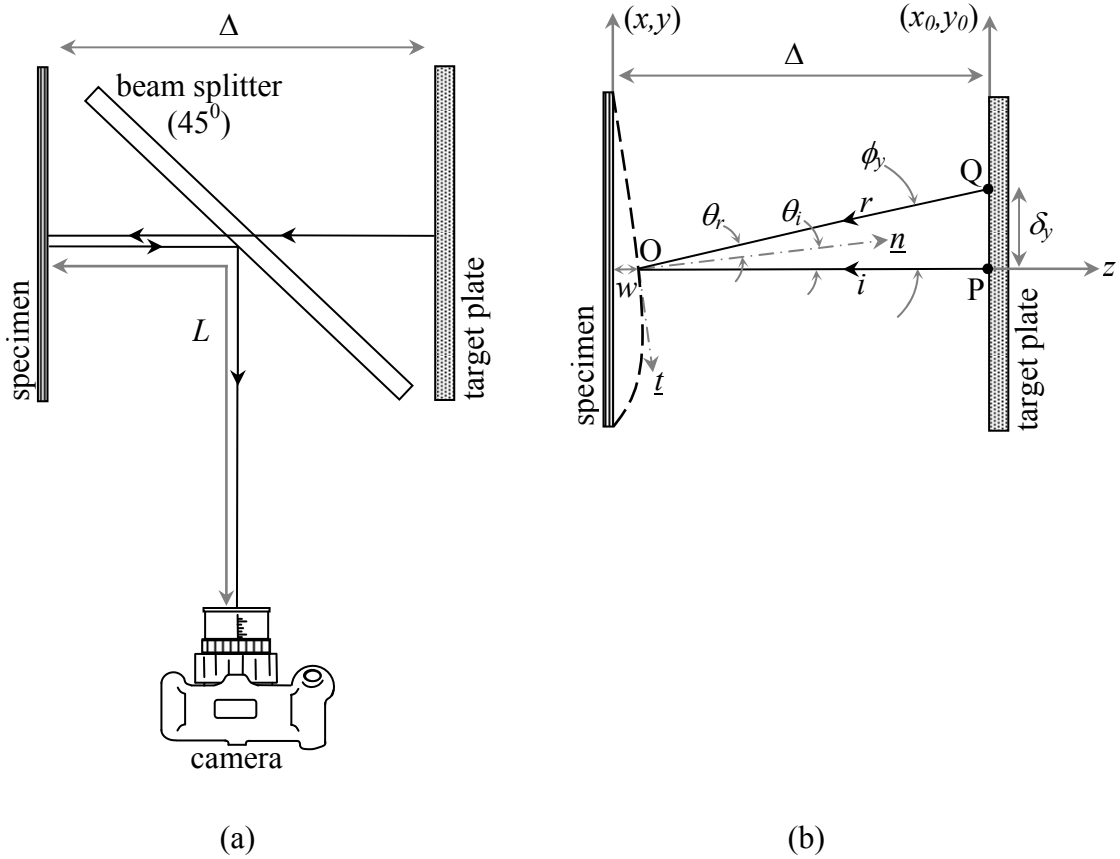

Figure 9.1: (a) Schematic of DGS experimental setup in reflection. (b) Optical path between the specimen and target (without beam splitter for simplicity); $\underline{n}$ and $\underline{t}$ denote unit vectors normal to and tangential to the specimen surface.

9.2 Working principle

Let (x, y) and (x_0, y_0) be the in-plane coordinates of the specimen and target planes, respectively. (Refer to Fig. 2.2 for a relative comparison with the schematic for the transmission mode DGS). Let a point P on the target plane be initially in focus when the specimen is flat and undeformed. In this condition, the incident (i) and reflected (r) rays will be collinear and parallel to the optical axis. Now, when the specimen undergoes out-of-plane deformation, OP gets deflected to OQ by an angle ϕ_y (= $\theta_i + \theta_r$; $\theta_i = \theta_r$, and $\underline{n}$ denotes the unit normal to the object surface at O) and brings point Q to focus as shown in Fig. 9.1(b). If the distance δ_y (and δ_x in the orthogonal direction) can be measured, and Δ known, the local surface slopes can be calculated as,

$$\frac{\partial w}{\partial x : y} = \frac{1}{2}\tan\left(\phi_{x:y}\right) = \frac{1}{2}\left(\frac{\delta_{x:y}}{\Delta}\right). \tag{9.1}$$

For small angular deflections, this can be written as,

$$\frac{\partial w}{\partial x : y} \simeq \frac{1}{2}\phi_{x:y} \simeq \frac{1}{2}\frac{\delta_{x:y}}{\Delta}. \tag{9.2}$$

9.3 Surface slopes of a silicon wafer subjected to central load

Next, the feasibility of reflection mode DGS method to measure surface slopes in planar reflective surfaces is demonstrated. The experimental setup is schematically shown in Fig. 9.2. The specimen is a one-side polished, 280 μm thick silicon wafer of

diameter 50.8 mm. The unpolished side of the wafer is glued onto a thick steel washer using epoxy adhesive. The inner and outer diameters of the washer are 25.7 mm and 76.2 mm, respectively. Another steel plate with a circular aperture was mounted with a micrometer (least count = 10 μm) and placed behind the silicon wafer inside a cylindrical holder. Both the steel washer (with the wafer) and the steel plate (with the micrometer) were secured tight by the retaining ring of the cylindrical holder. The entire assembly was then placed in front of a Nikon D3100 DSLR camera such that the reflective side of the wafer was facing the camera. The camera was fitted with an extension tube and a 70-300 mm lens. Then, a beam splitter was positioned between the wafer and the camera at an angle of 45 degrees to the optical axis of the camera.

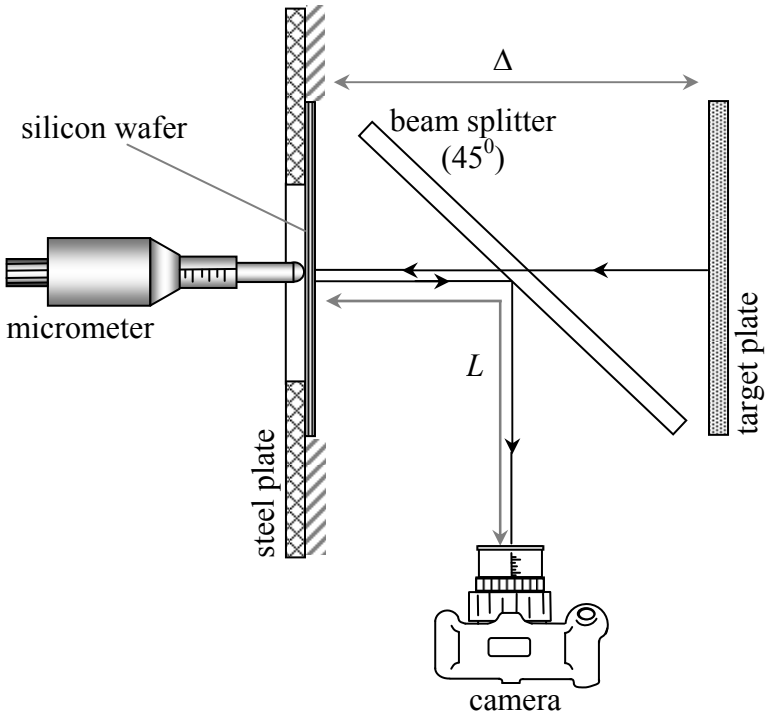

Figure 9.2: Schematic of the experimental setup for reflection mode DGS to measure surface slopes in a silicon wafer subjected to out-of-plane displacement.

The target plane, coated with a random black and white speckle pattern was placed perpendicularly by the side of the specimen at a distance of Δ = 66 mm. Now, the camera was focused on the speckle plane via the reflective face of the silicon wafer and an image was recorded. This recording is the reference or the undeformed image. Then, using the micrometer, a central out-of-plane displacement, w = 30 μm was applied to the wafer. This introduced a deformation of the specimen in the central circular region of 25.7 mm diameter resulting in a distorted speckle field relative to the undeformed counterpart (Fig. 9.3). This distorted / deformed image produced due to the deflection of light rays was recorded by the camera. The two images were correlated using the method of 2D DIC to extract δ_x and δ_y fields. Then, using Eq. 9.1, the surface slopes $\frac{\partial w}{\partial x}$ and $\frac{\partial w}{\partial y}$ were calculated over the entire circular region and are shown in Fig. 9.4. The surface slopes for a thin elastic plate subjected to a central deflection by a point force is given by [57]

$$\frac{\partial w}{\partial x} = \frac{4xw}{R^2}\log\left(\frac{\sqrt{x^2+y^2}}{R}\right),$$
$$\frac{\partial w}{\partial y} = \frac{4yw}{R^2}\log\left(\frac{\sqrt{x^2+y^2}}{R}\right), \tag{9.3}$$

where w is the out-of-plane displacement and R is the clamped radius of the wafer. The analytical results from the above equations are superposed on the experimentally obtained contours in Fig. 9.4 as broken lines. Figure 9.5 shows plots of radial variations of $\frac{\partial w}{\partial x}$ and $\frac{\partial w}{\partial y}$ along the x- and y- axes, respectively.

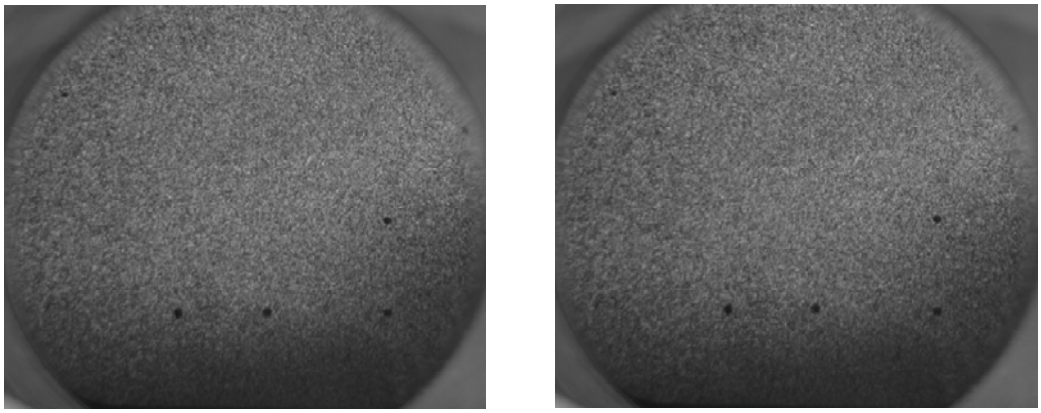

Figure 9.3: Reference (left) and deformed (right) images of speckles photographed off a thin silicon wafer subjected to central out-of-plane displacement of 30 μm.

From the two plots, it can be seen that the experimental results generally agree with the closed form solutions. Careful observation of Fig. 9.5 reveals that the peaks of the measured data occur farther from the wafer center when compared to the analytical counterparts. This can be attributed to the fact that the epoxy used to glue the wafer to the washer is compliant to some extent, whereas the analytical solution assumes an ideally rigid clamp. The measured data being non-zero at $x:y \rightarrow R$ further substantiates this possibility. Another reason is the steeper deflections of light rays at the wafer center that cause the speckles to appear smudged in the deformed image, which in turn introduces a degree of speckle decorrelation in that region.

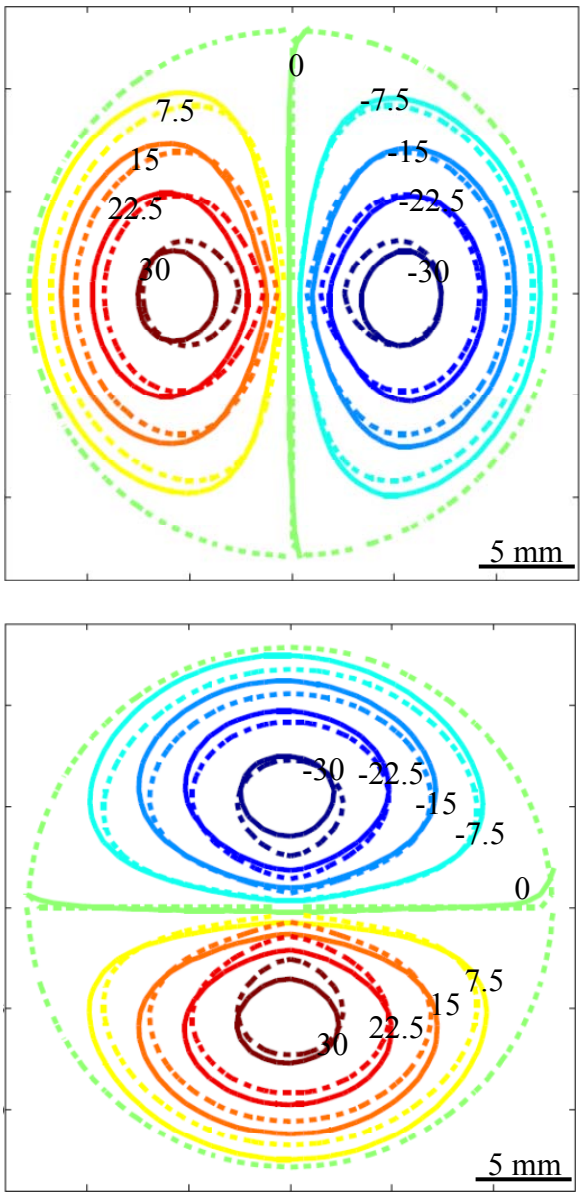

Figure 9.4: Experimental (solid lines) and analytical (dashed lines) contours of $\frac{\partial w}{\partial x}$ (top) and $\frac{\partial w}{\partial y}$ (bottom) corresponding to a circumferentially fixed silicon wafer subjected to a 30 μm central out-of-plane displacement. Contour levels are in 1×10^{-4} radians.

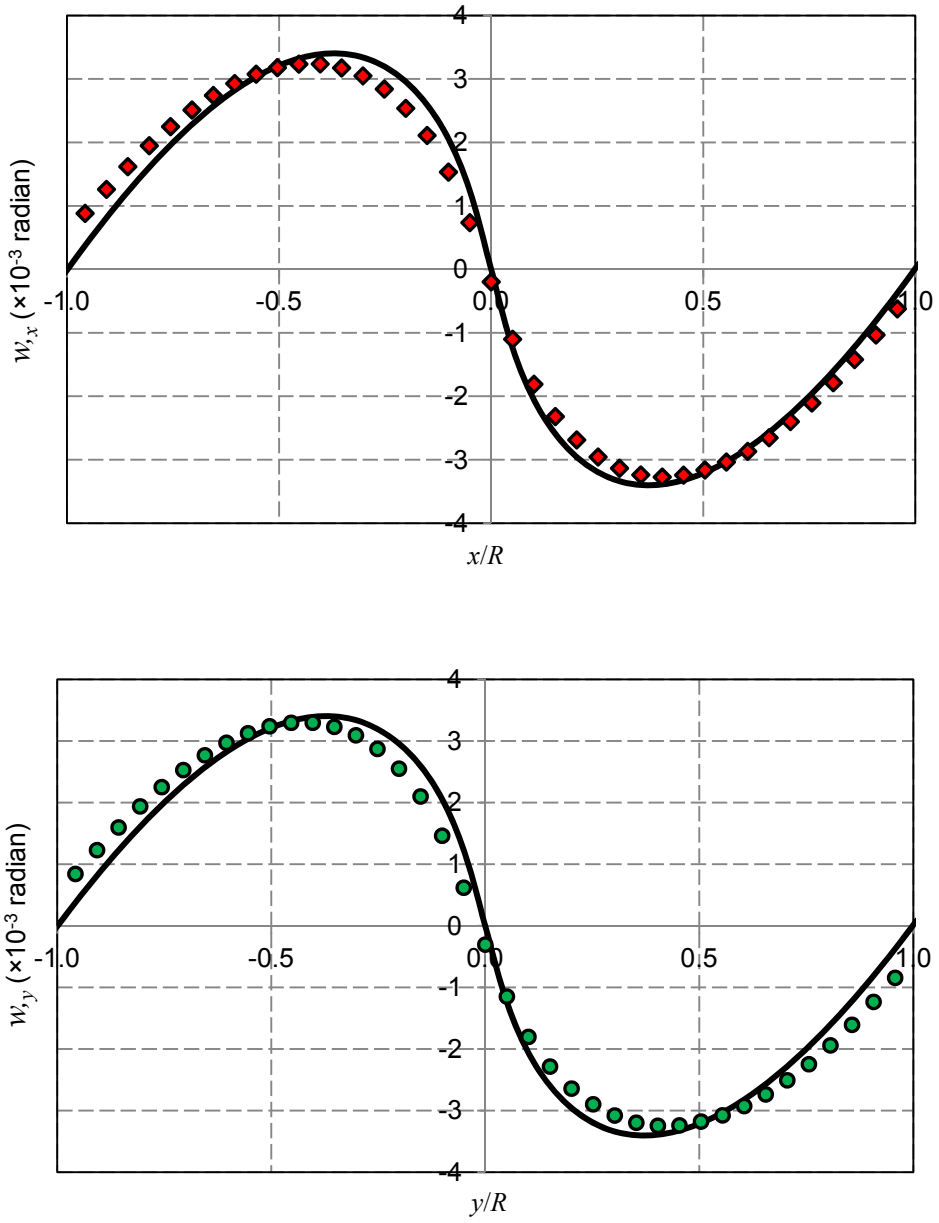

Figure 9.5: Analytical (solid lines) and experimental (symbols) data of $w_{,x} = \frac{\partial w}{\partial x}$ (top) along the x-axis and $w_{,y} = \frac{\partial w}{\partial y}$ (bottom) along the y-axis corresponding to a clamped silicon wafer subjected to a 30 μm central out-of-plane deflection.

9.4 Surface curvatures of a silicon wafer subjected to central load

One of the advantages of digital image processing is being able to obtain full-field derivatives from the measured data. In reflection DGS, δ_x and δ_y measurements being proportional to surface slopes, the measurements can be differentiated with respect to the spatial coordinates to obtain curvatures. Most DIC softwares offer such a facility since displacement derivatives are integral to speckle/texture correlation algorithms. Accordingly, derivatives of DGS measurements were obtained using the in-built algorithms of ARAMIS, and related to the respective curvatures as,

$$\begin{aligned} \frac{\partial^2 w}{\partial x^2} &= \frac{1}{2}\frac{\partial}{\partial x}\left(\frac{\delta_x}{\Delta}\right), \\ \frac{\partial^2 w}{\partial y^2} &= \frac{1}{2}\frac{\partial}{\partial y}\left(\frac{\delta_y}{\Delta}\right). \end{aligned} \tag{9.4}$$

For the parameters used in the DGS results, curvatures of the order of 10^{-4} mm^{-1} were discernible from the measurements.

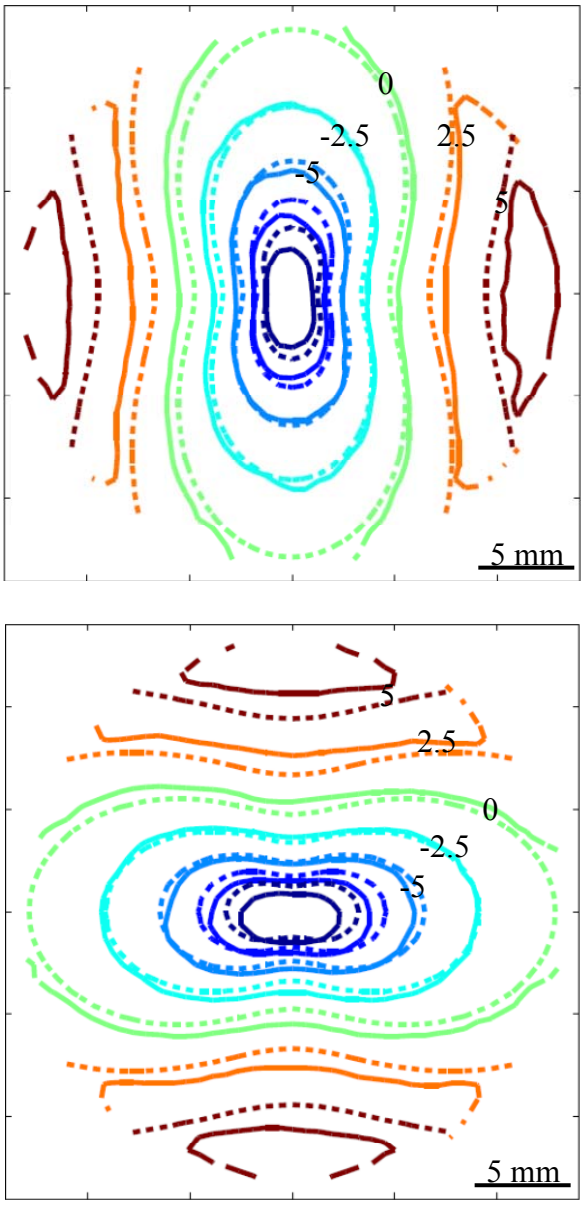

Figure 9.6: Experimental (solid lines) and analytical (dashed lines) contours of $\frac{\partial^2 w}{\partial x^2}$ (top) and $\frac{\partial^2 w}{\partial y^2}$ (bottom) corresponding to a circumferentially fixed planar silicon wafer subjected to a central 30 μm out-of-plane displacement. Contour levels are in 1×10^{-4} mm^{-1}.

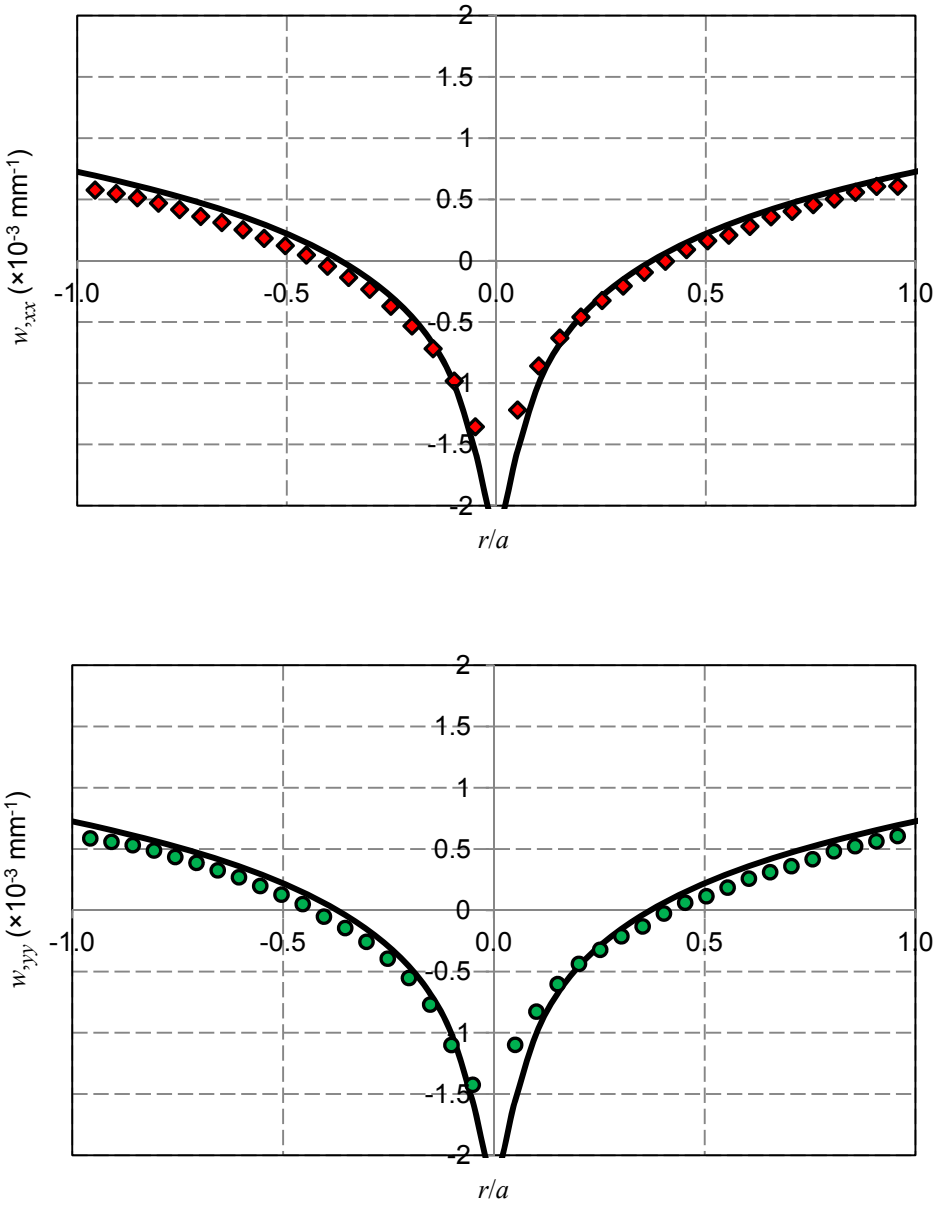

Figure 9.7: Experimental (solid lines) and analytical (symbols) plots of $w_{,xx} = \frac{\partial^2 w}{\partial x^2}$ (top) along horizontal diameter and $w_{,yy} = \frac{\partial^2 w}{\partial y^2}$ (bottom) along vertical diameter corresponding to a circumferentially fixed silicon wafer subjected to a 30 μm central out-of-plane displacement.

The contour plots of curvatures thus obtained are shown in Fig. 9.6. As expected, larger curvatures occur close to the loading point. For comparison, the analytical curvature fields given by [57]

$$\frac{\partial^2 w}{\partial x^2} = \frac{4w}{R^2}\log\left(\frac{\sqrt{x^2+y^2}}{R}\right) + \frac{4x^2 w}{R^2\left(x^2+y^2\right)}$$
$$\frac{\partial^2 w}{\partial y^2} = \frac{4w}{R^2}\log\left(\frac{\sqrt{x^2+y^2}}{R}\right) + \frac{4y^2 w}{R^2\left(x^2+y^2\right)} \tag{9.5}$$

are also superposed on the experimental contours. The measured curvature distribution is in qualitative agreement with the predictions. From Fig. 9.6, a slight non-conformity between measured data and analytical solutions is evident. This can be partly attributed to the numerical error from the differentiation process. Figure 9.7 shows plots of radial variations of $\frac{\partial^2 w}{\partial x^2}$ and $\frac{\partial^2 w}{\partial y^2}$ along the *x*- and *y*- axes, respectively. Given the fact that the epoxy used to glue the wafer to the steel plate is not perfectly rigid, the agreement between the measured and analytical fields are indeed good.

The availability of full-field digital / numerical data also facilitates numerical differentiation of one surface slope field with respect to either of the two orthogonal coordinates. Therefore, it is possible to calculate gradients of $\frac{\partial w}{\partial x}$ and $\frac{\partial w}{\partial y}$ with respect to the *y*- and *x*- axes to obtain $\frac{\partial^2 w}{\partial x \partial y}$ and $\frac{\partial^2 w}{\partial y \partial x}$, respectively. The results thus obtained are shown in Fig. 9.8. As expected, the two curvature fields are nearly identical qualitatively as well as quantitatively after allowing for experimental and numerical errors.

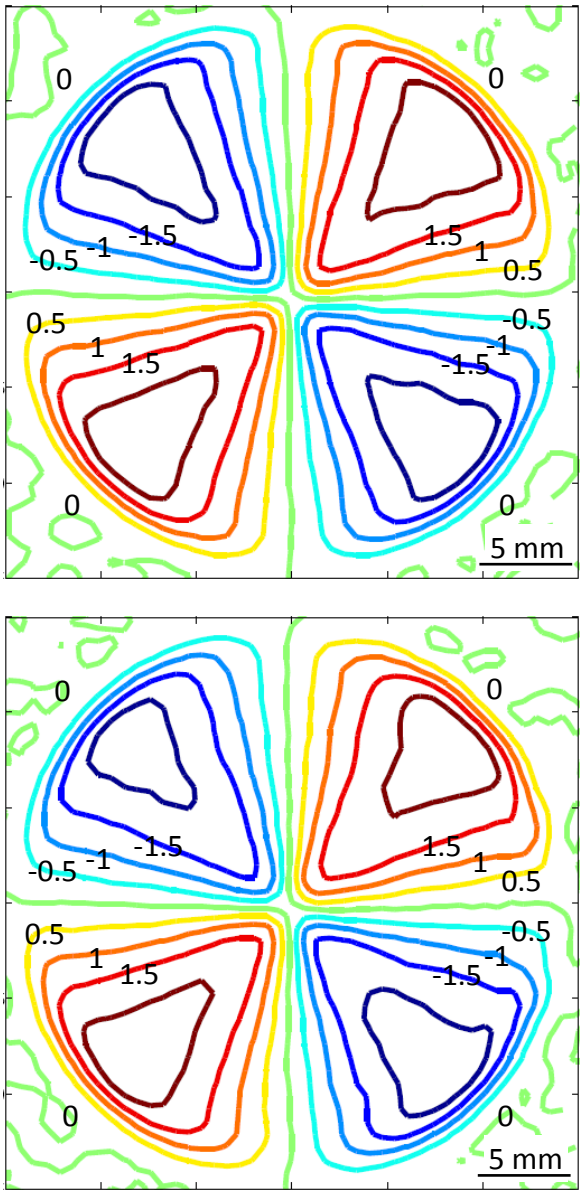

Figure 9.8: Contour plots of $\frac{\partial^2 w}{\partial x \partial y}$ (top) and $\frac{\partial^2 w}{\partial y \partial x}$ (bottom) corresponding to a circumferentially fixed silicon wafer subjected to a 30 μm central out-of-plane displacement. Contour levels are in 1×10^{-4} mm^{-1}.

10

Conclusions

An optical full-field measurement technique called Digital Gradient Sensing (DGS) was developed for measuring angular deflections of light rays in transparent and reflective objects which can be further related to stress gradients and surface slopes, respectively. The transmission mode DGS method is based on the elasto-optic effect and uses 2D digital image correlation methodology to quantify the angular deflections in two orthogonal planes. DGS employs a relatively simple experimental setup and requires ordinary white light for illumination. The availability of sophisticated digital recording technology and image processing algorithms offer enhanced capabilities to the DGS technique. The potential of the method to inspect and evaluate phase objects (such as lenses) or characterize the mechanical performance of transparent structural materials (such as transparent armor) are enormous.

The working principle of transmission mode DGS has been explained and the necessary governing equations have been derived. The analysis shows that the method is capable of measuring small angular deflections of light rays produced by *non-uniform* changes in the thickness and/or refractive index of the material. In mechanically loaded

planar objects, the angular deflections are in turn related to the gradients of first invariant of stresses, $\frac{\partial\left(\sigma_{xx}+\sigma_{yy}\right)}{\partial x}$ or $\frac{\partial\left(\sigma_{xx}+\sigma_{yy}\right)}{\partial y}$ under plane stress conditions. The DGS method has been first demonstrated using angular deflection fields produced by a plano-convex spherical lens. The measured contours of constant angular deflection of light rays and the deduced focal length are in good agreement with the expected value. Subsequently, several calibration and benchmark experiments have been performed to validate the DGS measurements. For the chosen experimental/optical parameters in this work, the achievable accuracy is approximately $1\text{x}10^{-4}$ radians.

The method has been successfully implemented to study a stress concentration problem involving a line load acting on the edge of a large planar sheet under both quasi-static and dynamic loading conditions. In regions outside the zone of dominant stress triaxiality, the measured angular deflections are in good agreement with the ones based on the Flamant's solution for a line load acting on the edge of a half-space. For the impact loading case, the angular deflections are compared with the numerical results obtained by performing a complementary elasto-dynamic finite element analysis of the problem. The angular deflections corresponding to post failure regime are also reported. It has also been shown that by combining the two simultaneously measured orthogonal stress gradients and with the aid of the analytical solutions, it is possible to estimate the stresses $\left(\sigma_{xx}+\sigma_{yy}\right)$ in the load point vicinity. In addition, the feasibility of using far field data as boundary conditions to integrate the stress gradient fields and obtain stresses has also been demonstrated.

The transmission DGS method has also been successfully implemented to measure the stress gradient fields around a crack tip under both quasi-static and dynamic loading conditions. The quasi-static and dynamic stress intensity factors were computed by performing overdeterministic least-squares analysis on the measured optical data using prevailing crack tip field equations. The evolution of static and dynamic stress intensity factor histories were successfully compared with the ones obtained from the analytical solutions and finite element simulations. In addition, a good full-field qualitative and quantitative agreement between the measured angular deflection values and the analytical solutions was also seen. Further, the problem of a flat punch impacting the edge of a planar sheet was studied and the stress gradient fields around the punch tip were measured using DGS. Using the analogy between the problem of a compressively loaded double edge crack and the square punch problem, the analytical crack tip angular deflection field equations were used to extract the punch tip stress intensity factor history from measured deformation fields. The results are again in good agreement with the numerically obtained punch tip stress intensity factor history computed from the same analogy, but extracted using crack opening displacements.

The DGS technique has also been demonstrated in reflection mode by measuring angular deflections of reflected light rays from a polished silicon wafer subjected to out-of-plane displacements. The measured deflection contours with respect to the two in-plane specimen coordinates were related to the wafer surface slopes and compared with closed form solutions for a thin plate. A good agreement between the two is observed.

Furthermore, the surface slope fields were differentiated to obtain wafer curvatures which also show a good agreement with the ones from closed form solution of the problem.

The capabilities of the DGS technique make it a promising non-contacting, full-field measurement tool for various applications where deflection of light rays occur and need quantification. A few such possibilities have been explored towards the end of this work, and have been presented in the Appendix. Other venues where DGS could be applied are thermal stresses in aircraft windows, temperature field measurement in flames, density variations in jet flows, vibration/defect analysis of reflective thin plates, etc.

References

1. P. Patel, et al., "Transparent armor", AMPTIAC Newsletter, 4(3) (2000).
2. O. Kafri and A. Livnat, "Reflective surface-analysis using Moire deflectometry", Applied Optics, 20(18), 3098-3100 (1981).
3. E. Strassburger, "Ballistic testing of transparent armour ceramics", Journal of the European Ceramic Society, 29(2), 267-273 (2009).
4. Rubio-Gonzalez, C. and J.J. Mason, "Experimental investigation of dynamic punch tests on isotropic and composite materials", Experimental Mechanics, 41(2), 129-139 (2001).
5. A. Mohajerani and J.K. Spelt, "Edge chipping of borosilicate glass by low velocity impact of spherical indenters", Mechanics of materials, 43(11), 671-683 (2011).
6. H. Chai and G. Ravichandran, "On the mechanics of fracure in monoliths and multilayers from low-velocity impact by sharp or blunt-tip projectiles", 36, 375-385 (2009).
7. S. Iwamoto, A.N. Nakagaito, H. Yano and M. Nogi, "Optically transparent composites reinforced with plant fiber-based nanofibers", Applied Physics a-Materials Science & Processing, 81(6), CP8-1112, (2005).
8. E.J.A Pope, M. Asami, and J.D. Mackenzie, "Transparent silica gel-PMMA composites", Journal of Materials Research, 4(4), 1018-1026 (1989).
9. S. Ravi, "Development of transparent composite for photoelastic studies", Advanced Composite Materials, 7(1), 73-81 (1998).
10. H. Yano, J. Sugiyama, A.N. Nakagaito, M. Nogi, T. Matsuura, M. Hikita and K. Handa, "Optically transparent composites reinforced with networks of bacterial nanofibers", Advanced Materials, 17(2), 153-+ (2005).

11. A. Wells and D. Post, "The dynamic stress distribution surrounding a running crack. In: Proceedings for the Society of Experimental Stress Analysis, 16, 69-96 (1958).
12. J.G.A. de Graaf, "Investigation of brittle fracture in steel by means of ultra high speed photography", Applied Optics, 3(11), 1223-1229 (1964).
13. J.W. Dally, "Dynamic photo-elastic studies of fracture", Experimental Mechanics, 19(10), 349-361 (1979).
14. M.R. Ayatollahi and M. Nejati, "Experimental evaluation of stress field around the sharp notches using photoelasticity", Materials and Design, 32(2), 561-569 (2011).
15. V. Parameswaran and A. Shukla, "Dynamic fracture of a functionally gradient material having discrete property variation", Journal of Materials Science, 33(13), 3303-3311 (1998).
16. A.J. Rosakis, H. Kanamori and K. Xia "Laboratory earthquakes", International journal of fracture, 138(1-4), 211-218 (2006).
17. F.P. Chiang and R.M. Juang, "Vibration analysis of plate and shell by laser speckle interferometry", Optica Acta, 23(12), 997-1009 (1976).
18. F.P. Chiang, J. Adachi and R. Anastasi, "Applications of laser speckle interferometry to strain concentration measurement", Journal of the Optical Society of America, 66(2), 183-183 (1976).
19. W. Gindl and U. Muller, "Shear strain distribution in PRF and PUR bonded 3-ply wood sheets by means of electronic laser speckle interferometry", Wood Science and Technology, 40(5), 351-357 (2006).
20. A. Sretenovic, U. Muller and W. Gindl, "Mechanism of stress transfer in a single wood fiber-LDPE composite by means of electronic laser speckle interferometry", 37(9), 1406-1412 (2006).
21. J. Park, K. Jang, K. Paik and S. Lee, "A study of hygrothermal behavior of ACF flip chip packages with moire interferometry", IEEE Transactions on Components and Packaging Technologies, 33(1), 215-221 (2010).
22. K. Rozenburg, J.R. Berger, P.A. Martin and I. Reimanis, " Analysis of moire data for near-interface cracks", International Journal of Fracture, 143(3), 207-217 (2007).

23. P.C. Savalia and H.V. Tippur, "A study of crack-inclusion interactions and matrix-inclusion debonding using moire interferometry and finite element method", Experimental Mechanics, 47(4), 533-547 (2007).
24. P. Krehl and S. Engemann, "August Toepler - The first who visualized shock waves", Shock Waves, 5(1-2), 1-18 (1995).
25. S. Bernhard, E. Hans and G. Ali, "Experimental investigation of hot and cold side jet interaction with a supersonic cross-flow", Aerospace Science and Technology, 13, 488-496 (2009).
26. L.C. Forde, W.G. Proud, S.M. Walley, P.D. Church and I.G. Cullis, "Ballistic impact studies of a borosilicate glass", International Journal of Impact Engineering, 37(5), 568-578 (2010).
27. H.V. Tippur and A.J. Rosakis, "Quasi-static and dynamic crack-growth along bimaterial interfaces - A note on crack-tip field measurements using coherent gradient sensing", Experimental Mechanics, 31(3), 243-251 (1991).
28. H.V. Tippur, S. Krishnaswamy, and A.J. Rosakis, "Optical Mapping of Crack Tip Deformations Using the Methods of Transmission and Reflection Coherent Gradient Sensing - a Study of Crack Tip K-Dominance", International Journal of Fracture, 52(2), 91-117 (1991).
29. H.V. Tippur, "Coherent gradient sensing - A Fourier optics analysis and applications to fracture", Applied Optics, 31(22), 4428-4439 (1992).
30. H.V. Tippur, S. Krishnaswamy and A.J. Rosakis, "A coherent gradient sensor for crack tip measurements: Analysis and experimental results", International journal of fracture, 48, 193-204 (1991).
31. M. Budyansky, C. Madormo, J.L. Maciaszek and G. Lykitrafitis, "Coherent gradient sensing microscopy (micro-CGS): A microscale curvature detection technique", Optics and Lasers in Engineering, 49(7), 874-879 (2011).
32. J. Dhanotia and S. Prakash, "Collimation testing using coherent gradient sensing", Optics and Lasers in Engineering, 49(9-10), 1185-1189 (2011).
33. X.F. Yao, W. Xu and H.Y. Yeh, "Investigation of crack tip evolution in functionally graded materials using optical caustics", Polymer Testing, 26(1), 122-131 (2007).

34. J. Beinert and J.F. Kalthoff, Mechanics of Fracture, Nijhoff Publishers, Vol. 7, Ed., G.C. Sih, 281-328, (1981).
35. A.T. Zehnder and A.J. Rosakis, "A note on the measurement of K and J under small-scale yielding conditions using the method of caustics", International journal of fracture, 30(3), R43-R48 (1986).
36. S. Krishnaswamy and A.J. Rosakis, "On the extent of dominance of asymptotic elastodynamic crack-tip fields: An experimental study using bifocal caustics", Journal of applied mechanics - Transactions of the ASME, 58(1), 87-94 (1991).
37. Y.J. Chao, P.F. Luo and J.F. Kalthoff, "An experimental study of the deformation fields around a propagating crack tip", Experimental mechanics, 38(2), 79-85 (1998).
38. M.S. Kirugulige, H.V. Tippur and T.S. Denney, "Measurement of transient deformations using digital image correlation method and high-speed photography: application to dynamic fracture", Applied Optics, 46(22), 5083-5096 (2007).
39. M.S. Kirugulige and H.V. Tippur, "Measurement of surface deformations and fracture parameters for a mixed-mode crack driven by stress waves using image correlation technique and high-speed photography", 45(2), 108-122 (2009).
40. P.L. Reu and T.J. Miller, "The application of high-speed digital image correlation", Journal of strain analysis for engineering design, 43(8), 673-688 (2008).
41. J.W. Dally and W.F. Riley, "Experimental stress analysis", 4 ed., College House Enterprises (2005).
42. M.A. Sutton, U. Orteu, and H. Schreier, "Image Correlation for Shape, Motion and Deformation Measurements", Springer, (2009).
43. R.G. Budynas, "Advanced strength and applied stress analysis", McGraw-Hill (1998).
44. C. Periasamy, R. Jhaver and H.V. Tippur, "Quasi-static and dynamic compression response of a lightweight interpenetrating phase composite foam", Materials Science and Engineering-A, 527(12), 2845-2856 (2010).
45. R.J. Butcher, C.E. Rousseau, H.V. Tippur, "A functionally graded particulate composite: Preparation, measurements and failure analysis, Acta Materialia, 47(1), 259-268 (1998).
46. M. Meyers, 'Dynamic Behavior of Materials', John Wiley & Sons, Inc., 305-307 (1994).

47. C. Periasamy and H.V. Tippur, "Measurement of orthogonal stress gradients due to impact load on a transparent sheet using digital gradient sensing method", Experimental Mechanics", *accepted*, 2012.
48. L. Xu, H.V. Tippur and C.E. Rousseau,"Measurement of contact stresses using real-time shearing interferometry", Optical Engineering, 38(11), 1932-1937 (1999).
49. M. Janssen, J. Zuidema and R.J.H. Wanhill, "Fracture Mechanics", 2 ed., VSSD (2006).
50. C. Periasamy and H.V. Tippur, "A full-field digital gradient sensing method for evaluating stress gradients in transparent solids", Applied Optics, 51(12), 2088-2097 (2012).
51. S. Krishnaswamy, H.V. Tippur and A.J. Rosakis, "Measurement of transient crack tip deformation fields using the method of coherent gradient sensing", Journal of the Mechanics and Physics of Solids, 40(2), 339-372 (1992).
52. J. Beinert and J.F. Kalthoff, "Mechanics of fracture", Nijhoff Publishers, Vol. 7, Ed., G.C. Sih, 281-328 (1981).
53. Roessig, K.M. and J.J. Mason, "Dynamic stress intensity factors in a two dimensional punch test", Engineering Fracture Mechanics, 60(4), 421-435 (1998).
54. Chen, L. and R.C. Batra, "Material instability criterion near a notch-tip under locally adiabatic deformations of thermoviscoplastic materials", Theoretical and Applied Fracture Mechanics, 30(2), 153-158 (1998).
55. T.Y. Kao and F.P. Chiang, "Family of grating techniques of slope and curvature measurements for static and dynamic flexure of plates", Optical Engineering, 21(4), 721-742 (1982).
56. R. Ritter, "Reflection moire methods for plate bending studies", Optical Engineering, 21(4), 663-671 (1982).
57. H.V. Tippur, "Simultaneous and real-time measurement of slope and curvature fringes in thin structures using shearing interferometry", Optical engineering, 43(12), 3014-3020 (2004).
58. A.J. Rosakis, K. Ravichandar, "On crack-tip stress state - an experimental evaluation of 3-dimensional effects", International Journal of Solids and Structures, 22(2), 121-134 (1986).

59. S.H. Mortazavi, M. Ghoranneviss and S. Faryadras, "Effect of low pressure nitrogen DC plasma on optical properties of biaxial-oriented polypropylene (BOPP), poly methyl methacrylate (PMMA) and poly vinyl chloride (PVC) films", Journal of Fusion Energy, 31(3), 211-215 (2012).
60. Lai Chuan-Yar, T. Ponting and E. Baer, "Influence of interdiffusion on multilayered gradient refractive index (GRIN) lens materials", Polymer, 53(6), 1393-1403 (2012).

Appendix

A1 Stress triaxiality near a line-load on an edge

In Chapter 4, the DGS-based load measurements deviated from the imposed value in the close vicinity of the loading point. This was attributed to three dimensional deformations approximated by a plane stress state. This section serves to quantify the stress triaxiality zone near a line load acting on the edge of a planar sheet. A 3D finite element model of a rectangular PMMA sheet subjected to a line load on its edge was developed. The dimensions ($180 \times 69.5 \times 9.4$ mm^3) of the model used were same as that of the specimen used in experiments described in Chapter 4. Symmetries about the mid-plane of the specimen and the loading axis were used in the model. An arbitrary line load was applied on one side of the model (Fig. A1.1). The face opposite to the load was simply supported (sliding was permitted in the direction perpendicular to the loading direction). The model was discretized into 225180 linear hexahedral elements (~1 mm edge length) with 5 elements along the (half) thickness.

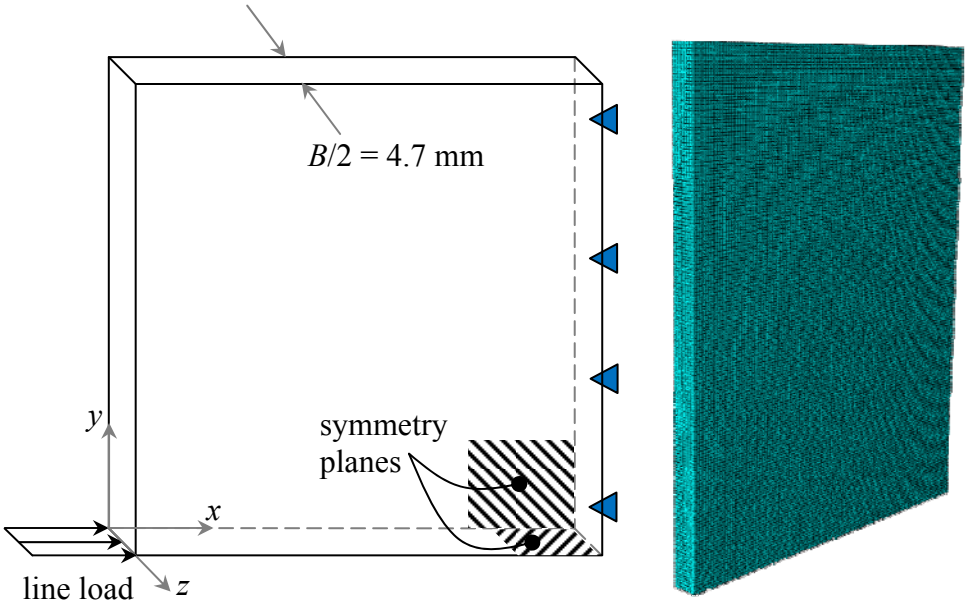

Figure A1.1: Schematic (left) and discretized geometry (right) of the finite element model for a line-load problem.

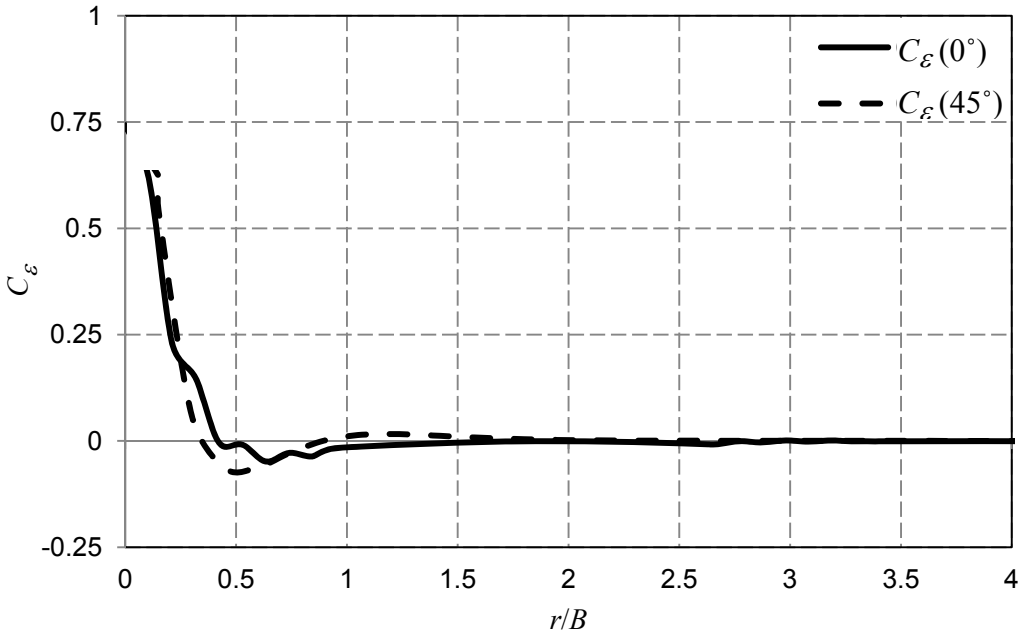

Figure A1.2: Radial variation of plane strain constraint (C_ε) near a line load in a planar sheet of thickness 9.4 mm.

From the 3D elasto-static numerical solution, the plane strain constraint [58] parameter $C_\varepsilon = -\dfrac{\sigma_z}{\upsilon\left(\sigma_x + \sigma_y\right)}$ was obtained on the mid-plane of the model. For a plane stress condition to prevail, the above quantity should vanish. To verify the radial extent from the loading point where plane stress conditions in the PMMA model prevails, C_ε was obtained along 0˚ and 45˚ from the loading axis, and are plotted as functions of normalized radial distance in Fig. A1.2. From the figure, it is clear that the triaxial stress zone in a plate of dimensions used in Chapter 4 subjected to a line-load extends up to approximately $r/B = 0.5$.

A2 Effect of in-plane displacements on DGS

In a transmission mode DGS experiment, a specimen deforms while the target (speckle) plane remains stationary. Further, a uniform state of stress producing constant thickness and refractive index changes should not result in non-uniform angular deflection field. To ensure this experimentally, an experiment using DGS was carried out. For the sake of discussion, let a point P on the speckle plane be initially in focus through a point O in the specimen under no-load condition as shown in Fig. A2.1. Now, assume that the specimen deforms uniaxially in the *y*-direction. Let the deformation cause an adjacent point O' to move to the position initially occupied by O. Moreover, as the stress state in the specimen would have changed after deformation, light rays would deflect and bring a point, say Q to focus instead of P. Therefore, a question arises as to whether the in-plane

displacements of the specimen would have any influence in the angular deflection measurements in addition to thickness and refractive index changes.

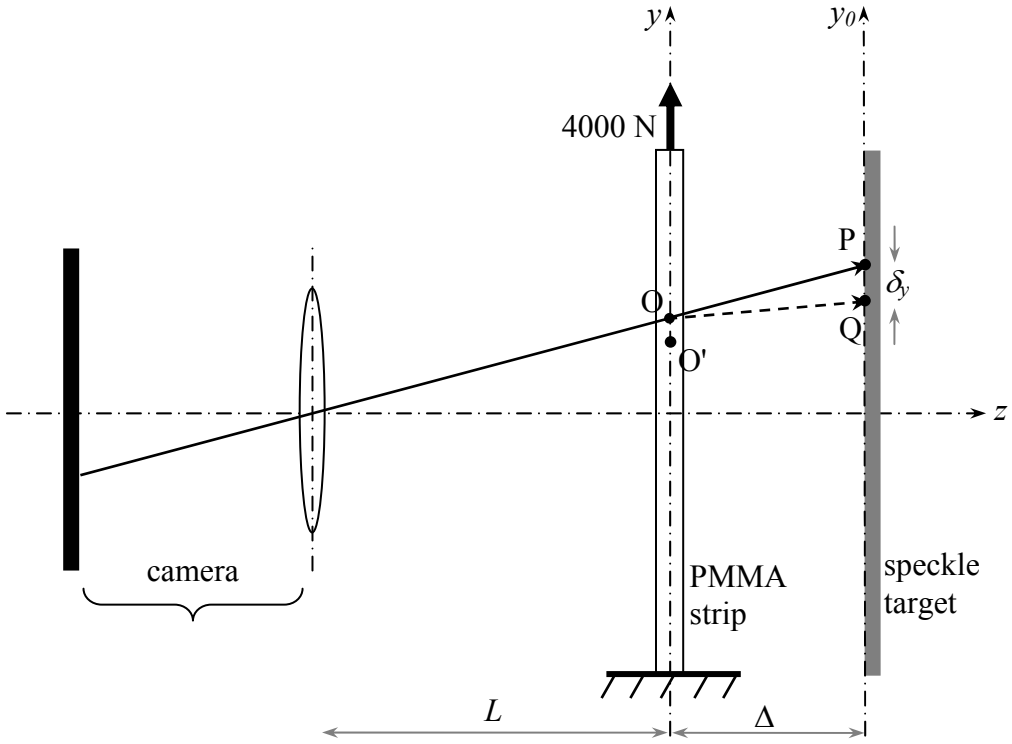

Figure A2.1: Schematic of a DGS experiment to evaluate angular light deflections produced by a uniaxially loaded PMMA plate.

To investigate this, a uniaxial tensile test was carried out on a PMMA sheet. The resulting contours should be uniformly zero, due to the absence of stress gradients. If there is any influence of the linearly varying displacement field, a regular contour pattern should occur. To verify the above, a PMMA sheet, 19.6 mm wide and 5.9 mm thick was subjected to a uniaxial tension using Instron 4465 universal testing machine. The other experimental parameters used were, L = 1450 mm and Δ = 28.3 mm. A reference image

was recorded under a preload of a few Newtons. Then, a tensile force of 4000 N was applied (σ_{yy} = 34.6 MPa), which resulted in a uniform thickness change of ~ 20 μm in the specimen.

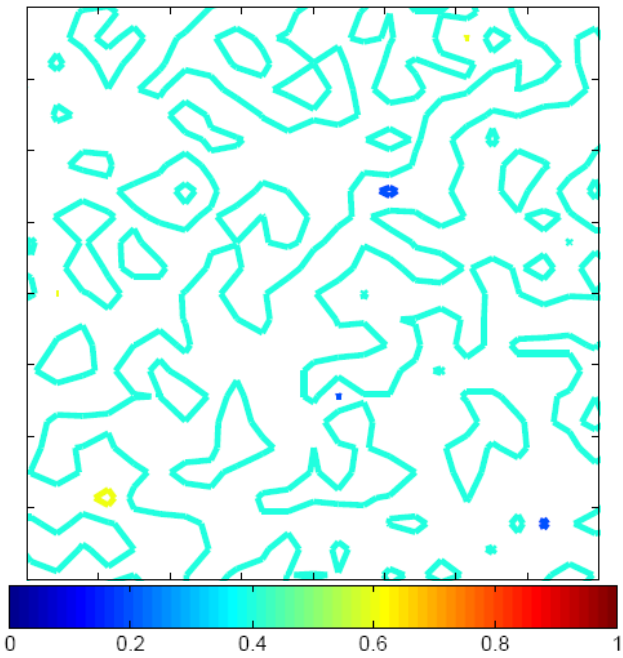

Figure A2.2: Angular deflection contours of ϕ_y for a uniaxially loaded PMMA strip. Contour levels are in $\times 10^{-3}$ radian.

The angular deflection field in the loading direction was obtained from the reference and deformed images and is shown in Fig. A2.2. The deflection field is uniform in the direction of specimen displacement, which substantiates that the in-plane displacements have no influence on the DGS measurements. The deflections recorded in the field are approximately 3×10^{-4} radians which is close to the resolution of the method.

A3 Refractive index measurement using DGS

Light rays refract as they travel through media having different refractive indices. Therefore, it is possible to quantify the refractive index of a transparent constant thickness sheet using DGS, since it is capable of measuring angular deflections of light rays. In Fig. A3.1, assume a light ray traveling in air be incident at a point O on a transparent, optically homogeneous, planar medium of thickness B and refractive index n at an angle of θ_i relative to the surface normal. Due to the difference in refractive indices of air and the planar medium, the light ray will deflect towards the normal (assuming $n >$ 1) to the surface. Let this refracted ray form an angle θ_r with the normal. As the light ray exits the planar medium at Q', it will now deflect away from the normal, parallel to the original incident direction. On the other hand, path of the light ray would have been OQ if there was no second medium. It is obvious that the vertical distance δ_y between Q and Q' is a result of the difference in densities (refractive indices) of the two media. This displacement can be measured using DGS and related to the refractive index of the transparent medium. For verification, a PMMA plate was used to experimentally obtain displacement fields δ_x and δ_y and compared with the analytical counterparts.

Experimental details

The schematic of the experimental setup to capture δ_y is shown in Fig. A3.2. A target plane with the speckle pattern was placed at a sufficiently large distance of ~1275 mm from a camera (Nikon D100 digital camera fitted with a 28-300 mm lens using an

extension tube and aperture setting #11). A reference (undeformed) image of the speckle pattern was recorded first. Then, a clear 9.4 mm thick PMMA plate was introduced between the camera and the speckle plane. The distance from the mid-plane of the specimen to the speckle plane, Δ was 30.7 mm. A second image of the speckle pattern, this time through the PMMA plate, was recorded. The size of the image recorded by the camera was approximately 64 x 42 mm^2 rectangle in the central region of the PMMA.

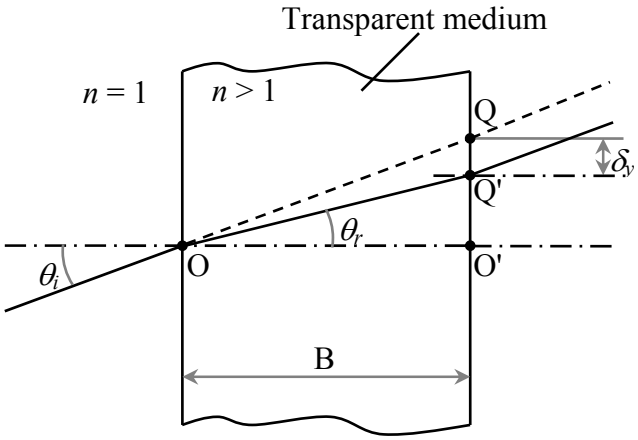

Figure A3.1: Schematic to explain the optical path change of light rays traveling through media of different refractive indices.

The recording of the reference and perturbed speckle fields used a pixel resolution of 1504 x 1000 pixels (1 pixel = 43.54 μm on the target plane). The second speckle image can be considered to be the "perturbed" image whose δ_y field is given by,

$$\delta_y = O'Q - O'Q' = B\left(\tan\theta_i - \tan\theta_r\right). \tag{A3.1}$$

Also, from the Snell's law, $\frac{\sin\theta_i}{\sin\theta_r} = \frac{n}{1}$. For small angles (paraxial approximation), $\theta_r = \frac{\theta_i}{n}$. Therefore, Eq. (A3.1) becomes

$$\delta_y = B\theta_i\left(1 - \frac{1}{n}\right). \tag{A3.2}$$

Now, from Fig. A3.2, $\tan\theta_i = \frac{y_t}{L+\Delta}$. Substituting this relation in Eq. (A3.2), and assuming small θ_i and θ_r, we get,

$$\delta_y = \frac{By_t}{L+\Delta}\left(1 - \frac{1}{n}\right). \tag{A3.3}$$

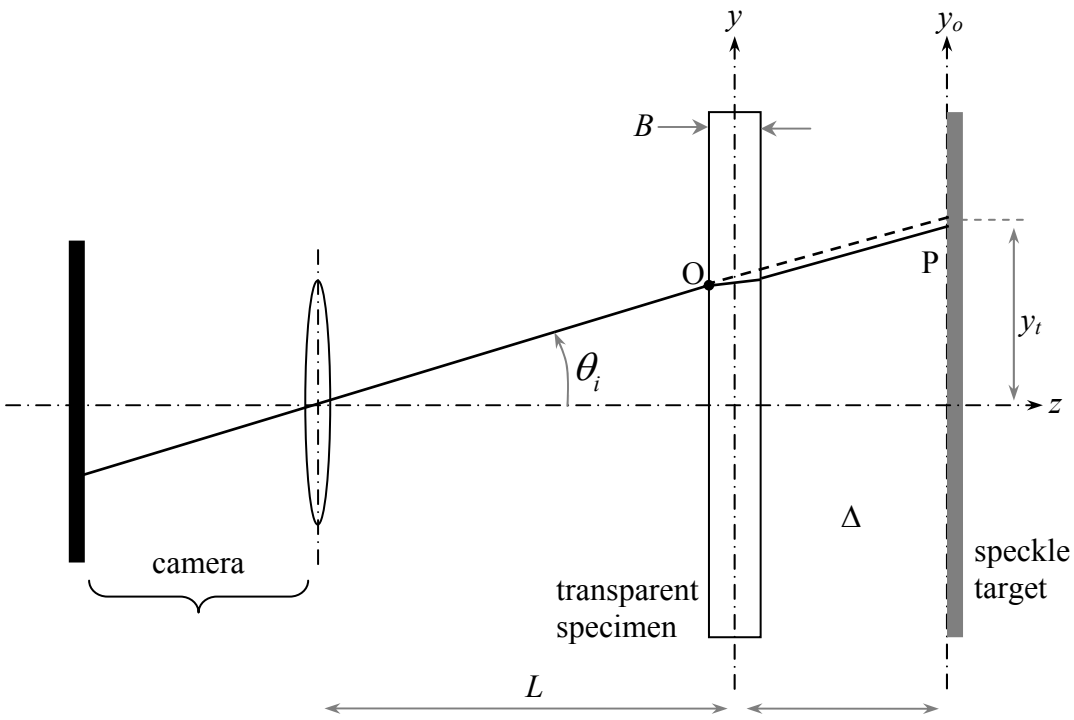

Figure A3.2: Schematic of the experimental set up used to capture the optical path change of light rays traveling through media of different refractive indices.

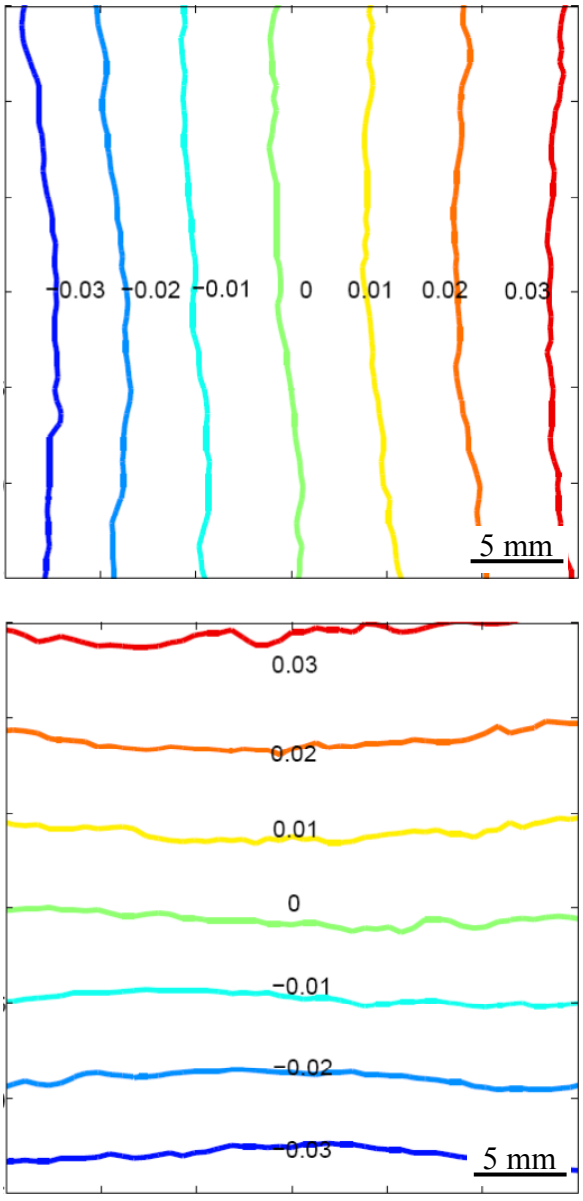

Figure A3.3: Contour plots of measured δ_x (top) and δ_y (bottom) fields. Contour levels are in mm.

A similar expression for the horizontal component of displacement, δ_x is to be implicitly understood. By rearranging Eq. (A3.3), the refractive index of the specimen

can be obtained. As evident from the above equation, the displacement fields, δ_x and δ_y are linear functions of the specimen's x- and y-coordinates, respectively. Hence, the contours of constant δ_x and δ_y should be equally spaced. In addition, for an optically homogeneous medium, the contours should be equally spaced lines parallel to the two coordinates. These can be used to verify Eq. (A3.3). The in-plane displacement fields were extracted from the undeformed and deformed images by performing 2D digital image correlation. The contour plots of the experimentally obtained δ_x and δ_y are shown in Fig. A3.3. As predicted, the contours are approximately equidistant and parallel lines. Any departure from the parallelism can be attributed to the optical inhomogeneity and non-uniform thickness of the specimen besides other experimental errors. An average value of refractive index computed based on the contour spacing is n = 1.44, which is close to that of commercial PMMA found in the literature [59, 60].

A4 Inspection of glass for inhomogeneities and defects using DGS

This section presents a promising commercial application of DGS as an engineering inspection tool. The application is to measure angular deflections of light rays in commercial glass, where DGS can be easily implemented as an inspection tool to investigate the optical homogeneity qualitatively as well as quantitatively. To demonstrate the feasibility to measure angular deflections caused by inhomogeneities and defects, a borosilicate plate of dimensions 50×50×2.8 mm^3 was deliberately subjected to a thermal load caused by a brief exposure to its center the flame of a blow torch. This

introduced thermal stresses in the glass specimen upon cooling. The schematic of the experimental setup used to visualize and quantify the inhomogeneity is shown in Fig. A4.1. A Nikon D100 digital camera fitted with a 28-300 mm lens and an extension tube was placed at a distance $L \sim 1000$ mm from where the glass specimen is to be positioned. A target plane decorated with a random black and white speckle pattern was placed behind the specimen location at a distance $\Delta = 27.1$ mm from the mid-plane of the specimen. The camera was focused on this plane when the specimen was not in the path of observation. The aperture was set to #11 in the lens and the sensor resolution used was 1504 × 1000 pixels (1 pixel = 35.6 μm).

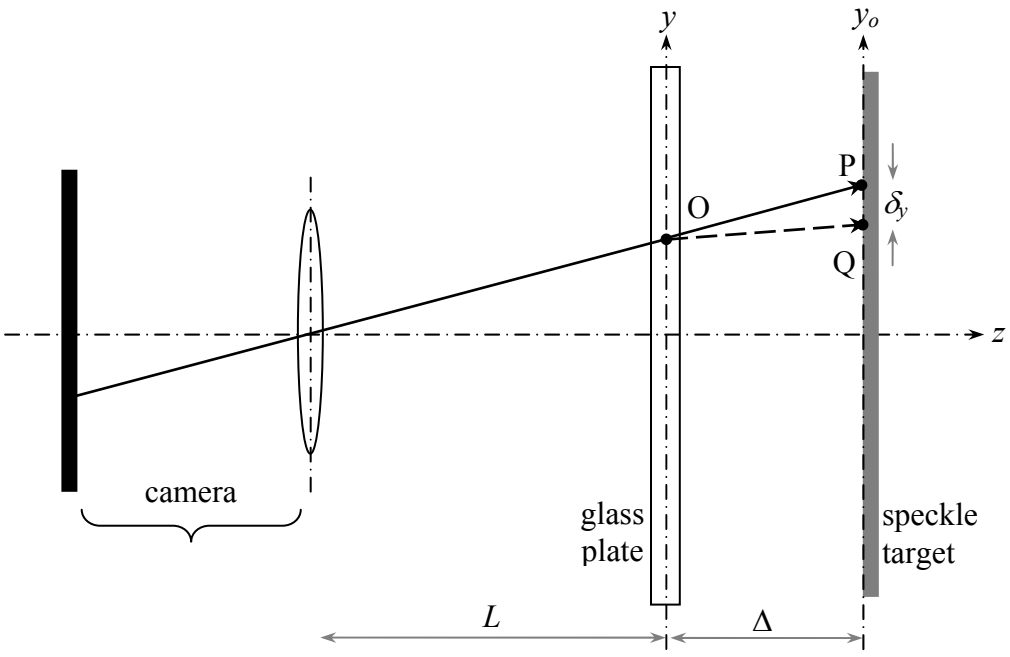

Figure A4.1: Schematic of the experimental set up used to measure angular deflections in a thermally stressed borosilicate glass plate using DGS.

A reference image of the speckle plane was recorded. Then, the thermally stressed specimen was moved into position as shown in Fig. A4.1. This made the speckles appear distorted when looked through the defective specimen (Fig. A4.2). The distorted / deformed image was now recorded using the same camera settings. The two images were then processed using 2D DIC to obtain δ_x and δ_y fields. The angular deflection fields (ϕ_x and ϕ_y) were then obtained by dividing δ_x and δ_y by the separation distance Δ (Section 2.2). The results are plotted in Fig. A4.3. The angular deflection contours show a clear evidence of a nearly circular heat affected zone (HAZ) in the mid-field of view, signified by a dense cluster of contours along the periphery of the HAZ. Away from the HAZ, the field consists of nominally parallel angular deflection contours along the horizontal and vertical directions in the ϕ_x and ϕ_y fields. The parallel contours can be explained by the reasons provided in Section A3.

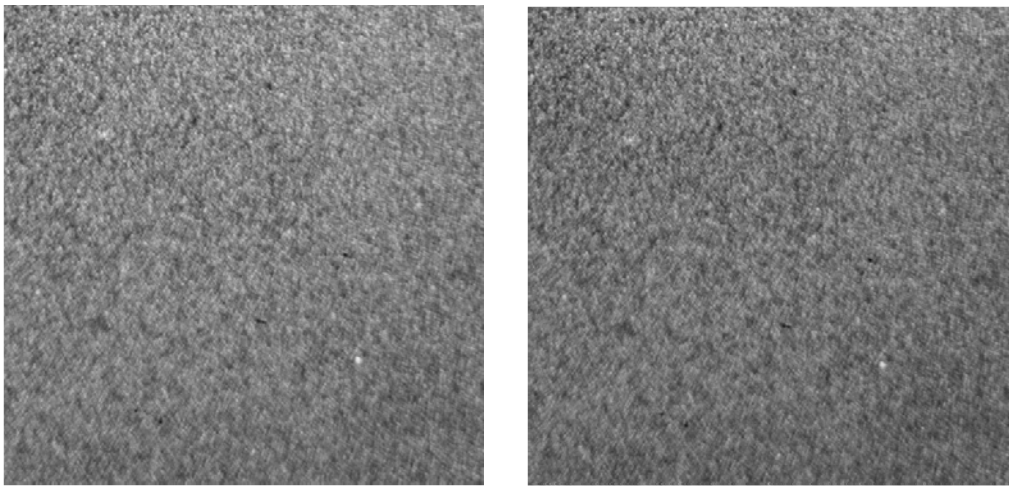

Figure A4.2: Reference (left) and deformed (right) image of speckles recorded through an optically inhomogeneous borosilicate glass plate. (The perturbation of speckles is not discernible to the human eye)

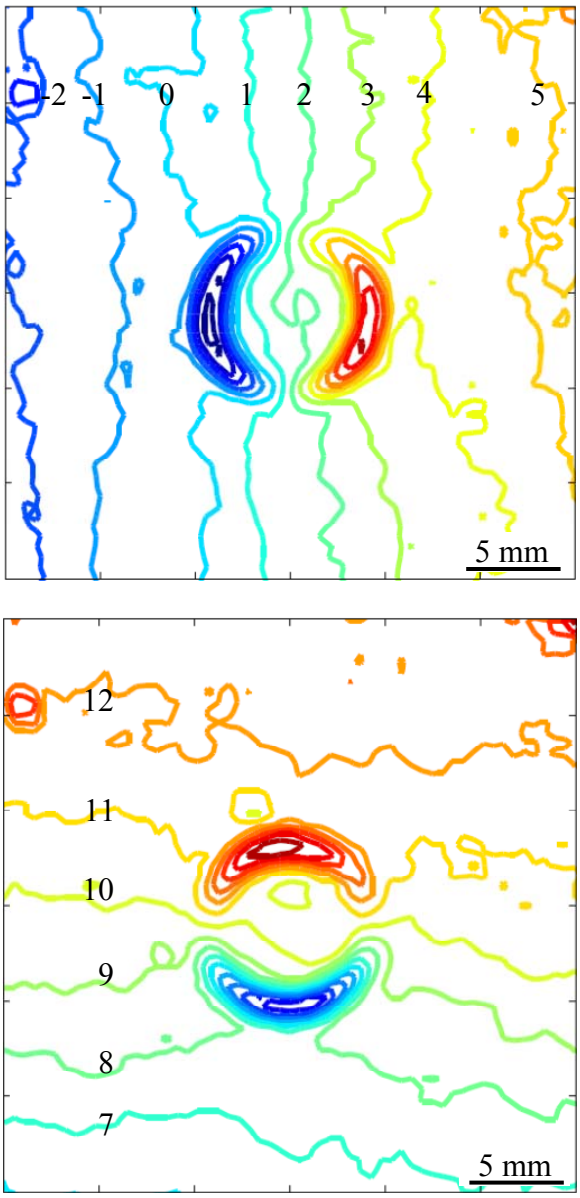

Figure A4.3: Angular deflection contours, ϕ_x (top) and ϕ_y (bottom) in a thermally stressed borosilicate glass plate. Contour levels are in 10^{-4} radian.

A5 Curing induced surface slopes of a polymer coated silicon wafer

One of the potential applications of the proposed reflection DGS methodology is to monitor the evolution of surface slopes and curvatures (and hence stresses) during deposition and curing of dissimilar material films on silicon wafers during microelectronic fabrication. To demonstrate this feasibility, an experiment in which slopes and curvatures of a thin silicon wafer, spin-coated with a layer of uncured epoxy and monitored during the initial stages of the curing process, was conducted. As evident from Fig. 2.2, by increasing the separation distance Δ between the object and target planes, the displacements (δ_x and δ_y) can be magnified using the optical arm, for the same angular deflection values. This feature is of significance in situations where very small ($< 1 \times 10^{-4}$ radians) angular deflections are encountered / expected, as the resolution of DGS could be intrinsically adjusted thereby minimizing measurement errors associated with small angular deflections. Equipped with this information, a feasibility experiment to measure the small surface slopes induced by *in situ* curing of a thin layer of epoxy film on one face of a thin silicon wafer was performed. A schematic of the experimental setup used is shown in Fig. A5.1. A 50.8 mm diameter, 100 μm thick double side polished silicon wafer was spin-coated on one side with 20-30 μm thick epoxy (Epothin® - a two part, low viscosity epoxy from Buehler Inc., USA; gel time ~20 mins at room temperature) layer. The epoxy-coated wafer was freely rested on a rigid platform with a square clear aperture placed parallel to the table top. The uncoated, side faced the speckle target positioned parallel to it, at a distance of Δ = 472 mm (note that a large Δ is chosen since the expected deformations are relatively small in this experiment). A beam splitter

was placed in-between the coated wafer and the target and oriented at 45˚ to the wafer surface. A Nikon D3000 DSLR camera fitted with an extension tube and a 70-300 mm focal length lens was positioned at a distance of L = 1505 mm from the wafer surface. Then, the camera was focused on the speckled target *via* the beam splitter and the silicon wafer. Then, a reference image of the speckles was recorded at time t = 0 mins (corresponding to 10 minutes after the start of mixing the two-part epoxy resin and hardener).

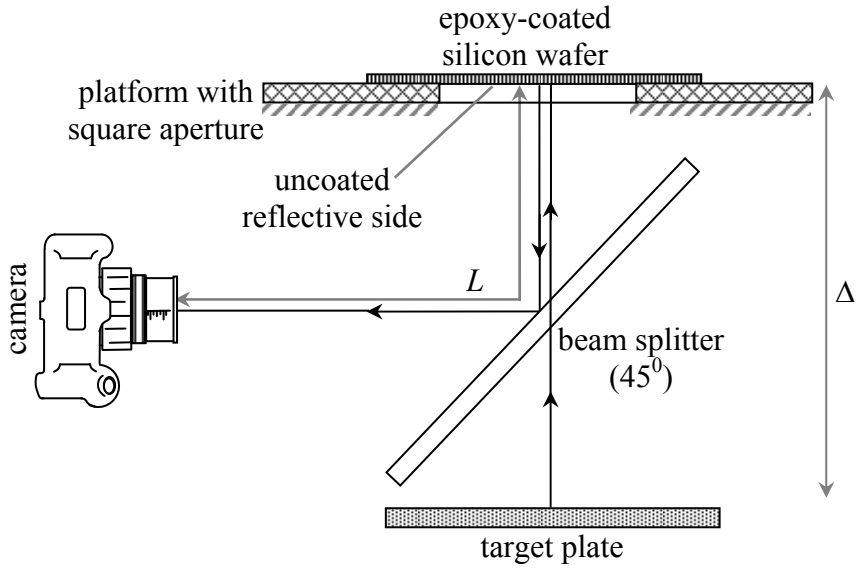

Figure A5.1: Schematic of experimental setup used to measure surface slopes of a 100 μm thick silicon wafer caused by the *in situ* curing of thin epoxy film.

The images were recorded through a 70-300 mm lens with $F^{\#}$ 22 aperture, and a resolution of 1936 × 1296 pixels, each pixel corresponding to 59.4 μm on the target plane. Subsequently, perturbed images of the speckles while the epoxy cured at room temperature, were recorded at every 5 minute intervals for up to one hour. The

'deformed' speckle images were then correlated with the reference image to obtain the $\frac{\partial w}{\partial x}$ and $\frac{\partial w}{\partial y}$ contours and results for a few select times are shown in Fig. A5.2. As noted earlier, the coordinates of the contour plots were corrected for perspective effect introduced by the large Δ (Section 3.2) using coordinate mapping functions. During analyses, the recorded images were segmented into 15 × 15 non-overlapping sub-images which resulted in 75 × 98 data points at each time step.

The time-resolved contour plots in Fig. A5.2 show the evolution of surface slopes in the silicon wafer as the epoxy film cures. In the early stages of curing, the contours (t = 0-25 mins) are randomly shaped and oriented whereas subsequent contours (t = 35 mins) reveal a definite organization in terms of shape and orientation. The increase and decrease in contour densities between t = 35 mins and 55 mins is indicative of the time dependent deformation in the wafer caused by the curing of epoxy film. There is a monotonic increase in the number of slope contours up to ~45 minutes of the curing cycle as the film continues to polymerize and cross-link. Subsequently, a drop in the number of contours (and the magnitude of surface slopes) is evident suggesting a degree of relaxation of the wafer from progressive warping, possibly attributed to micro-scale debonding between the wafer and the epoxy film. In this first qualitative demonstration of the curing induced deformations, the continuous monitoring of the epoxy coated wafer was discontinued beyond the last frame in view of the demonstrative nature of the work. The slope contours at t = 35, 45 and 55 mins suggest a relatively uniform deformation of the wafer as suggested by the near-parallel and uniformly spaced orthogonal slope contours.

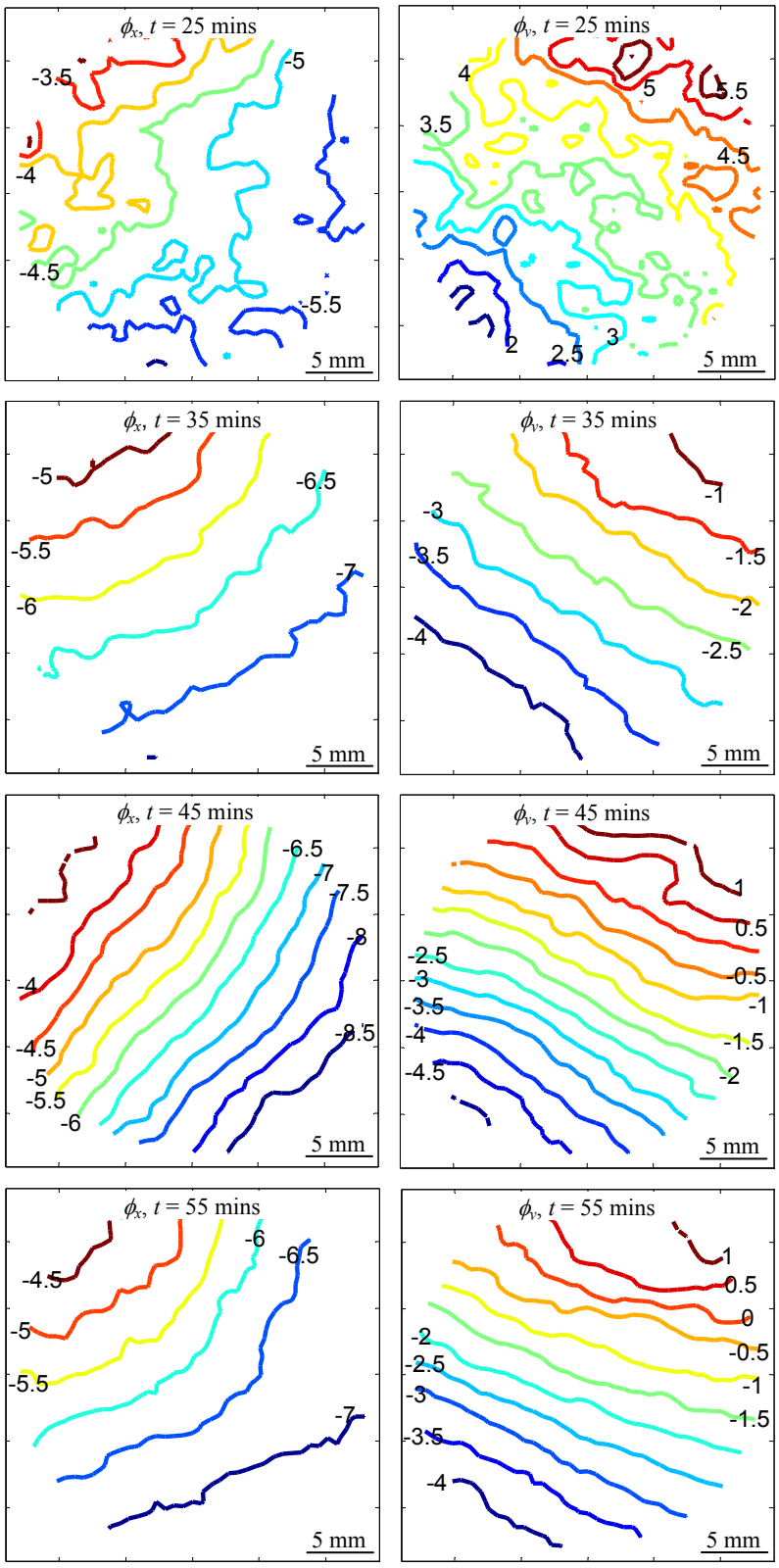

Figure A5.2: Evolution of orthogonal surface slopes $w_{,x}$ and $w_{,y}$ of silicon wafer as epoxy film cures on the wafer. Contour levels are in 1×10^{-5} radians.